Dissertation

submitted to the

Combined Faculty of Natural Sciences and Mathematics

at the Ruprecht-Karls University of Heidelberg, Germany

for the degree of

Doctor of Natural Sciences (Dr. rer. nat.)

Presented by

M. Eng. Linlin Xiao

Born in Fuzhou, China

Oral examination: Feb. 28th, 2014

Influence of Surface Topography on Marine Biofouling

This dissertation was carried out at the

Department of Applied Physical Chemistry

University of Heidelberg

Referees:

Prof. Dr. Michael Grunze

apl. Prof. Dr. Hans-Robert Volpp

Abstract

Marine biofouling, associated with the accumulation of marine colonizers on submerged surfaces, has been a longstanding problem. Among different surface properties, cell-substrate interaction is strongly influenced by surface topographies. Therefore, in this work responses of representative marine fouling species were investigated in relation to different topographies.

The settlement of zoospores of *Ulva linza* was explored on a hot-embossed honeycomb gradient. The highest settlement was found on microstructures with a similar or larger size than spores. Spore settlement density correlated with the Wenzel roughness of the topographies and 'kink sites' resembled preferred attachment positions. Following the gradient study, different settlements of cells of *Navicula incerta*, *Ulva* zoospores, and cyprids of *B. improvisus* were observed on soft-casted discrete honeycombs with the feature size as the only variable. The correlation between the 'attachment point theory' and the diatom attachment was in line with the literature. Settlement of spores deviated from the guideline of Wenzel roughness mainly due to the gregarious settlement on PDMS substrates, while the settlement of cyprids could be correlated with both Wenzel roughness and the interaction between sensory structures and comparably sized microtopographies. Furthermore, tapered microstructures with different feature spacings and aspect ratios were prepared via hot embossing and hot pulling to avoid unfavorable corners and to minimize the surface contact area. Topographic preferences of *Navicula* diatoms and *Ulva* spores during settlement were proven to be dominated by the 'attachment point theory' and Wenzel roughness, respectively.

Topographic cues guiding the settlement turned out to be complicated as they were related to both, topographies and fouling species. As effective antifouling strategies, the combined effect of a variety of surface properties seems appropriate. Along these lines, the concept of slippery liquid-infused porous surfaces (SLIPS), which combined both surface lubricity and topographies, were tested against fouling under both laboratory and field conditions. Immersion tests suggested a correlation between the stability of slippery coatings in seawater and fouling resistance efficacy. On stable slippery surfaces, settlement of *Ulva* spores and *Balanus amphitrite* cyprids was remarkably reduced. Although both marginal fouling-release and poor field performance indicated the

requirement of significant improvement of such coatings for practical applications, the fouling-resistant potential of the SLIPS concept was demonstrated.

Kurzfassung

Marines Biofouling, die Akkumulation von sessilen marinen Spezies auf Oberflächen, ist ein altbekanntes Problem. Neben anderen Oberflächeneigenschaften spielt die Topographie eine wichtige Rolle für die Wechselwirkung zwischen Organismus und Substrat. Im Rahmen dieser Arbeit wurde daher der Einfluss unterschiedlicher Topographien auf die Kolonisierungsantwort verschiedener mariner Modelorganismen untersucht.

Auf heiß-geprägten PMMA-Bienenwaben-Gradienten wurde das Besiedlungsverhalten von Sporen der Grünalge *Ulva linza* analysiert. Die höchste Akkumulation konnte auf Mikrostrukturen beobachtet werden, deren Durchmesser ähnlich oder größer dem Sporenkörper waren. Die Sporendichte korrelierte außerdem mit der Wenzel Rauigkeit. Darüber hinaus wurde festgestellt, dass die Sporen Eckpositionen (engl. ‘kink sites’) als Besiedlungsstelle bevorzugen.

Um den alleinigen Einfluss der Strukturgröße auf die Besiedlung durch die Kieselalge *Navicula incerta*, *Ulva linza* Sporen und Cyprid-Larven der Seepocke *Balanus improvisus* zu untersuchen, wurden diskrete Bienenwabenstrukturen in PDMS gegossen. Das Verhalten der Kieselalge konnte mit der Angriffspunkt-Theorie (engl. ‘attachment point theory’) in Zusammenhang gebracht werden und stimmte mit der Literatur überein. Während die Ansiedlung der Seepockenlarven mit der Wenzel-Rauigkeit korrelierte und einen Zusammenhang zwischen der Größe der Sensororgane und den Strukturgrößen zeigte, wich das Sporenverhalten bedingt durch die gregäre Ansiedlung (engl. ‘gregarious settlement’) auf PDMS Substraten von den Voraussagen der Wenzel-Rauigkeit ab.

Zusätzlich wurden konisch zulaufende Mikrostrukturen durch Heißprägen und Heißziehen von Polycarbonaten präpariert, um bevorzugte Ecken zu vermeiden und die potentielle Kontaktfläche zwischen Substrat und Organismus zu minimieren. Es konnte gezeigt werden, dass das Ansiedeln von *Navicula* durch die Angriffspunkt-Theorie beschrieben wird, wohingegen *Ulva* Sporen hauptsächlich durch die Wenzel-Rauigkeit der Topographie beeinflusst wurden.

Zusammenfassend stellte sich die Korrelation zwischen Besiedlung und Topographie als komplex heraus, da sowohl die Art der Strukturierung als auch die

Spezies relevant waren. Als effektive Strategie gegen Biofouling bietet sich daher die Kombination verschiedener Oberflächeneigenschaften an. Diesem Gedanken folgend wurden s.g. SLIPS (engl. ‘slippery liquid-infused porous surfaces’, rutschige flüssig-benetzte poröse Oberflächen), welche Strukturierung und Schlüpfrigkeit einer Oberfläche kombinieren, in Labor- und Feldversuchen im Hinblick auf Biofouling getestet. Inkubationsexperimente zeigten einen Zusammenhang zwischen der Stabilität der Beschichtungen in Meerwasser und der Resistenz gegen verschiedene Organismen. Auf stabilen SLIPS war die Ansiedlung von *Ulva linza* und *Balanus amphitrite* signifikant reduziert. Trotz der nicht optimalen Ergebnisse in Haftstärke-Experimenten und Feldversuchen, die auf die Notwendigkeit weiterer Verbesserungen hindeuten, demonstrieren die gezeigten Resistenzeigenschaften die potenzielle Anwendbarkeit dieser Beschichtungen.

Contents

1 Introduction

Marine biofouling, the undesired colonization of various fouling species on submerged natural or man-made surfaces in seawater [1, 2], introduces tremendous problems into ocean-related industries [3-5], which sequentially exert a considerable impact on different aspects of the modern world [6, 7]. Once underwater devices are encrusted by fouling organisms and their by-products, their performance in applications is highly impaired. A primary strategy to combat fouling is based on preventing biofoulants from attaching, which could be realized by covering the submersed surfaces with an antifouling (AF) coating. Most successful antifouling paints in history used biocides to deter/kill marine colonizers through a leaching process [8-10]. It is a delicate work to achieve the balance between the efficacy and the durability for practice, and besides, it should be noted that hazardous toxicants released from previously and currently applied marine coatings are one of the main sources responsible for the water pollution along the coastline and in the harbors. Due to the ecological concerns [11], gradual banning of the use of biocides in AF coatings spurs a huge market to pursue novel non-toxic antifouling solutions, thus triggering the incentive for research activities in this field.

Colonization of a new substrate by algal cells or invertebrate larvae opens a prelude to the life story of most marine fouling organisms, e.g., microalgae diatom *Navicula incerta*, macroalgae *Ulva linza* and invertebrate barnacles of *Balanus amphitrite* and *Balanus improvisus*. The initial contact between the fouling organisms and the host substrates occurs at the interface. As a consequence, understanding of the cell-substrate interaction at the interface is essential to the modulation of coating properties to eventually achieve anti-biofouling. Among different surface properties, it has long been recognized that cells respond to substrate topographies [12]. Additionally, topography has been proven to be of comparable importance as chemistry in constructing natural antifouling surfaces, e.g., the skin of sharks and pilot whales and the surface of lotus leaves [13-15]. Therefore, topography is considered as a fundamental key factor to be taken into account for marine coatings design.

Different topographic features, i.e., feature size, feature spacing, aspect ratio, surface roughness, etc., have been investigated with respect to the applications in the marine antifouling field. Topography could either enhance or reduce the recruitment of fouling organisms. It was indicated in the literature that critical size and spacing of topographic features with regards to the dimension of fouling organisms or relevant sensory and adhesive organs were fundamental to the surface defense against fouling [16,

17]. For instance, *Ulva* spore settlement on Sharklet AF^{TM} topographies with feature width and spacing of 2 µm was reduced by ~85% compared with the smooth control [14]. And besides that, contact guidance was also observed to be vital for fouling organisms to attain solid adhesion on substrates against external hydrodynamic forces. In addition, as the fluid hydrodynamic interaction played an integral role in attracting fouling accumulation [18], it was pointed out that the concept of fluid slip might provide a possible route to contribute to the antifouling character of marine coatings.

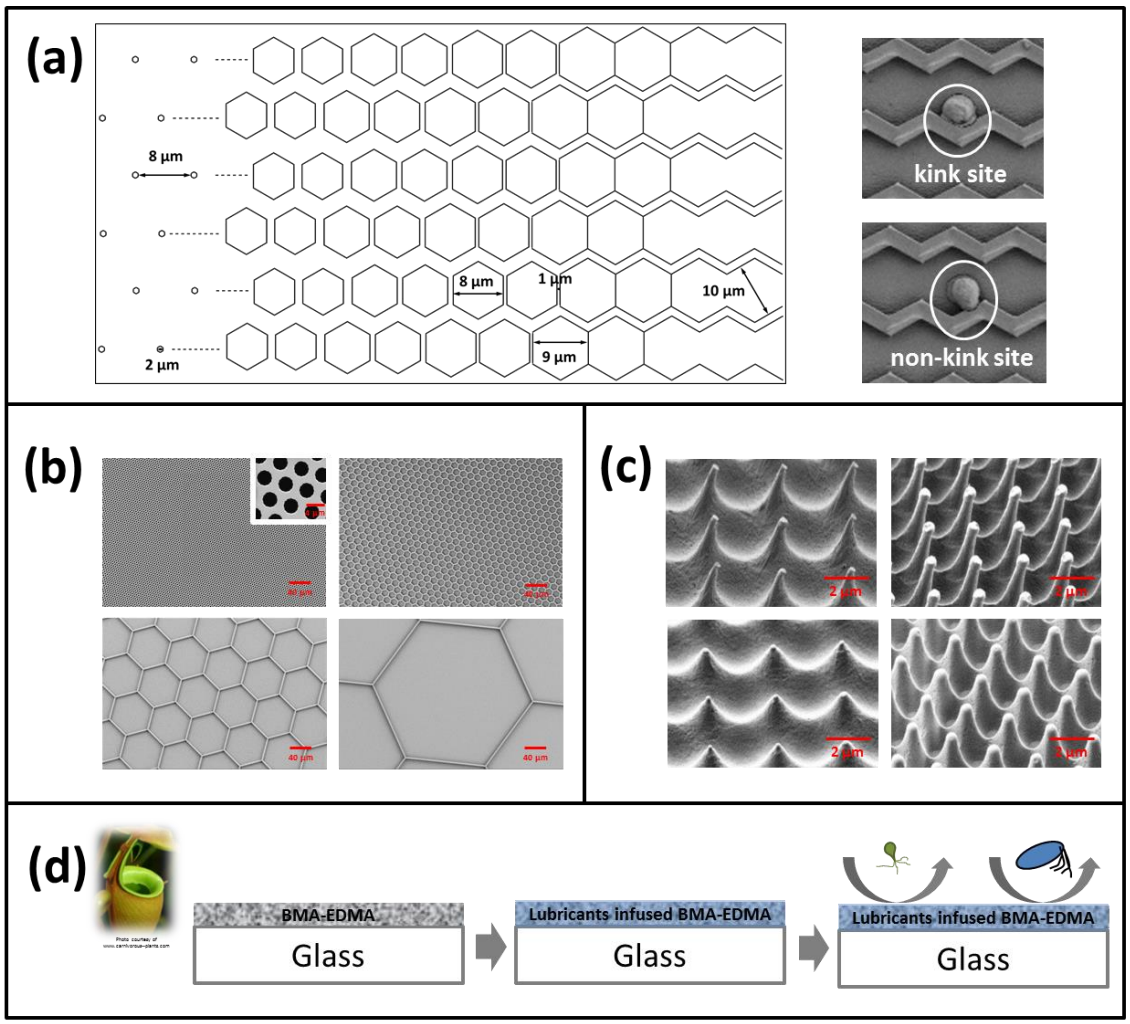

Figure 1-1 Overview of the different patterns and approaches used in this thesis. (a) Honeycomb gradients in Section 4.1; (b) discrete honeycombs in Section 4.2; (c) tapered microstructures in Section 4.3; (d) microtexture-based slippery liquid-infused porous surfaces in Section 4.4.

Due to the high diversity in the morphology and the settlement mechanism of marine colonizers, it is difficult to come up with a general principle to interpret and predict their behaviors. Currently existing models and theories, e.g., ERI model and 'attachment point theory' [16, 19], were limited in their general applicability as they were

proposed on the basis of a restricted range of organisms and topographies. Intensive research with different fouling species and varying topographic features is necessary to gain a more systematic understanding of biofouling and antifouling effects of topographies.

In this study, to obtain topographies of specific interest, a variety of fabrication approaches, i.e., hot embossing, hot pulling, PDMS casting and UV-initiated polymerization, have been employed, and subsequent biological assays were performed with correspondingly targeted fouling organisms. In Section 4.1 (Figure 1-1a), the influence of topographic properties (Wenzel roughness, local binding geometry, etc.), in terms of honeycomb size gradients, on the settlement behaviors of *Ulva* spores was closely examined. Following the gradient study, a series of discrete honeycombs of different sizes (Section 4.2, Figure 1-1b) was constructed and studied to determine the size preference of different fouling species. Furthermore, the topographic cues guiding the settlement of different fouling species were compared on a set of tapered microstructures with minimized contact area on the outmost surface (Section 4.3, Figure 1-1c). Finally, going beyond the direct fouling-topography interaction (Section 4.1-4.3), SLIPS surfaces (Section 4.4, Figure 1-1d) were prepared by infusing a lubricant liquid into porous microtopographies to enhance their resistance to fouling. The antifouling performance of the SLIPS surfaces was examined with both laboratory and field tests.

2 Background

2.1 Marine biofouling

The detrimental damage to maritime industries (e.g., shipping, aquaculture and ocean energy) [3-5] caused by a substantial variety of microfoulers (e.g., bacteria and diatoms) and macrofoulers (e.g., macroalgae and barnacles) has been a long-standing issue remaining to be addressed. Once natural or manufactured surfaces are immersed in the sea, they are immediately subjected to the unwanted colonization of various fouling organisms. The consequence of abundant marine biofouling is associated with conspicuous economic, environmental and social implications.

Taking shipping as an example, in the absence of effective fouling-control strategies, the vessel surfaces will be dominated by marine lives in a short period of time (150 kg fouler/m^2 within 6 months of immersion) [20]. Because of the increased surface roughness caused by hull fouling, the increased hydrodynamic drag has a remarkable impact on fuel consumption (up to 40% by minor fouling) and operation efficiency (10%-18% by moderate fouling) [20]. The additional expenditure (fuel consumption, hull cleaning, repainting, etc.) related to hull fouling of the mid-sized naval surface ships (the entire Arleigh Burke class destroyer DDG-51) amounts up to ~56 million US dollars per year [6]. Moreover, in parallel with the prosperity of open ocean exchange shipping brings together the aquatic invasive species (AIS), one of the greatest threats constantly challenging regional ecological balance and public health. Hull fouling has been documented as a comparably important vector to ballast water in term of introducing these nuisance species [21, 22].

In seawater a high diversity of marine organisms (more than 4000 species as reported [23]) are involved in the fouling of immersed solid surfaces. As shown in Figure 2-1, these fouling organisms cover a wide range of sizes (e.g., bacteria 0.25-1 μm, spores of *Ulva linza* 5-7 μm, and cyprid larvae of *Balanus amphitrite* ~500 μm). The accumulation of marine foulers are normally grouped into ‘microfouling’, referring to the formation of biofilm by unicellular microorganisms (bacteria, diatoms, etc.); ‘soft macrofouling’, involving the recruitment of macroalgae (seaweed) and soft invertebrates; and ‘hard macrofouling’, comprised by the colonization of shelled invertebrates (e.g., barnacles, tubeworms and mussels) [24].

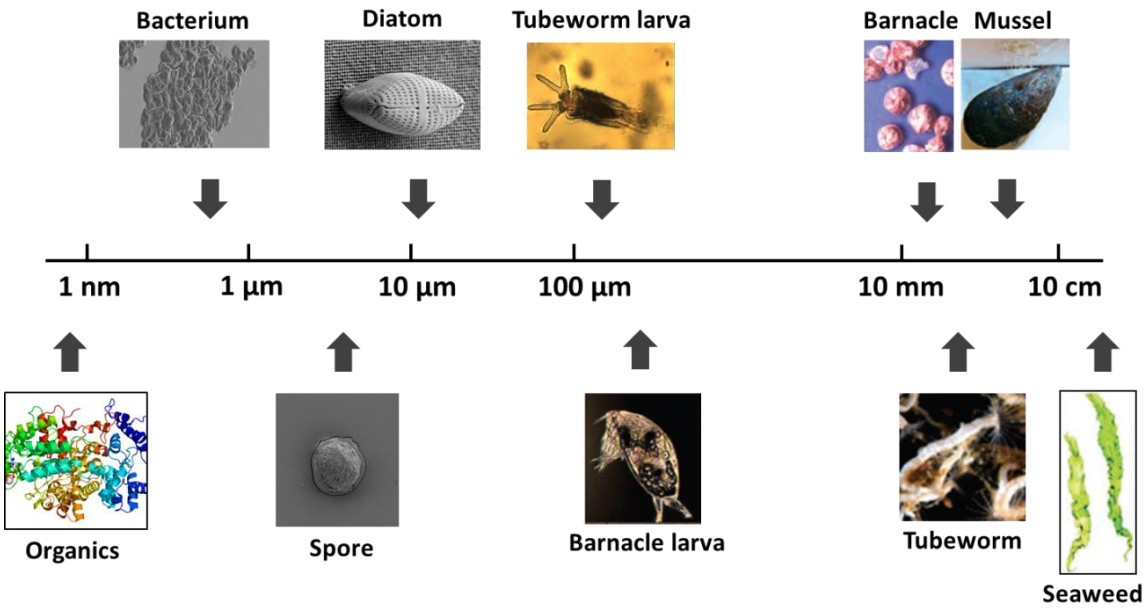

Figure 2-1 Size scales of representative fouling organisms (adapted from Callow et al. 2011 [24]).

Although the exact sequence of biofouling is unknown, a distinction could be made among different key stages of biofouling (Figure 2-2) [23, 25]. Once a clean surface is immersed in the ocean, the development of the 'conditioning' film, mainly consisting of physically absorbed organic and inorganic molecules (proteins, polysaccharides, proteoglycans, etc.) [26, 27], will take place within minutes driven primarily by electrostatic and Van der Waal's forces. The formation of conditioned surfaces is followed in the first 24 h by the accumulation of pioneering bacteria and other unicellular microfoulers. As the attachment of a succession of algal cells and invertebrate larvae occurs within one-to-several weeks with the promotion of extracellular polymeric substances (EPSs) secretion to facilitate the adhesion, a more balanced view of marine fouling is provided by the 'dynamic' model [28] rather than the linear 'successional' model. Following the attachment, further colonization between the organisms and the substrates is supported by the water movement through Brownian motion, sedimentation and convective transport. A mature fouling coverage is eventually attained by the fixation, growth or even emigration of settled fouling species under optimized surface conditions. It should be noted that this is just a simplified view of colonization, as fouling represents a highly dynamic cell-substrate interaction and the degree of fouling and the specific fouling community depend not only on the substrate (physicochemical properties, moving speed, etc.) but also on the environment (geographical location, season, etc.).

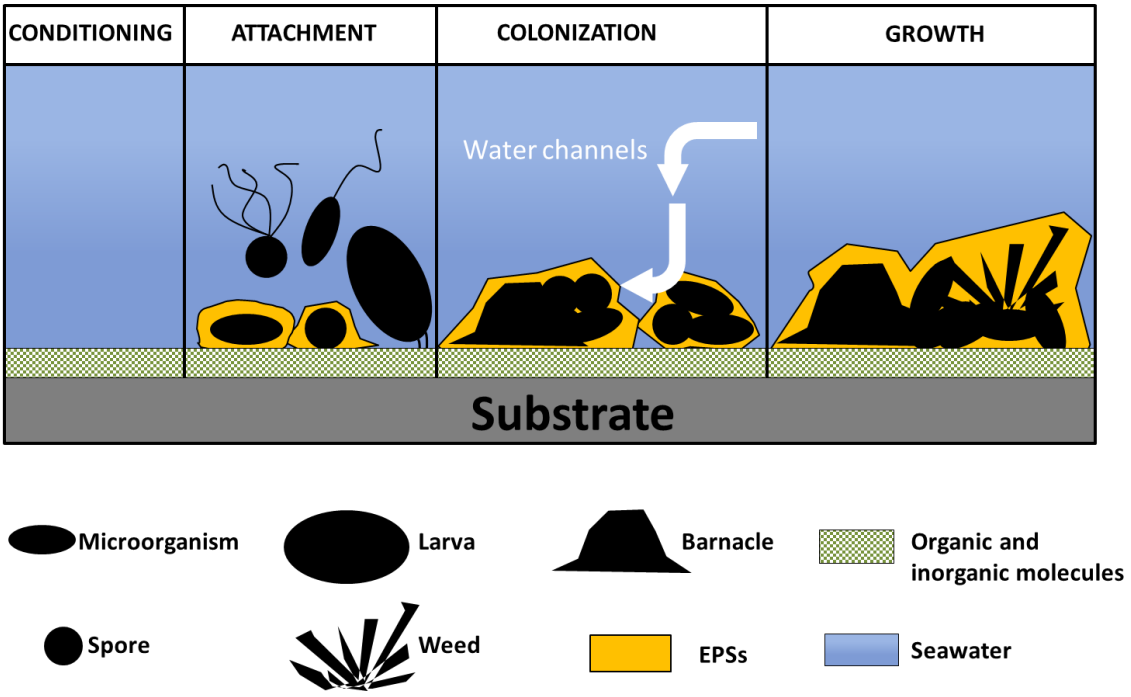

Figure 2-2 Scheme of critical biofouling stages (adapted from Chambers et al. 2006 [25]).

2.1.1 Spores and sporelings of *Ulva linza*

Being one of the most frequently observed soft-fouling species in the water line, the green algae of *Ulva linza* have been widely studied as a model marine fouling organism. The initial stage in the life cycle of this intertidal macroalgae is accomplished via the colonization of various substrates by zoospores (Figure 2-3a) [29-31].

The quadriflagellate motile spores are pyriform 'naked' cells with the size of 5-7 µm in length and 5 µm at the widest point of the body [32]. The prominent probing ability of spores facilitates the selection among a range of surface properties (topographic, chemical, mechanical, etc.) during the temporary exploration phase (pre-settlement). A number of motion patterns have been detected, identified and named at this stage [33]. Besides passive sensing by swimming spores, the rapid spinning around the temporarily attached apical papilla is recognized as an additional way pertinent to spore exploration [34]. As long as they sense an appropriate habitat, they complete the fundamental step to their survival — the permanent settlement (adhesion) on a foreign substrate in a short time (a settled spore, Figure 2-3b). To commit to irreversible attachment, they 'round up' as the glycoprotein adhesive is exuded via exocytosis from membrane-bound vesicles in the front regions of the body, flatten the anterior part against the substrate, and retract the flagellar axonemes inside the cell [31].

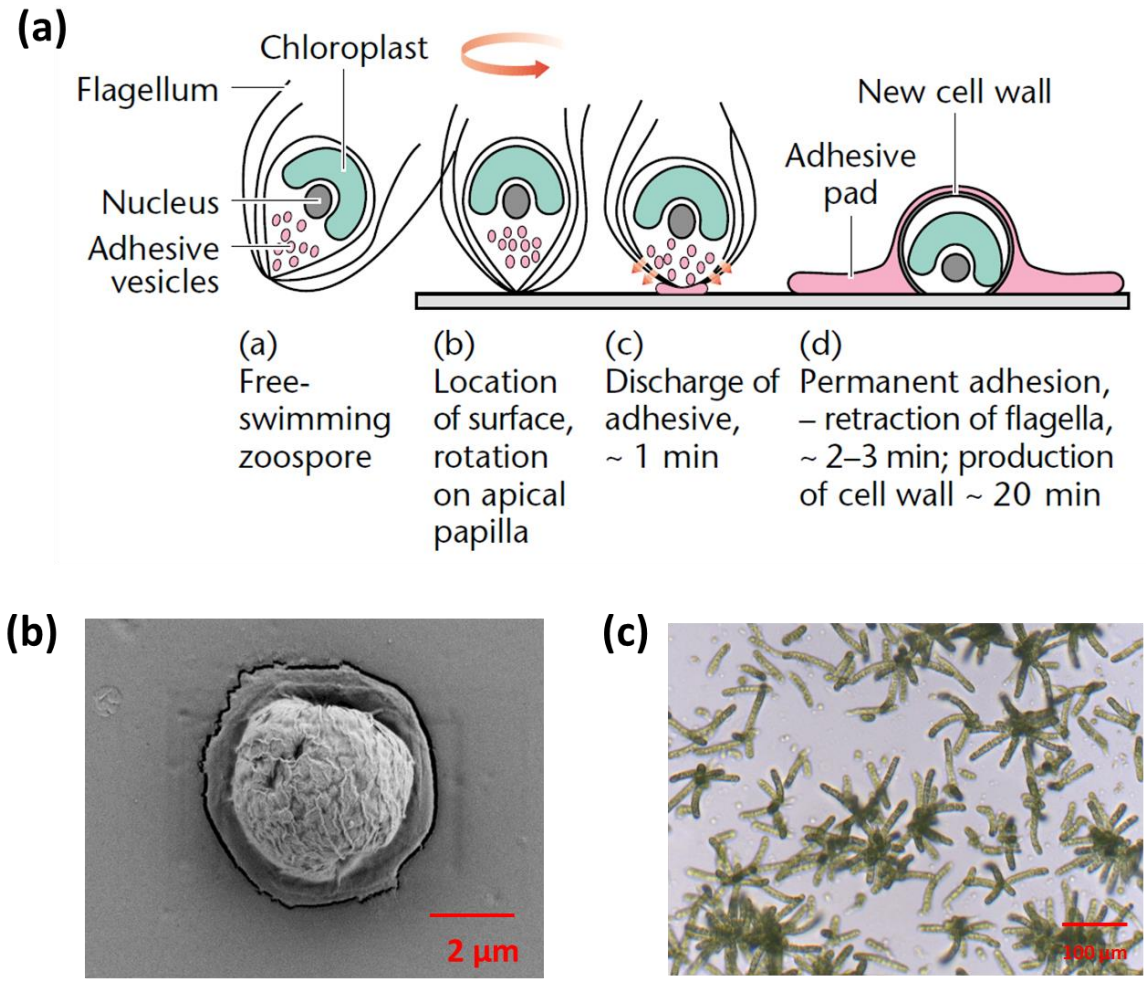

Figure 2-3 (a) Sketch of main stages involved in the exploration and settlement of spores of *Ulva linza* (taken from Maggs et al. 2003 [29]); (b) SEM image of a settled *Ulva linza* spore; (c) microscopic image of sporelings of *Ulva linza*.

Following the formation of cell walls, the germination of spores will start within a couple of hours. With sufficient supply of nutrients settled spores will finally grow into young plants — sporelings (Figure 2-3c), which are commonly cultured particularly for fouling-release assays to evaluate the adhesion strength of sporelings on targeted surfaces.

2.1.2 The diatom *Navicula incerta*

Navicula is a genus of boat-shaped unicellular diatoms featured by their sophisticated siliceous cell walls termed ‘frustules’, which are comprised of secretion-associated valves and highly ordered girdle bands of silica. This benthic raphid microalga constitutes a vital part of environmental sustainability by contributing sustainable amount of O_2 to the atmosphere (~ 25%) [35], fulfilling the aquatic carbon cycle, and supporting the energy flow of the ecological food chain. However, the ubiquitous distribution and outstanding

colonization capability render the diatom *Navicula* one of the greatest barriers with regard to anti-biofouling.

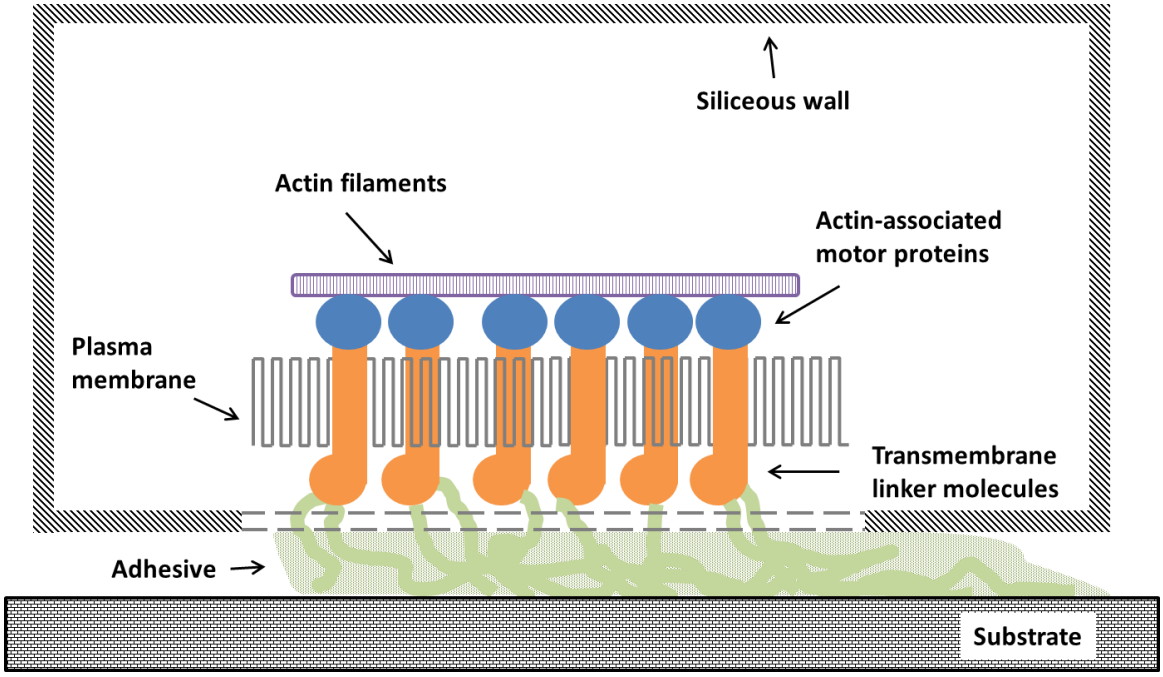

Figure 2-4 Schematic sketch of main components of the adhesive complex (AC) presumably involved in the motility of a raphid diatom (adapted from Wetherbee et al. 1998 [36]).

Three key stages are normally involved in the settlement of *Navicula* diatoms — location of the surface, reversible initial contact with the surface, and permanent final adhesion on the surface [37]. Since diatoms lack flagella, they could not actively explore the surface and hence they are brought into the initial contact with surfaces by water movement or simply gravity force in most cases. Following the primary touch with the surfaces, diatoms will choose either to settle or to relocate themselves. In the case of re-orientation, they adopt the adhesive-mediated motion 'gliding', flipping at a speed of 0.1-25 µm/s depending on both the organism and the environment [38]. This mobility is caused presumably by either the force generated by myosin in the actin and transferred through the path of actin filaments → intracellular motor proteins → transmembrane linker molecules → extracellular adhesive attached on the surface [36] (Figure 2-4), or the force generated by the directional secretion and hydration of adhesive complex (AC) and functioning independently via the guide of actin filaments in each individual part [38, 39]. Following a period of 'gliding', the permanent adhesive-related secondary adhesion, or so called sessile adhesion, is initiated.

Both transitory/motile and permanent/sessile adhesions are modulated by the secretion of extra cellular polymeric substances (EPSs) from the raphe in both valves of the cell, although the composition of the mucilage varies in relation with the species and the fouling stages. The sticky multicomponent adhesive is mainly comprised of highly hydrated carbohydrate macromolecules and it is essential to the biological success of this species.

2.1.3 Cyprids of *Balanus amphitrite* and *Balanus improvisus*

Barnacle, an important member of the hard-fouling community abundant in the intertidal zone, is featured by its reprensentative two-phase life cycle (larval phase and adult phase) [40]. The sessile and gregarious nature of this organism causes significant problems to marine-related industries. As the only sessile crustacean, the sedentary life of barnacles is initiated by exploration and adhesion of substrates by cyprid larvae (non-feeding and planktonic-benthic phase following the naupliar stage). Briefly speaking (Figure 2-5a), sexually mature barnacles are able to release nauplii into the seawater, which later metamorphose into cyprids. Cyprids approach and explore surfaces, leaving footprints. Depending on the surface properties, cyprids choose to either relocate themselves or commit settlement. The metamorphosis into juvenile barnacles is accomplished within 12 h of permanent attachment [41].

Among different species of arthropods of Cirripedia, close similarity has been observed in the larval stage in contrast to the high diversity found in the adult life. Measurements show that although there is no statistically significant variation in the size of cyprids, e.g., cyprids of *B. amphitrite* (ca. 534 µm in length and ca. 249 µm in width) and cyprids of *B. improvisus* (ca. 587 µm in length and ca. 269 µm in width), they could be distinguished when they adopt respective characteristic shapes soon after gluing themselves onto the substrate (Figure 2-5b) [42].

The attachment of cyprids onto a foreign surface is essentially composed of three stages [43, 44]: (1) exploration characterized by probing in the vicinity of the surface and walking on the surface leaving traces of ‘footprints’; (2) adhesion of cyprids supported by cyprid cement; and (3) permanent fixation by adult cement after around one month of attachment [45]. All three stages rely to great extent on the adhesive/cement mediated attachment to substrates. Although the composition of the multiprotein adhesive differs

between different stages, the attachment strength of all cements could reach up to the order of 10^5 N·m^{-2} [46].

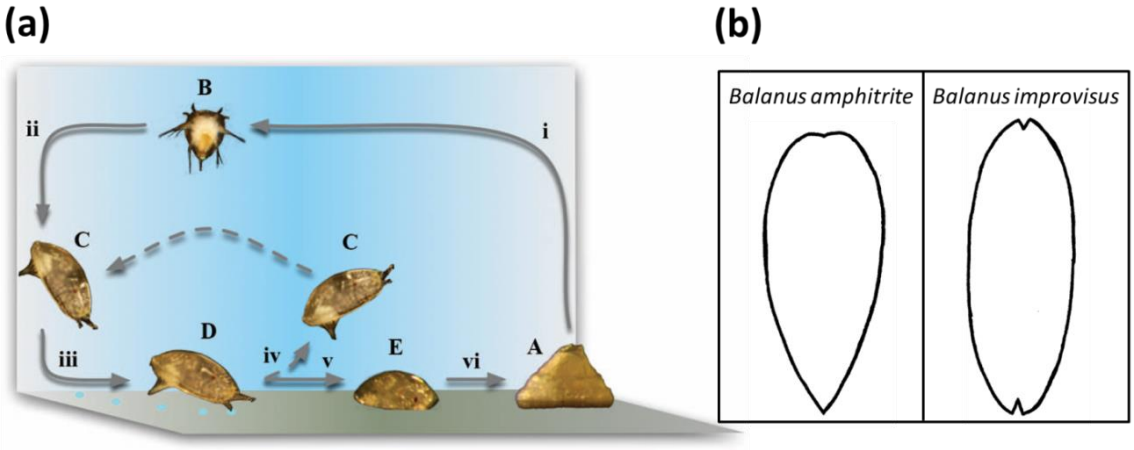

Figure 2-5 (a) Diagram of the simplified two-phase life cycle of a generalized thoracican barnacle (taken from Aldred et al. 2008 [41]). A-E represent different stages of a barnacle life cycle, i.e. juvenile barnacle, nauplius, swimming cyprid, exploring cyprid and settled cyprid, respectively. (b) Top views of the carapace of settled cyprids. *Balanus amphitrite*, tear-like shape with the anterior end slightly notched; *Balanus improvisus*, cigar-like shape with both ends obviously notched (taken from Doochin et al. 1951 [42]).

Prior to settlement, with antennules temporarily adhering to the surface a number of sensory setae around the adhesive disk of the adhesion organs and frontier segment are responsible for sensing and locating appropriate habitats. Following the exploration cyprid adhesive is discharged locally. Studies indicate that the solidification of the dual-component cement fluid occurs fast via the quinone crosslinking (tanning) to secure adhesion [47, 48]. Before the adult cement apparatuses are formed, the metamorphosis from larva to juvenile and the early growth of juvenile are dependent on this cyprid cement. The adult cement will then be secreted gradually with the development of relevant apparatuses to further secure the growth and maturing of barnacles. Mutual combination of sensory and adhesive organs of cyprids and the substrates via the bridge of cement completes the life story of barnacles.

2.2 Anti-biofouling strategies

Regarding the serious issues introduced by marine biofouling, solutions are desired to solve this problem. Once fouling organisms get a hold on submersed solid surfaces they could rapidly colonize the substrates and therefore are difficult to remove. Thus, prevention is a superior option to cure. Marine anti-biofouling refers to the actions which

prevent or counteract the recruitment of fouling organisms on underwater surfaces such as those of ships, thus improving the performance and durability of underwater devices. This could essentially be achieved by applying a specialized coating (an anti-fouling paint) onto solid surfaces. To minimize the possible damage, great efforts have been made in different fields and over a long time to create the barriers against different fouling organisms, such as slime, seaweeds and barnacles.

2.2.1 Historical development of antifouling coatings

The adverse influence of unwanted colonization of marine species has been recognized for over 2000 years. Since the first reported human activities against marine fouling in 700 BC, antifouling technologies have highly developed to comply with up-to-date requirements [9, 23-25].

Prior to 16th century the mixture of petroleum and organic products (pitch, tar, tallow, weed, hair, etc.) were widely used to cover the bottom of wooden ships. Despite the limited antifouling achievements, these attempts took the first step in the history of marine antifouling. Later between 16th and 18th centuries metallic sheading, which could effectively resist the accumulation of worms on wooden vessels, dominated the antifouling market. However, due to the related galvanic corrosion to metallic parts of ships and its poor performance in deterring fouling of other organisms, this protection strategy gradually faded out of history from 1682. Meanwhile, the application of copper as an antifoulant appeared in 1625 and after around one century's development copper sheading became widespread in preventing fouling. Not until the turn of 19th century it was discovered that the dissolution of copper explained the antifouling performance. The use of copper sheathing was nearly terminated in the late 18th century as a result of the uncertainty of its antifouling function and the galvanic corrosion to the iron ships which were newly introduced.

The appearance of iron ships caused important changes in the ship coatings design. From the mid of 1800s until the end of the Second World War the concept of antifouling was based on the extensive employment of toxic compositions (copper oxide, arsenic, mercury oxide, etc.) in the polymeric coatings. The development of antifouling coatings during this period, featured by going from 'hot plastic paints' to 'cold plastic paints', highly focused on improving the antifouling efficiency, extending the service life, and simplifying the painting process.

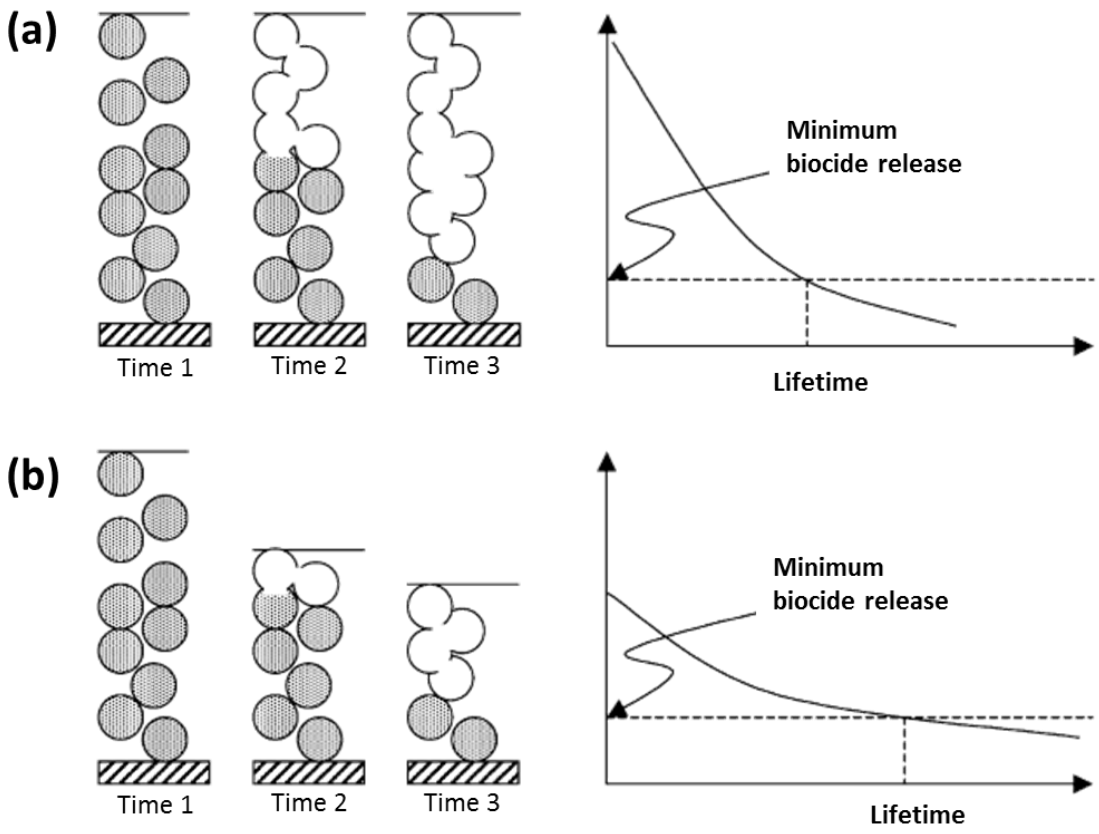

Figure 2-6 Working schemes and biocide release diagrams of traditional (a) insoluble and (b) soluble matrix coatings. 'Minimum biocide release' represents the point where the antifouling coatings reach the efficient limit (adapted from Yebra et al. 2004 [9]).

In 1950s paints composed of tributyltin (TBT) launched the revolution and took the dominant place in the antifouling field for the next half century. The extremely toxic organotins were first introduced in a 'free association' way in the insoluble polymeric matrix (Figure 2-6a) [8]. The functioning components were dissolved by the seawater, leaving the unsolvable porous texture. With the growing service time, the antifouling efficacy went down with the decreasing release rate of biocides due to the longer distance that the dissolved pigments had to travel though. This kind of paints was characterized by their excellent mechanical stability but limited lifetime (12-18 months). Combining soluble binder in coatings was the key to the construction of soluble matrix paints (Figure 2-6b), which were then further developed into tributyltin self-polishing copolymer (TBT-SPC) paints [10]. The former was a natural rosin-based paint, which consisted of a large amount of acids. The carboxyl groups of the acids could be easily dissolved in seawater via alkaline hydrolysis and the biocides could then be released [49]. Unfortunately this coating was far from being ideal because of the unpredictable fast

dissolution rate and the exponential erosion with the growing vessel speed attributable to the lack of hydrophobic proportion in the coating, not to mention the instability in air because of double bond oxidation. To achieve steady toxicant release and satisfactory balance between antifouling performance and mechanical stability, the tributyltin self-polishing copolymer (TBT-SPC) paints were designed. When coatings were immersed in the sea, the top surface was renewed in parallel with the release of biocides due to the erosion of the outmost layer. This process was initiated by the saponification of the binders (typically carboxyl-TBT linkage) in seawater and resulted in more brittle and hydrophilic polymer framework, which could be easily disintegrated in the ocean. The vital components of these paints (binder groups, hydrophobic proportion, etc.) could be well tailored to achieve expected polishing rates (tunable specific rates in the range of 5-20 μm per month) and effective lifetime (as long as 5 years) to satisfy the practical applications on vessels of different sailing speeds and idle periods. To add to the advantages, possible combination of varying biocides (copper, triorganotins and booster biocides, etc.) in such systems facilitated the resistance against a wide spectrum of marine colonizers.

With the growing environmental concerns, organotin-based coatings were gradually withdrawn from the market due to their detrimental effects on marine ecology and human health (i. e. 2003-IMO ban on TBT paint application; 2008-IMO ban on TBT based paints). New research started to focus on tin-free biocide-based antifouling coatings in the directions of tin-free self-polishing copolymers (tin-free SPCs), controlled depletion systems (CDPs) and hybrid systems. The working mechanism of tin-free SPCs in seawater is assumed to be the same as TBT-SPCs, while CDPs is an improvement of traditional soluble matrix technology by applying modern reinforcing resins. The hybrid of CDP and SP, such as Interswift 655, also has an important position in the market. Although all these coatings are free of TBT, they are generally functioning on the basis of releasing biocides or co-biocides. Due to ecological concerns about the unclear consequences of these biocide-containing paints, there is a tendency towards the revolution to obtain fully biocide-free antifouling coatings. The difficulty lies in the achievement of the balance between economic feasibility, practical success and environmental sustainability. Intensive research interest therefore has been raised in the new approaches of anti-fouling (AF) coatings (e.g., coatings with bioinspired topographies or coatings with low surface energy) and fouling-release (FR) coatings (e.g.,

PDMS-based coatings) free of toxic components. To optimize their functionality, studies on a multi-disciplinary platform are desired.

2.2.2 Surface properties influencing biofouling

Modulation of fouling organism recruitment (antifouling) and detachment (fouling-release) could be realized by tuning different properties of antifouling coatings, such as chemistry, topography, elasticity, etc. The antifouling studies on topographies are summarized in Section 2.3.

Coating chemistry

The chemical composition of coatings, in part determines the degree of hydration and surface wettability of antifouling paints, which have been proven to be critical to their antifouling performance.

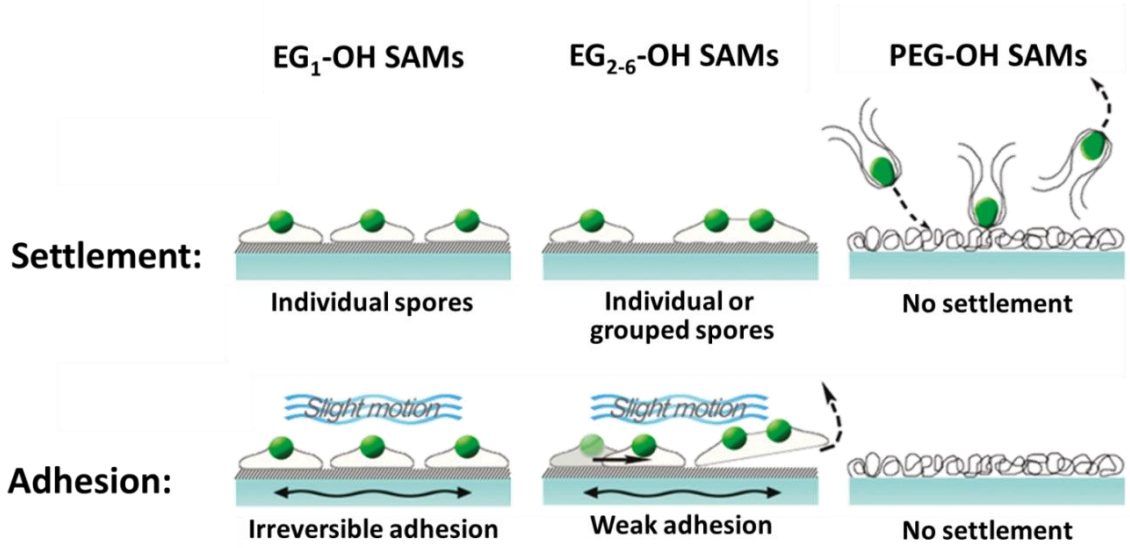

Figure 2-7 Settlement and adhesion of *Ulva* spores on OEG and PEG SAMs (taken from Schilp et al. 2009 [50]).

A representative example could be given by ethylene glycol (EG) based SAMs. Polyethylene glycol (PEG) is one of the most outstanding materials in resisting the settlement and adhesion of organic molecules, micro-foulers and macro-foulers [50-53]. This prominent antifouling performance is closely correlated with the surface hydration of PEG. In aquatic solution $(EG)_n$ chains are highly hydrated, representing an environment similar to the water surroundings, and could therefore effectively block the

interaction between substrates and the adhesive discharged by various colonizers. In the work presented by Schilp et al. [50], antifouling investigation was carried out on self-assembly monolayers (SAMs) constructed with a series of $(EG)_n$ thiolates containing different numbers of EG units. Results (Figure 2-7) showed that SAMs with more than one EG unit per molecule generated sufficient hydration to exclude the irreversible attachment of spores. Although spores did settle on $EG_{2\text{-}6}OH$ SAMs, the weak adhesion could not hold up even slight hydrodynamic force. Comparatively, no settlement was found on PEG SAMs and its distinguished resistance to fibrinogen and algal cells was independent of the terminal end groups.

In another study [54], adsorption of fibrinogen proteins and attachment of *Ulva* spores and *Navicula* cells were tested on hexa(ethylene glycols) (EG_6) SAMs terminated with different alkoxyl end-groups. Results indicated a dependence of biological preference on the surface wettability induced by the end groups. The amount of firmly adhered cells, both spores and diatoms, increased with decreasing surface wettability, which was consistent with the protein adsorption results. The general trend found in all biological tests suggested the difficulties in replacing the water from the interface diminished the possibility for bioadhesive to come into direct contact with relatively more hydrophilic surfaces. Therefore, compared with hydrophilic surfaces, hydrophobic surfaces were more attractive to the attachment of algal cells.

Coating elasticity

Another notable route to maintain ship hulls free of fouling relies on the external hydrodynamic force generated by the movement in water. The ability to minimize attachment of fouling organisms and promote detachment of accumulated foulers is determined by both coating properties and operating status of the vessels. Currently silicon elastomer-based paints, in particular made of poly(dimethylsiloxane) (PDMS), are the most commercially-available fouling-release coatings, as they possess both low surface energy and low surface modulus. Biological tests with algal cells [55, 56] showed that although no significant influence of PDMS elastic modulus on the attachment of *Ulva* spores (0.2-9.4 MPa) and *Navicula* diatoms (0.4-2.4 MPa) was detected yet, the removal rate of attached spores and sporelings was highly increased when the PDMS substrates became very soft (ca. 0.2 MPa). On the other side, Gary et al. [57] reported that settlement of larvae was positively related to the surface modulus of PDMS

(0.01-0.1 MPa), which could possibly be explained by the influence on mechanosensitive ion channels. Similar conclusions were drawn in another long-term in situ study [58] showing that the initial settlement and metamorphosis of barnacle larvae increased with growing surface elastic modulus (0.01-0.47 MPa) on both hydrophobic PDMS and hydrophilic PAMPS/PAAm DN gels, although the growth of barnacle seemed to be independent of the elastic modulus of the substrates. It was pointed out by the Brady's group [59, 60] that the coincidence between low bioadhesion and low elastic modulus of substrates could be explained by the mobility of the low modulus surface, which reduced the energy barrier to promote and expedite the failure of adhesive joins.

2.3 Biofouling studies on surface topographies

Topographic cues are among the key physiochemical properties, which influence and modulate adhesion on surfaces. Studies related to protein adsorption, cell differentiation and microbial response on different surface microtopographies have been reported [61-63]. For example, the microtopography of honeycomb-patterned porous films has been found to strongly affect the morphology and adhesion of cells [64]. Besides the studies in biomedical field, the role of surface micro- and nano-topography has been intensively investigated and discussed in the area of marine antifouling, as topographic advance is an inseparable component of prospective non-toxic antifouling (AF) coatings design. The focus of topographic researches is highly diverse in feature shape, feature size, feature spacing, aspect ratio, and roughness.

2.3.1 Influence of topographic features on biofouling

Among different surface properties, topography has been demonstrated to have both deterrent and attractive effects on the settlement of fouling organisms. The settlement is highly dependent on topographic features including size, spacing, aspect ratio and roughness.

As fouling organisms diverse highly in the shape and size (bacteria $\leq$ 1 μm; spores ca. 5-7 μm; larvae ca. 120-500 μm) at the attachment stage, feature size plays an extensive role to achieve the physical defense of topographic coatings. Effectiveness of a topographic design is associated with both the size of topographic features and the dimension of organisms in the specific fouling community [65], or in other words, effective antifouling topographies should be of a specific size scale which matches critical

sizes of targeted fouling propagules or larvae. As contact area is vital for the settlement success, microtopographies slightly larger than the cell/larva of fouling organisms facilitated settlement [32, 66, 67], in which case a fouling organism could fit inside the topographic feature entirely and therefore the degree of contact reached the maximum. On the contrary, substantially reduced settlement and attachment strength of the propagules could be found on natural or man-made surfaces with topographic features smaller than their body [16, 66].

It has been well documented in the literature that surface roughness was of great relevance to the retention of microorganisms on surface topographies with respect to biofouling issues [68]. Generally, surface roughness contributed to the increased total surface area which facilitated the adhesion of microorganisms by providing sufficient contact area for the secreted adhesive. Additionally, retention of cells by cavities or depressed/sheltered corners on a surface of certain roughness might confer the advantage to stand the external hydrodynamic force [69]. For example, during settlement spores showed their preference for certain attachment positions. Normally areas with higher dissimilarity (i.e., recessed areas) were preferentially chosen.

In the study reported by Schumacher et al. [70], the significant influence of microstructure aspect ratio (feature height/feature width) on the antifouling performance of topographic coatings was identified. Each unit increase of aspect ratio on the species-specific Sharklet AF^{TM} surfaces decreased the settlement of both *Ulva* spores and *Balanus amphitrite* cyprids by 42-45%. Settlement dependence on topographic aspect ratio could possibly be related to the underwater superhydrophobicity attained when the roughness ratio exceeded the critical limit.

2.3.2 Models related to biofouling studies on topographies

For the correlation between surface topographic features and fouling organism responses, several empirical models, namely ‘attachment point theory’, engineered roughness index (ERI) model, surface energetic attachment (SEA) model, nanoforce gradient, etc. [16, 19, 71, 72], have been proposed. These models will help understand the settlement mechanism of fouling organisms and predict surface performance of antifouling coatings, which could finally lead to an optimal antifouling design.

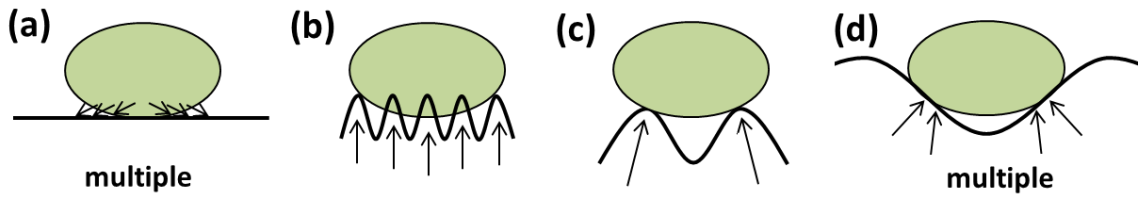

Figure 2-8 Schematic illustration of attachment points on topographies of different wavelengths (adapted from Scardino et al. 2006 [19]). (a) Multiple attachment points on the smooth surface; (b)-(c) fewer attachment points with increasing feature wavelength when the organism size is bigger than the microstructure size; (d) multiple attachment points when the organism fits entirely inside the microstructure.

The 'attachment point theory' was first brought up by Scardino et al. [19]. It suggested that more attachment points during settlement resulted in higher and stronger attachment. It was reported that the settlement of different diatoms, *Fallacia carpentariae*, *Nitzschia* cf. *paleacea*, *Amphora* sp. and *Navicula jeffreyi*, had a positive relationship with the number of available attachment points. Lowest settlement was found on microstructures with the feature wavelength slightly smaller than the size of fouling propagules/larvae (Figure 2-8c), as only two points were available for attachment. With decreasing feature wavelength (Figure 2-8c→Figure 2-8b), the settlement increased with the increasing attachment points. Multiple attachment points were present when organisms settled on smooth surfaces (Figure 2-8a) or entirely inside the microstructure (Figure 2-8d, a microstructure big enough to host the entire organism), and the settlement was highly increased in this case. In the continuous work [73], the theory was further examined with more fouling species, i.e., the diatom *Amphora* sp., the green alga *Ulva rigida*, the red alga *Centroceras clavulatum*, the serpulid tube worm *Hydroides elegans* and the bryozoan *Bugula neritina*. Generally, lower attachment of most tested organisms was observed on microstructures with the feature wavelength slightly smaller than the organism size. And the amount of settlement increased when the microstructures got wide enough to host one individual organism. Although it turned out that the theory was not confirmed for the settlement of non-motile algal spores of *C. clavulatum*, it strongly influenced the attachment of large macrofouling larvae (*H. elegans* and *B. neritina*) and also correlated with the attachment of small motile microfoulers (*Amphora* sp. and *U. rigida*). These findings reinforced the possible applications of the 'attachment point theory' in the field of biofouling to anticipate or even control the degree of fouling.

Another topographic model, ERI model, was first introduced by Schumacher et al. [16]. The model encompassed the Wenzel roughness factor (r), the depressed surface fraction (φ_s) and the degree of freedom to move around the surface (d*f*). The influence of topographic feature size, roughness and geometry on the settlement of *Ulva* spores was examined with this model. To expand this correlation for applications on more topographies, ERI_{II} [74] was set up by replacing the degree of freedom (d*f*) in ERI_I with the number of distinct features (n), which was particularly useful for topographies composing of more than one features, e.g., Sharklet AF™.

$$ERI_I = \frac{r \cdot df}{1 - \varphi_s}, \qquad ERI_{II} = \frac{r \cdot n}{1 - \varphi_s}$$

By multiplying with the Reynolds number (Re) [75], the model was proven to correlate well with the attachment of both zoospores of *Ulva* and cells of *Cobetia marina*. The Reynolds number was calculated from the density (ρ) and viscosity (μ) of the assay solution, the velocity (V) of organisms in the solution, and the characteristic length (L) of organisms.

$$ERI_{II} \cdot Re = \frac{r \cdot n}{1 - \varphi_s} \cdot \frac{\rho V L}{\mu}$$

However, the application of ERI series was restricted to interpreting and estimating the settlement of limited fouling species on specific topographies with fixed feature spacing (2 µm) and depth (3 µm).

A recently reported surface energetic attachment (SEA) model [71] was established by combining both the 'attachment point theory' and the ERI model. The probability of settlement depended on the relative attachment energy at a specific topographic site. This model took into account the cell-substrate interface properties and the geometry of the topographic features with respect to fouling organisms. Compared with ERI models which were only applicable to correlate with the reduced settlement, the SEA model could be applied to predict both enhancement and reduction of settlement.

2.4 Fabrication and analysis techniques

2.4.1 Thermal nanoimprint: hot embossing and hot pulling

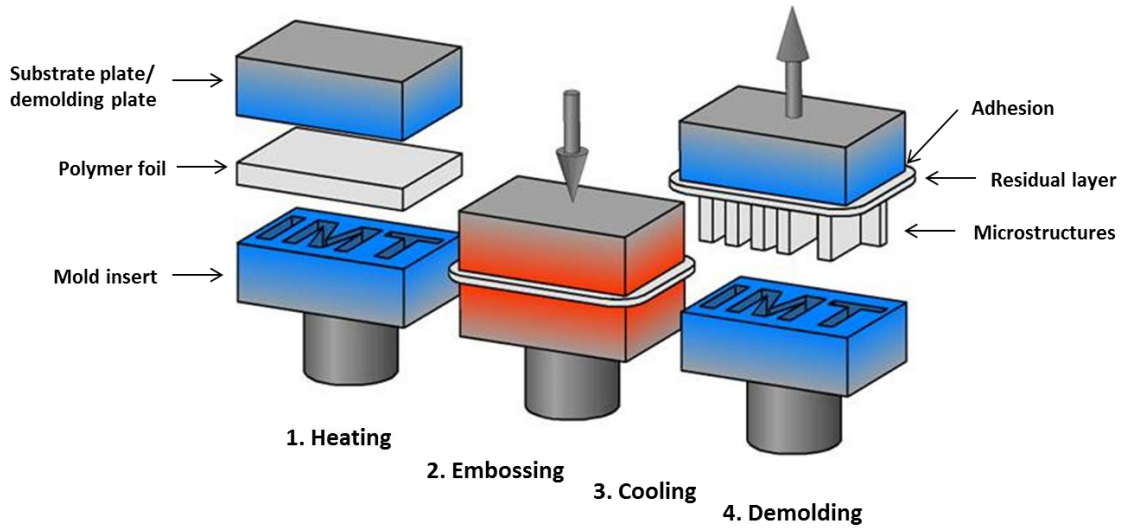

Figure 2-9 Schematic representation of a hot embossing process (taken from Worgull et al. 2008 [76]). The molding part includes a microstructured mold insert, a thermoplastic polymer foil and a rough demolding plate. The embossing process is featured by heating the polymer foil above its glass transition temperature, a two-cycle embossing with controlled force and velocity, a convective cooling, and finally a vertical demolding ensured by the adhesion between the polymeric residual layer and rough demolding plate.

For sophisticated applications of microstructures (e.g., micro-optical devices, microfluidic devices) with the dimensions of several hundred micrometers down to the submicron scale, hot embossing is one of the established technologies dedicated for the construction of delicate surface topographies. Hot embossing [77] is a micro-replication process which reproduces patterns from the mold insert onto the substrate material, typically thermoplastic polymer, e.g., polymethylmethacrylate (PMMA) and polycarbonate (PC). Compared with other molding techniques such as injection molding, hot embossing is highly recommended for producing topographies with micro-cavities, which require extremely high pressure to fill the cavities with viscous polymer melt. This replication technique is featured by the short flow distance from molten polymer to cavities on the mold and the moderate embossing velocity (in the range of 1 mm/min). And these characteristics in turn result in a remarkably lower shear stress of the polymer melt and therefore a lower residual stress of the molding part. After developing for over a century, today hot embossing could be applied to construct microstructures with small feature sizes (down to nanoscale), high aspect ratios, and sharp vertical side walls (surface

roughness < 40 nm) on a broad variety of materials (thermoplastic polymer, shape-memory polymer, metallic glasses, etc.) [78-83].

The hot embossing process could be divided into a few steps (Figure 2-9). First, under vacuum the thermoplastic material, in the form of a thin polymer film, is heated up to the molding temperature, which is typically above the glass transition temperature of the polymer. The second step involves an isothermal molding by embossing, i.e., stamping the pattern on the mold into the softened polymer with controlled force and velocity. Following the embossing, the whole setup is cooled down to the demolding temperature while keeping the embossing force constant. Finally, the structured polymer is separated from the instrument by opening the tool. The strong adhesion between the residual polymer layer and the substrate plate/demolding plate ensures accurate vertical demolding and reduces the risk of damage to the mold. The instrument applied in our study is a custom-built Hex03 hot embossing machine (Figure 2-10).

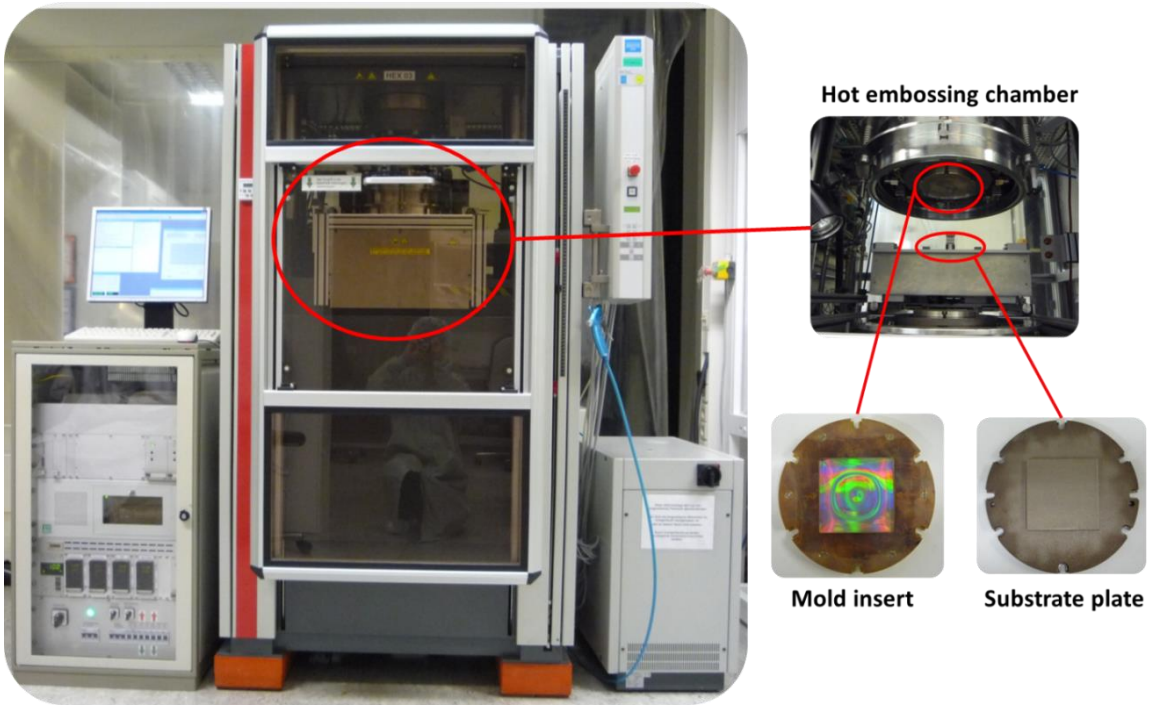

Figure 2-10 Photos of the Hex03 hot embossing machine. The standardized system ensures quick change of mold inserts, substrate plates and polymer foils.

Generally speaking, the total surface area with respect to a certain volume generally increases with decreasing microstructure size, and therefore the fabrication of submicron features is quite sensitive to the demolding force. Small imperfection of the mold insert or tiny deviation from the standard procedure could highly deform or even

rupture the replicated microstructures. Micro- or nano-structures and especially hierarchical topographies below a certain scale are suggested to be molded with a multilevel process combining the hot embossing and hot pulling techniques [84]. When microstructures are prepared via standard hot embossing, the aspect ratio of micro-features is limited by the design of the mold. To obtain microstructures with higher aspect ratios (up to 10) compared to that defined by the mold, a modified hot embossing process — hot pulling, could be applied by taking advantage of the high demolding force when we separate the molding tool. The differences between the conventional embossing and the modified pulling lie mainly in the cooling and demolding steps. Instead of cooling the tool to solidify the polymer material before demolding in hot embossing, the temperature of the mold insert is maintained above the glass transition temperature of the polymer for the hot pulling. Therefore, when the mold insert and the substrate plate separate from each other, the adhesion between the cavity of the mold and the soften polymer will stretch the viscous material to pursue relatively higher microstructures. The capability of pulling depends on both the geometry of the mold patterns and the properties of the substrate materials, particularly the elastic modulus. As the temperature is kept nearly constant throughout hot pulling and thus no time consumption for the heating and cooling cycle is required, the cycle time of hot pulling is lower compared with hot embossing, which leads to higher cost-effectiveness.

2.4.2 Scanning electron microscopy (SEM)

Scanning electron microscopy (SEM) is primarily developed to study surface morphology of bulk specimens [85, 86]. Compared with normal light microscopy the combination of electromagnetic lenses and deflection coils in SEM enables the achievement of images with higher magnification (up to 1000000×), larger depth of field (~40 times superior to light microscope), better resolution (typically 1-10 nm) , and greater versatility. In principle, SEM images are derived from the interaction between the incident electron beam and the objective surface. Signals, particularly secondary and backscattered electrons, obtained from the specimen while the focused electron beam is probing the surface, are essential to topographic imaging.

Three most important parameters of SEM are magnification, depth of field, and spatial resolution. The magnification (M) depends on the excitation of the scan coils and could be calculated from the ratio of the monitor length (L_{mon}) versus the scan length on

the specimen (L_{spe}). The depth of field (D) is defined as the change in the specimen height over which an SEM image in acceptably sharp focus could be obtained. It varies with the objective aperture radius (R_{ape}), working distance (D_w) and magnification (M). As expressed below,

$$D \propto \frac{1}{\alpha M} = \frac{1}{\frac{R_{ape}}{D_W} M}$$

where α is the divergence angle. Compared with light microscopy, SEM has a much higher depth of field due to the relatively smaller α. The spatial resolution (d), the minimum separation that can be resolved by SEM, is given by the following formula,

$$d = \frac{\lambda}{2n \sin\theta}$$

where n is the refractive index of the imaging medium (which is 1 in the vacuum of an electron microscope) and λ is the wavelength of the incident electron beam. This formula suggests that with a shorter wavelength of the beam source (extremely short wavelengths of accelerated electrons in SEM) and a larger index of the medium refraction, the resolution could be improved.

The operating compartment in SEM generally includes electron gun, lens system, scanning coils and electron detector (Figure 2-11). An electron gun consists of an electron source known as cathode and an electron accelerating chamber. Electrons could be released from the cathode by means of thermionic emission or field emission. In the case of thermionic emission, electrons are excited by raising the temperature of the cathode. While for field emission sufficient electrostatic field at the cathode is required to decrease the surface barrier for electrons to escape. The combination of these two methods, or so called Schottky emission, could further increase the emission efficiency. After being emitted from the cathode, electrons are accelerated by the high potential difference V_0 between the two poles. A limited amount of electrons with a typical energy of 1-30 keV for SEM will reach and pass through the small hole of the anode plate. As the resolution of SEM is limited by the diameter of the incident electron beam, the lens systems (condenser lenses and objective lenses) serve as the main optical components to focus the electron beam. Scanning coils mounted in the optical compartment enable the simultaneous scanning in two perpendicular directions known as raster scanning. The

amount of electrons which will finally probe the specimen is tuned by the aperture. SEM images of varying contrasts could be generated by different detectors (SE detector or BE detector) via collecting the back-scattered electrons (BE) and/or secondary electrons (SE), as they have different interaction depths with the material. With the electron source remaining under high vacuum, the measurement chamber, containing the detector and the sample holder, could be purged with N_2 for sample exchange. The measurement is carried out under high vacuum (< 10^{-10} Pa). A LEO1530 Gemini SEM device (Zeiss, Germany) is used in this work.

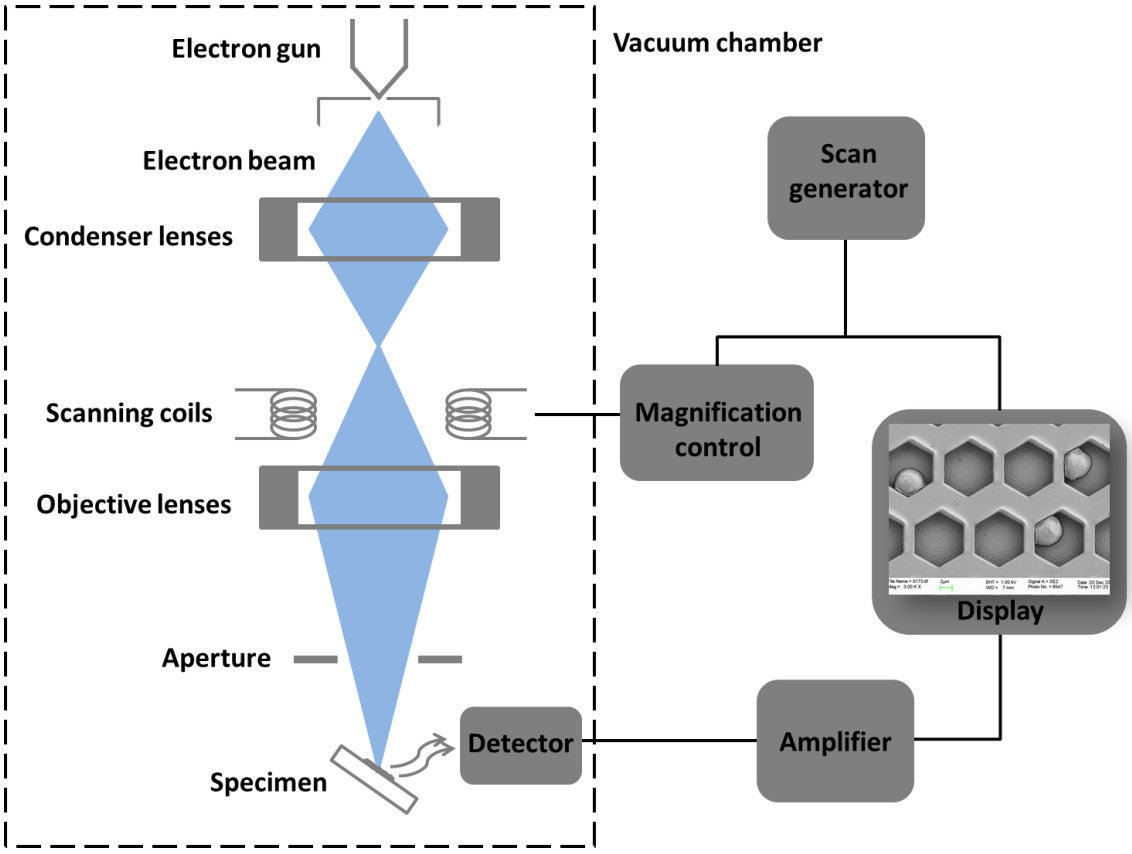

Figure 2-11 Schematic diagram of a scanning electron microscope (adapted from Goodhew et al. 2001 [85]).

2.4.3 Atomic force microscopy (AFM)

Atomic force microscopy (AFM) [87, 88], a scanning probe microscopy with demonstrated high resolution (fractions of a nanometer), is frequently applied to image, measure and construct topographies at the nano-scale. As shown in Figure 2-12, at the end of each cantilever used for AFM measurement we could find a force-sensing tip, which is capable of detecting ultra-small force. With the cantilever scanning parallel to the surface, the interaction between the tip and the surface causes the deflection of the

cantilever. The corresponding displacement of the beam light reflected from the backside of the cantilever is detected by the photodiode. The collected signals are then transformed to compile a topographic image of the tested surface.

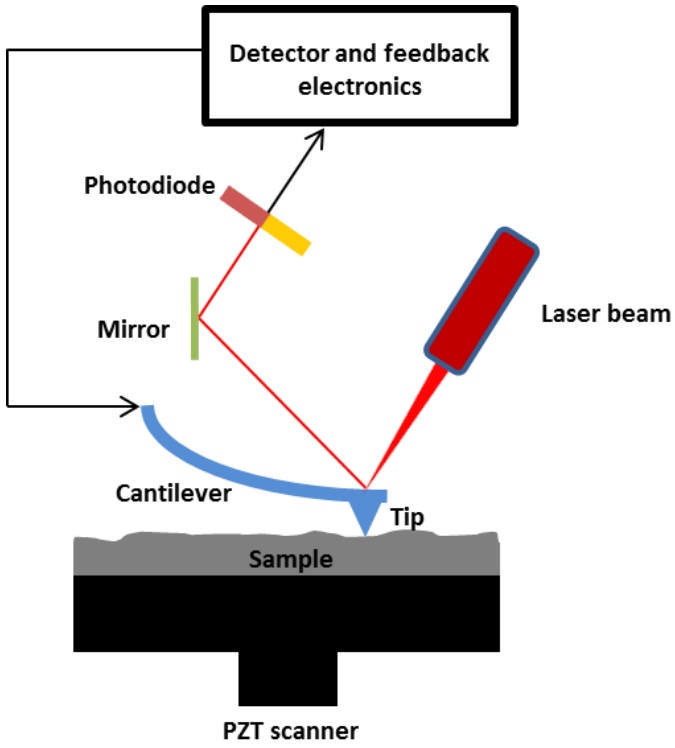

Figure 2-12 Diagram of atomic force microscopy (AFM). When the cantilever scans over a surface, the interaction between the tip and the topography deflects the cantilever, which is then detected by a photodiode via the deflection of the laser light reflected from the backside of the cantilever.

Topographies could be analyzed with AFM under different modes, namely contact, non-contact, and tapping modes. In a contact mode, the measuring tip is brought into direct contact with surfaces. The same force is exerted on the surface during scanning by maintaining a constant deflection via the adjustment of a piezoceramic element (constant-force mode), or the same distance is maintained between the tip and the sample (constant-height mode). Due to the direct physical contact, tips and samples with fragile surfaces (e.g., biological samples or organic thin films) might be deformed or even damaged during measurement. For measuring soft samples, non-contact mode is another option. In contrast to contact mode, the tip does not contact the sample surface in a non-contact mode [89]. Instead, the cantilever oscillates above the test surface either at or just above its resonance frequency. When the tip gets closer to the surface, the van der Waals force or other long rang forces will act to decrease the resonance frequency of the cantilever. The feedback loop system detects this change and makes corresponding adjustment of the

tip-to-sample distance to maintain constant oscillation frequency or oscillation amplitude. The topographic images are generated from the change in tip-to-sample distance collected during the scanning. However, in the presence of a liquid layer under ambient conditions, it is difficult to bring the tip close enough to develop detectable short-rang forces and meanwhile prevent the tip from sticking to the surfaces. Therefore, the tapping mode is developed to compensate this shortcoming. When AFM is operated under a tapping mode [90], intermittent touching or 'tapping' occurs on the sample. The tip goes through both the attractive and repulsive force region of the tip-surface interaction. The distance between the tip and the surface is adjusted by the piezoelectric element to maintain a preselected high oscillation amplitude (typically 100-200 nm compared with <10 nm in the non-contact mode), which could effectively reduce the dragging forces during the scanning. AFM images are generated by imaging the variations of the z-position of the tip during scanning. Compared with the other two modes, a relatively higher lateral resolution (1-5 nm) could be attained under the tapping mode. The AFM used in this work is a MFP-3D BioAFM (Asylum, Germany).

2.4.4 Contact angle goniometry

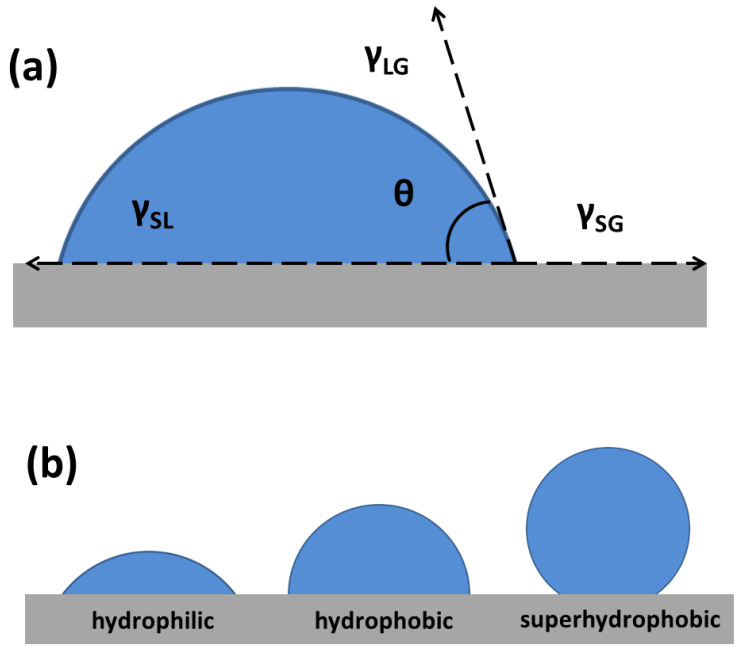

Figure 2-13 (a) Contact angle of a liquid droplet on a rigid solid surface; (b) water droplets on hydrophilic, hydrophobic and superhydrophobic surfaces.

Contact angle goniometry quantifies the degree of wetting, or more specifically, the ability of a liquid to maintain contact with a solid surface in terms of contact angles. The

contact angle (θ) is defined as the angle where the liquid/vapor interface meets the solid surface (Figure 2-13a). A smaller contact angle represents higher wettability of the surface, which indicates relatively stronger interaction between the liquid and the solid. If water is used as the testing liquid, substrates are referred as hydrophilic ($\theta < 90°$), hydrophobic ($\theta \geq 90°$) and superhydrophobic ($\theta > 150°$ with the contact angle hysteresis smaller than 5°) with increasing water contact angle values (Figure 2-13b).

On an ideal solid surface, Young's equation [91] could be applied to calculate contact angles (θ_Y) from tensions of three interfaces (γ_{SL}, solid-liquid; γ_{SG}, solid-gas; γ_{LG}, liquid-gas).

$$cos\,\theta_Y = \frac{\gamma_{SL} - \gamma_{SG}}{\gamma_{LG}}$$

This ideal equation is only valid when atomically smooth and chemically homogeneous surfaces are tested with small droplets of liquid, in which case the gravitational force of the droplets could be ignored. As real surfaces are heterogeneous complexes which combine physical and chemical differences, this ideal equation is not applicable in most cases.

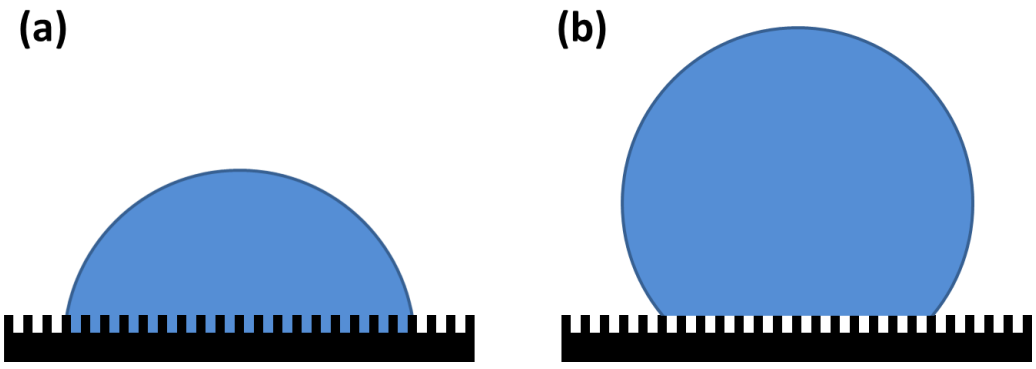

Figure 2-14 (a) Wenzel model representing a homogeneous wetting regime; (b) Cassie-Baxter model representing a heterogeneous wetting regime.

When a liquid droplet is deposited on a structured surface, the interaction could be classified into two regimes (Wenzel model [92] and Cassie-Baxter model [93]; Figure 2-14a and Figure 2-14b, respectively). In the case of homogeneous wetting into the structures, the Wenzel contact angle θ_W could be calculated from the Young contact angle θ_Y and the Wenzel roughness factor r_{Wenzel}, which is defined as the ratio between the actual surface area and geometrical surface area.

$$cos\,\theta_W = r_{Wenzel} \cdot cos\,\theta_Y$$

Some structured surfaces, such as lotus leaves, could not be fully filled with the liquid because of the small air pockets remaining between the solid-liquid interface. The degree of this incomplete wetting could be quantified by the Cassie-Baxter equation. The Cassie-Baxter contact angle θ_{CB} is determined from the surface contact fraction φ of the liquid droplet and the Young contact angle θ_Y.

$$cos\,\theta_{CB} = \varphi \cdot (cos\,\theta_Y + 1) - 1$$

A custom-built contact angle goniometer with a tilting stage is used in this study.

3 Materials and Methods

3.1 Surface preparation

3.1.1 Hot embossing and hot pulling

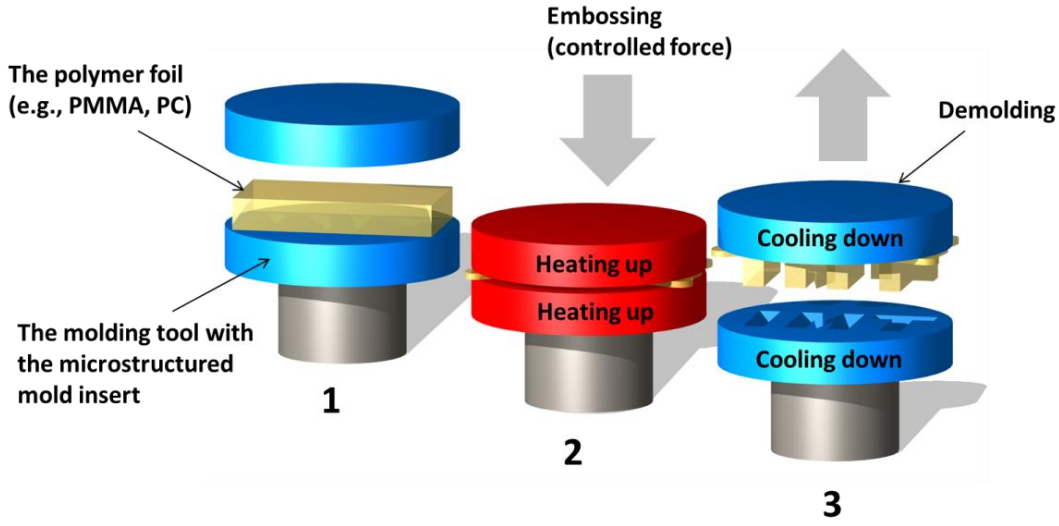

Figure 3-1 Schematic view of the hot embossing process (adapted from Worgull et al. 2008 [76]).

Microstructured surfaces constructed via thermal nanoimprint were prepared together with the group of Dr. Hendrik Hölscher at the Institute of Microstructure Technology, Karlsruhe Institute of Technology. Large-area surfaces with micro- and/or nano-structures were fabricated by hot embossing (Figure 3-1 and Figure 3-2a), a plastic molding process. The embossing parameters (molding temperature, molding force, etc.) were optimized to ensure complete constructing of the microstructures on the thermoplastic polymer (polymethylmethacrylate, polycarbonate, etc.). The embossing device consisted of the molding platform and the demolding plate. Via sandblasting the demolding plate maintained a certain degree of surface roughness, which was essential to preserve the physical adhesion with polymer sheets and facilitate the demolding process. To commence the hot embossing, the structured nickel (Ni) mold insert was fixed on the molding platform and an unstructured polymer foil was positioned between the two-part molding tool. After closing the embossing chamber, the polymer sheet was heated above its glass transition temperature. When the molding temperature was reached, the softened polymer was pressed into the cavities of the mold insert with a specified embossing force. With the applied force remaining constant, the polymer was cooled below the glass transition temperature to ca. 50 °C. Finally, the demolding took place by opening the molding tool, and the molded polymer wafer was peeled off the demolding plate.

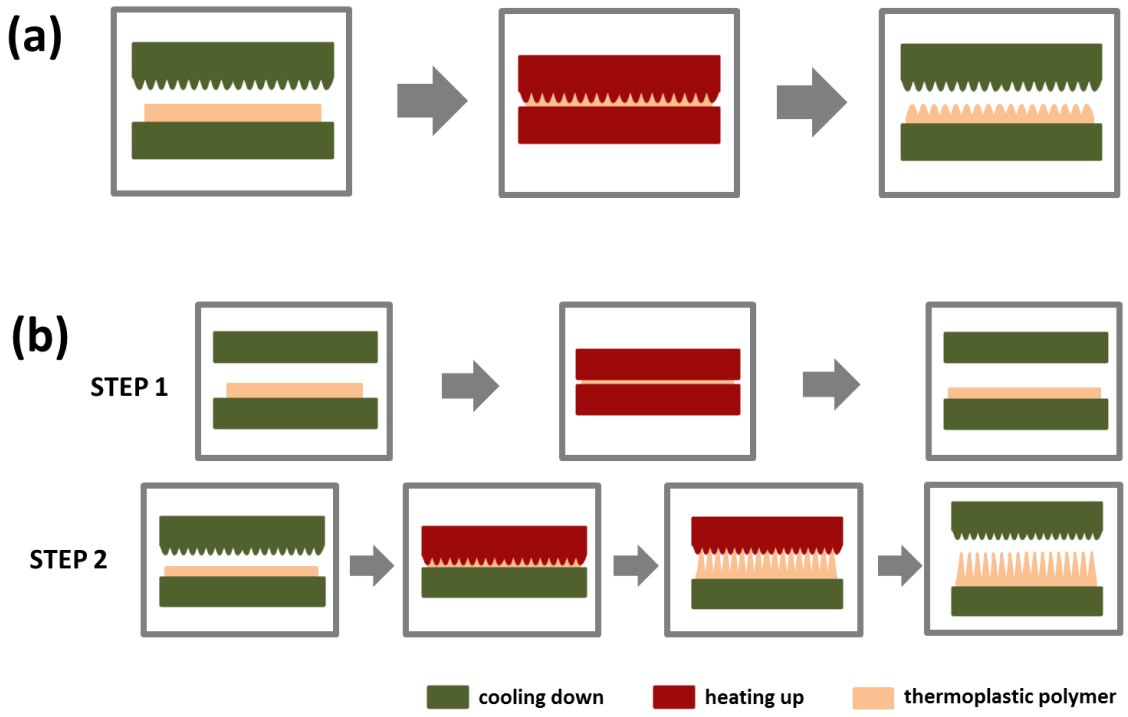

Figure 3-2 Diagrams describing the processes of (a) hot embossing and (b) hot pulling.

A standard hot embossing procedure produced microstructures with a specific feature height defined by the mold layout. To overcome this constraint we employed a two-step hot pulling technique (Figure 3-2b) [84] to fabricate features of different heights from the same mold. In the first step, a normal hot embossing process was completed with a smooth mold to create strong adhesion between the polymer sheet and the demolding plate. To start the second step, the smooth mold was first replaced by the microstructured mold. The thermal nanoimprint started by increasing only the temperature of the mold insert while keeping the temperature constant for the demolding stage with the polymer attached on. The micro-patterns were pressed into the softened polymer at the molding temperature with a defined molding force. The molding platform and the demolding plate were then separated at a steady rate with the temperature of the mold insert remaining above the glass transition temperature of the polymer to pull those features that had already been constructed. At the end of the pulling step, the whole setup was cooled down to ca. 50 °C and the molding tool was opened completely to peel off the samples.

To prepare microstructures of different properties, nickel (Ni) shim molds with specific micro-patterns were selected and prepared for microreplication. Hot embossing and hot pulling process parameters, i.e., embossing temperature, embossing pressure,

demolding/pulling temperature, and pulling speed, were adjusted to obtain desired features (Table 3-1).

Table 3-1 Process parameters of thermal nanoimprint, i.e., embossing temperature, embossing force, demolding/pulling temperature, and pulling speed (Section 4.1 and Section 4.3).

Sample	Type	Embossing temperature (℃)	Embossing force (N)	Demolding/pulling temperature(℃)	Pulling speed (mm/min)
Honeycomb gradient (Section 4.1)	*embossing*	*155*	*40000*	*95*	—
3μm-H (Section 4.3)	*pulling*	*260*	*15000*	*260*	*1*
3μm-L (Section 4.3)	*embossing*	*155*	*1000*	*145*	—
2μm-H (Section 4.3)	*pulling*	*280*	*20000*	*280*	*0.5*
2μm-L (Section 4.3)	*embossing*	*180*	*20000*	*145*	—
230nm-H (Section 4.3)	*embossing*	*170*	*70000*	*145*	—
230nm-L (Section 4.3)	*embossing*	*175*	*5000*	*145*	—

3.1.2 PDMS casting

In order to render the SU8 photoresist mold chemically inert before PDMS casting, the mold surface was fluorinated with tridecafluorooctyltriethoxysilane (TFS; Degussa, Germany) via chemical vapor deposition (CVD). The desiccator was dried in an oven at 105 °C for half an hour. Around 0.5 ml TFS was deposited in a glass dish placed at the bottom of the desiccator and the samples were positioned on a porous ceramic lying above the TFS solution. After applying 0.1 mbar vacuum for 5 min, the desiccator was sealed and stored under room conditions for 2 days. The mold was then rinsed with absolute ethanol and dried with N_2.

Sylgard® 184 Silicone Elastomer (Dow Corning, USA) was used for casting microstructures from the mold. The base and the curing agent (10:1 by weight) were mixed thoroughly in a container by stirring with a glass rod. The capacity of the container should be at least four times higher than the volume of the input mixture. The mixture

was kept in vacuum (< 1×10^{-1} mbar) for around 30 min to remove all entrapped air introduced during the mixing step. Mixture was then poured continuously onto the mold. The coated molds were stored steadily under the ambient conditions for 24 h and then transferred to the oven where the mixture was further cured at 60 °C for 2 h. The casting samples were then peeled off the mold for surface characterization and biological tests.

3.1.3 Fluorocarbon-infused microporous slippery surfaces

Fluorocarbon-infused microporous slippery surfaces were prepared in collaboration with the group of Dr. Pavel Levkin at the Institute of Toxicology and Genetics, Karlsruhe Institute of Technology. All basic chemicals for preparing the microtexture base [poly (butyl methacrylate-co-ethylene dimethacrylate), BMA-EDMA] of the slippery surfaces were ordered from Sigma-Aldrich, Germany. The covalent binding between the polymer and the glass substrate was critical to the homogeneity and stability of the porous microtexture. To create the anchoring sites for the polymer layer, Nexterion® glass slides (Schott, Germany) were first activated by immersion sequentially in 1M NaOH for 1 h and 1M HCl for 30 min, followed by washing with deionized water and drying with compressed air. 3-(Trimethoxysilyl)propyl methacrylate ethanol solution (20 % vol, pH = 5 adjusted with acetic acid) was deposited onto one slide, which was then covered by another slide to assist the spread of the droplets over the whole slide and avoid air bubbles that might be trapped between slides. The solution was reapplied after every 30 min. After 1 h, the slides were washed in acetone and dried with N_2. As shown in Figure 3-3, to create the mold for polymerization, thin strips of Teflon with a thickness of 50 μm (American Durafilm Co., USA) as spacers were placed at the edge of both long sides between two slides and the stacked slides were then fixed with clamps. A mixture of butyl methacrylate (BMA) (20 wt %), ethyleneglycol dimethacrylate (EDMA) (30 wt %), 1-decanol (50 wt %) and 2,2-dimethoxy-2-phenylacetophenone (DMPAP) (1 wt %, with respect to monomers) [94] was injected into the space between the two glass slides. The whole setup was irradiated with UV light (260 nm, 12 mW/cm^2) for 15 min. The slides were then carefully opened with a scalpel. Most of the polymer adhered to the upper glass slide leaving a very thin layer on the bottom slide possibly due to the reduction of UV light intensity through the thickness of the polymer film. The upper slide was then washed intensively with methanol and stored in methanol to remove unreacted monomers insider the microtexture.

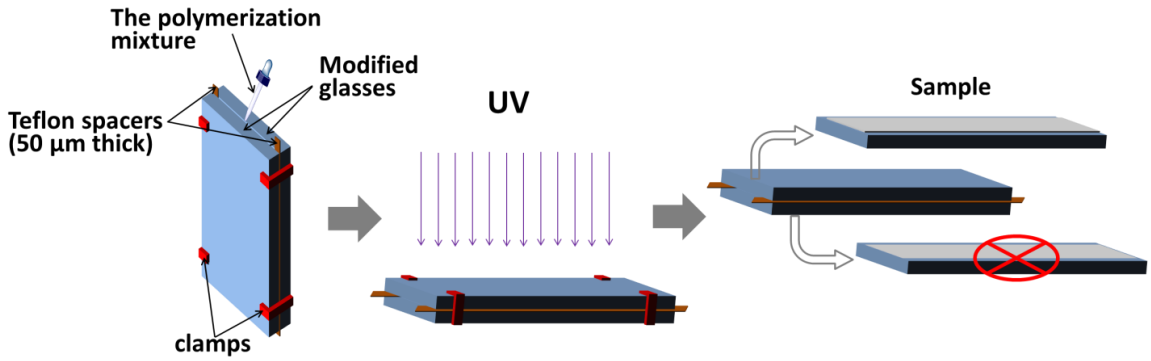

Figure 3-3 Preparation of the microtexture BMA-EDMA layer on a glass substrate via UV-initiated polymerization.

Before applying fluorocarbon lubricants, the slides were removed from methanol and dried with an air gun. An excess amount of perfluorinated liquids (Krytox® GPL 103 and Krytox® GPL 100 from H. Costenoble GmbH & Co. KG, Germany, and Fluorinert® FC-70 from Sigma-Aldrich, Germany) was applied onto the porous BMA-EDMA surfaces respectively. The liquids were maintained on the surfaces overnight to fully saturate the pores inside the polymer layer. Afterwards, samples were tilted vertically for 4 h to get rid of excess fluorocarbon before use in experiments.

3.2 Surface characterization

3.2.1 Scanning electron microscopy (SEM)

The detailed information about the surface morphology was provided by scanning electron microscopy (SEM) measurements. Before imaging, samples (polymer substrates with or without organisms) were coated with a thin layer (~40 nm) of gold or gold/graphite mixture using a sputter coater (Cressington 108 auto; Cressington Scientific Instruments Ltd., UK) to make surfaces electronically conductive, thus preventing the accumulation of electrostatic charge during the scanning. Images were recorded in a LEO1530 Gemini SEM device (Zeiss, Germany) operating at an electron acceleration voltage of 1-2 kV under high vacuum (residual gas pressure < 1×10^{-5} mbar).

3.2.2 Atomic force microscopy (AFM)

Atomic force microscopy (AFM) was applied to examine the surface topography of samples. The analysis of surface topographies was carried out by a MFP-3D BioAFM (Asylum, Germany) in AC-mode using commercial Si_3N_4 cantilevers with a spring

constant of 7.5 N/m (µMasch). The measurement was completed under ambient conditions in a closed loop on all three axes with the tip scanning back and forth at 0° along the horizontal line. Obtained topographic images were analyzed with the software package IGOR (WaveMetrics Inc., USA).

3.2.3 Optical microscopy

A Nikon Eclipse 90i light microscope (Nikon, Germany) with a Nikon DIGITAL SIGHT DS-5Mc camera was applied for the observation and imaging of surface patterns. Images were captured in phase contrast mode with different objective magnifications and processed with Nikon NIS-ELEMENTS AR 3.2 software.

3.2.4 Water contact angle (WCA)

The wettability of surfaces was assessed by water contact angle measurements with a homebuilt contact angle goniometer. Under ambient conditions droplets (around 2-3 µl, Milli-Q water) were deposited on samples by a syringe. Images were acquired using a digital camera and analyzed with either the Program CAM 3.02.01 (Kölsch, P.; Motschmann, H.; Orendi, H.) or the ImageJ software (Rasband, W.) with a Dropsnake plugin. The static sessile water contact angles were measured with the tip of the syringe withdrawn from the droplet. To acquire advancing and receding water contact angles, a constant water application of 12 µl/min was applied. The average was taken from 5-9 measurements with the error bars describing the standard deviations.

3.3 Biological evaluation

3.3.1 Settlement of spores of *Ulva linza*

Spore settlement tests were performed together with the group of Prof. James A. Callow at School of Biosciences in University of Birmingham, UK. Plants of green macroalgae *Ulva linza* were collected from Llantwit Major, Glamorgan, Wales (52°23' N, 3°30' W) 2-5 days before the spring tide. Zoospores were released from the reproductive tips into filtered artificial seawater (ASW, Tropic Marin®, filtered at 0.22 µm) and prepared for the assays. In brief, after being filtered through 3 layers of nylon mesh (100 µm, 50 µm and 20 µm) to remove debris, the spore suspension was stored in a beaker, which was then quickly plunged into ice. Due to the low temperature at the bottom of the beaker maintained by the surrounding ice, although spores swam rapidly towards the bottom,

they would not commit settlement. The concentrated spore suspension at the bottom of the beaker was removed with a pipette and refiltered through two layers of 20 µm nylon mesh. The spore suspension was then diluted with filtered ASW to attain the required concentration according to the experimental design (settlement and growth experiments, 1×10^6 spores/ml; toxicity tests, 7×10^5 spores/ml). The spore suspension was kept on a magnetic stirrer and used in assays within 30 min of release.

Table 3-2 Conditions of spore settlement assays on different surfaces.

Sample type	Pre-incubation	Suspension concentration (spores/ml)	Sample dimension (length×width, cm×cm)	Assay container	Amount of input (ml)	Settlement duration
Honeycomb gradients (Section 4.1)	*In ASW with vibrating for 1 h*	*1×10^6*	*4.5 × 4.5*	*9 cm diameter Petri dishes*	*30*	*45 min*
Discrete honeycombs (Section 4.2)	*In ASW with vibrating for 1 h*	*1×10^6*	*2 × 2*	*5 cm diameter Petri dishes*	*15*	*30 min*
Tapered microstructures (Section 4.3)	*In ASW with vibrating for 1 h*	*1×10^6*	*2 × 2*	*6-well culture plates (ca. 3.5 cm diameter)*	*5*	*45 min*
Slippery surfaces (Section 4.4)	*In ASW with vibrating for 48 h*	*1×10^6*	*7.5×2.5*	*quadriperm dishes (ca. 8.2 cm×3.0 cm)*	*10*	*45 min, 2 h*

Detailed conditions for spore settlement assays on different surfaces are illustrated in Table 3-2. Generally, to ensure the surfaces were fully wetted prior to the settlement assay, samples were pre-incubated in filtered ASW on a vibrating platform (50 rpm) for different durations depending on the physicochemical properties of the samples. Right before the start of the assay, ASW was removed and quickly replaced with the spore suspension to minimize the possibility of drying.

Spore suspension was added into the assay dishes containing the samples. The amount of suspension for each sample was determined by both, the dimension of the sample and the volume of the assay container. The dishes were incubated in the dark at

room temperature (ca. 20-22 °C) for 45 min [95] or in some cases for 30 min or 2 h. The samples were then washed in filtered ASW to remove motile spores (i.e., spores that had not settled and undergone permanent attachment), by gently passing the samples 10 times through a beaker of ASW. The samples were then fixed in 2.5% glutaraldehyde in ASW for 20 min, followed by sequential washing in ASW, 50% ASW and deionized water, and subsequently air-drying. Settlement assays with different batches of spores were conducted to confirm the reproducibility of the data.

Spores settled on substrates were visualized and counted by autofluorescence of chlorophyll using an AxioVision 4 image analysis system attached to a Zeiss epifluorescence microscope (20× objective; excitation and emission wavelengths: 546 and 590 nm, respectively). For some microstructured samples (e.g., honeycomb gradients on PMMA), it was not possible to assess the settlement using automated image analysis as the pattern itself was autofluorescent leading to exaggeration of cell numbers. Therefore, attached spores were viewed under transmitted light and counted by eye from fields of view projected onto a computer screen. Spore settlement density is expressed in cells·mm^{-2}. Reported values are the mean (± standard errors) of the data (normally 80-90 counts) collected from a number of replicates (at least 3 replicates of each sample type). Repeating settlement assays with different batches of spores were conducted to verify the reproducibility of the results.

3.3.2 Attachment of the diatom *Navicula incerta*

Diatom attachment assays were completed together with the group of Prof. James A. Callow at School of Biosciences in University of Birmingham, UK. As diatoms do not have flagella to support the active exploration of surfaces before committing settlement, they are passively brought into the vicinity of surfaces by gravity or water flow. Before applying external hydrodynamic force, the cell density appears to be similar on all substrates irrespective of the surface properties. The initial attachment of diatoms was therefore assessed after a washing step to remove unattached or weakly attached diatoms. As a consequence, the resulting density actually revealed the ability of diatoms to attach firmly on a specific surface.

After 3 days' culture in F/2 medium in an illuminated incubator (75 µmol photons·m^{-2}·s^{-1}) at 18 °C, cells of *Navicula incerta* were washed three times and resuspended in fresh medium. The diatom suspension was then filtered through two

layers of 20 µm nylon mesh and diluted with ASW (Tropic Marin®) to obtain a concentration with ca. 0.25 µg/ml chlorophyll *a*. Settlement conditions on different surfaces are listed in Table 3-3. In general, to perform the settlement assay, a certain volume of cell suspension was added onto the samples. After 2 h of incubation at room temperature (ca. 20-22 °C), the samples were rinsed by passing 10 times through ASW in a beaker. Samples were subsequently fixed with 2.5% glutaraldehyde in ASW and washed sequentially in ASW, 50% ASW and deionized water, and subsequently air-drying. Attached diatoms were visualized through the autofluorescence of chlorophyll with an AxioVision 4 image analysis system attached to a Zeiss epifluorescence microscope (20× objective; excitation and emission wavelengths: 546 and 590 nm, respectively). The number of settled diatoms was counted in 20-30 fields of view on each replicate (3-4 replicates of each sample type). The results are expressed as the mean number (± standard errors) of settled diatoms per square millimeters. Settlement was repeated with different batches of diatoms to confirm the reproducibility of the data.

Table 3-3 Conditions of diatom attachment assays on different surfaces.

Sample type	Pre-incubation	Concentration of chlorophyll *a* (µg/ml)	Sample dimension (length×width, cm×cm)	Assay container	Amount of input (ml)	Settlement duration
Discrete honeycombs (Section 4.2)	*In ASW with vibrating for 1 h*	*0.25*	*2×2*	*5 cm diameter Petri dishes*	*15*	*2 h*
Tapered microstructures (Section 4.3)	*In ASW with vibrating for 1 h*	*0.25*	*0.5×0.5*	*6-well culture plates (ca. 3.5 cm diameter)*	*5*	*2 h*

3.3.3 Settlement of barnacle cyprids of *Balanus amphitrite* and *Balanus improvisus*

Cyprid settlement assays were conducted together with the group of Prof. Anthony S. Clare at School of Marine Science and Technology in Newcastle University, UK. Cyprids of *Balanus amphitrite* and *Balanus improvisus* were cultured as described in the literature [17, 96]. Before settlement, cyprids (*Balanus amphitrite*: 3-day

post moult from the 6th-stage nauplius larva; *Balanus improvisus*: 0-day post moult from the 6th-stage nauplius larva) were stored in a refrigerator at ~6 °C. One droplet of approximately 0.5 ml freshly filtered (filtered at 0.22 µm) seawater (cyprids of *B. amphitrite*) or artificial seawater (Tropic Marin®; cyprids of *B. improvisus*) containing around 15-20 cyprids was placed on the surface of each replicate. After incubation for 48 h in darkness at 28 °C, the amount of settled cyprids was quantified under a light microscope. The percentage of settlement was calculated as the ratio between the number of settled cyprids and the total number of cyprids. The reported values are the average of the data collected from six replicates of each sample type with the error bars showing the standard errors. Experiments were repeated with different batches of cyprids to confirm the reliability of the data.

3.3.4 Removal of sporelings of *Ulva linza*

Sporeling removal tests of slippery surfaces (Section 4.4) were performed together with the group of Prof. James A. Callow at School of Biosciences in University of Birmingham, UK. To assess the fouling-release capability of the coatings with a reasonable accuracy, a minimum amount of biomass was required to be present on the samples before being exposed to a shear stress in a removal experiment. Therefore, spores were allowed to settle (attach) on samples for 2 h in darkness as described in Section 3.3.1. The suspension with unsettled spores was gently removed with a pipette and growth medium [97] was carefully added without disturbing the settled spores. Samples were then transferred to an illuminated incubator at 18 °C with a 16:8 light: dark cycle (45 µmol photons·m^{-2}·s^{-1}). The medium was exchanged every two days.

After growing for 7 days, the attached sporelings were quantified in a plate reader as described in the literature [98]. The RFU value of each replicate was the mean taken from 70-point readings along the center region of the sample (in a 10×7 grid covering an area of ca. 4 cm^2). Samples were then exposed to a wall shear stress of 50 Pa in a flow channel [99] for 5 min and the remaining biomass was quantified again. Percentage removal of biomass was determined by the RFU values before and after flow, where $\%\mathbf{removal} = \frac{\mathbf{RFU}_{\mathrm{before}} - \mathbf{RFU}_{\mathrm{after}}}{\mathbf{RFU}_{\mathrm{before}}} \times 100\%$. The mean percentage removal from six replicates of each sample type is reported with the error bars representing 95% confidence intervals.

3.3.5 Field test

The field test of slippery surfaces (Section 4.4) was performed in collaboration with partners in International Paint, AkzolNobel, UK. Samples of microscope glass size were adhered on the immersion test board using an epoxy adhesive. When the glue was fully cured, an acrylic tiecoat was applied around the samples on the board. Following the drying of the tiecoat, the area around the testing surfaces was coated with an addition layer of blue top coat Intersleek® 970. The testing board was then immersed in Hartlepool, UK (International Paint immersion test facility). The percentages of different types of fouling (i.e., micro-fouling, weed, soft-fouling and hard-fouling) were assessed by eye and images of the testing board were taken after 3 weeks, 5 weeks and 5 months of immersion, respectively. Averages were obtained from 10 replicates per each sample type.

3.4 Other related methods

3.4.1 Spectral ellipsometry

The thickness of thin organic films was determined by a spectral ellipsometer M44 (J. A. Woollam, USA). With a high pressure Xenon lamp serving as the light source, the instrument was operated at a wavelength between 280-800 nm. The thickness of the PEG2000 self-assembly monolayers (SAMs) surface, which was included as a standard in the slippery study (Section 4.4), was determined to be 61±10 Å using a single Cauchy model layer with a fixed refractive index of 1.45. The consistency with values reported [100, 101] suggested the successful assembly of the monolayer. The reported values are the average taken from 9 measurements (measurements of 3 distinct spots on each of the 3 replicates) and the errors are the standard deviations of the data set.

3.4.2 Stability test

The stability test of slippery surfaces (Section 4.4) was done together with the group of Dr. Pavel Levkin at the Institute of Toxicology and Genetics, Karlsruhe Institute of Technology. Samples were immersed in filtered artificial seawater (ASW, Instant Ocean®; filtered at 0.22 µm) or filtered seawater (filtered at 0.22 µm) on a shaking table at 50 rpm. The static, advancing and receding water contact angles were measured after 1 h, 3 h, 18 h, 1 day, 2 days, 7 days, 9 days, 14 days, 21 days and 28 days of incubation. The

expressed values are the average of 9 measurements with the error bars representing the standard deviations.

3.4.3 Toxicity test

The toxicity test was done together with the group of Prof. James A. Callow at School of Biosciences in University of Birmingham, UK. Samples from the slippery study (Section 4.4) were incubated in 10 ml ASW (Tropic Marin®; filtered at 0.22 µm) in separate compartments of Quadriperm dishes (Greiner Bio One, UK) on a shaker (50 rpm) at room temperature (20-22 °C). After 48 h the ASW (leachate) was pipetted from the dishes and replaced with fresh ASW. The leachates collected after 48 h preincubation from three replicates of each type of sample were tested in a toxicity assay.

One milliliter of freshly released spores (7×10^5 spores/ml) in double strength enriched seawater medium (400 µl nutrients / 10 ml ASW) [97] was mixed with 1 ml leachate or 1 ml ASW (control) in 24-well plates. The plates were incubated in darkness for 2 h at room temperature (ca. 20-22 °C) and then transferred to an illuminated incubator with a 16:8 light:dark cycle (45 µmol photons$\cdot m^{-2}\cdot s^{-1}$) at 18 °C. After 5 days of growth, the medium was removed from the wells. Biomass in the wells was quantified as extracted chlorophyll *a* by adding 1 ml dimethyl sulfoxide (DMSO) into each well. The plates were incubated in darkness for 30 min and 200 µl solution from each well was pipetted into a 96-well plate. Fluorescence of the DMSO extracts was read in a plate reader (Tecan GENios Plus; excitation at 430 nm, emission at 670 nm) connected to a computer with Magellan v.4.00 software. All plates were read from the top, and the readings were based on four spot readings per well, taken in a 2×2 grid. The results were expressed as the relative fluorescence units (RFU). The reported data are the average from 3 replicates with ASW as the control, and error bars show the standard errors. The test was repeated to verify the reliability of the results.

3.4.4 Statistical analysis

The analysis was done together with partners from the group of Prof. James A. Callow at School of Biosciences in University of Birmingham, UK and the group of Prof. Anthony S. Clare at School of Marine Science and Technology in Newcastle University, UK. Biological data were tested for normality using Anderson-Darling test in the software Minitab 15. If the data conformed to normality, differences between the

surfaces were determined by one-way ANOVA with pairwise Tukey comparison test. If the data did not conform to normality, they were analyzed by Kruskal Wallis with post-hoc Dunn's multiple comparison test in the software GraphPad to determine the differences between surfaces [102, 103] . A *p*-value of < 0.05, is considered to be statistically significant. The complete set of analysis is presented in the supporting information in appendix (Section 6.1).

4 Results and Discussion

Scanning biological reactions with respect to a succession of surface properties could be realized on gradient surfaces. In Section 4.1, gradients of honeycomb pits were constructed via hot embossing. Across the gradient feature size (ca. 1-10 μm) and feature spacing changed simultaneously, while the distance between centers of every two adjacent honeycombs remained constant. The fouling responses of spores of *Ulva linza* were examined on these gradient surfaces to investigate the correlation between spore settlement and topographic cues and determine the minimum pit size to accommodate spores.

However, to interpret experimental observations in greater detail and avoid the possible influence on fouling responses by the gradient itself, a series of structured surfaces with a single variable provides an additional option. As depicted in Section 4.2, a series of honeycomb pits with the feature size as the single variable (ca. 2.5-250 μm), were designed and patterned on SU8 photo-resist molds for PDMS casting. Homogeneous honeycomb microstructures of a specific size were produced in an individual region (2×2 cm^2). Attachment of spores of *Ulva linza*, the diatom *Navicula incerta* and cyprids of *Balanus improvisus* was studied on these discrete honeycombs to obtain a better understanding of the size preference of different fouling organisms.

Sufficient contact at the cell-substrate interface is fundamental to the survival of marine colonizers to achieve solid adhesion against external hydrodynamic forces. To avoid sites preferred by fouling organisms, i.e. corners formed by two perpendicularly joined planes, and meanwhile to diminish the outmost surface area, cone-like tapered microstructures with different feature periods and feature heights were fabricated (Section 4.3) via hot embossing and hot pulling. The settlement results of *U. linza* spores and *Navicula incerta* diatom cells were examined for their correlation with different topographic cues, namely Wenzel roughness and the attachment point.

Sections 4.1-4.3 concentrated on the direct interaction between surface topographies and fouling organisms. As it is likely that the most successful antifouling coatings are the outcomes of multifunctional designs, in Section 4.4 slippery liquid-infused porous surfaces (SLIPS) were constructed by generating the surface lubricity on the basis of surface microtopographies. Porous microstructures were prepared via UV-initiated polymerization and subsequent infusion of fluorocarbon lubricants into the polymer microtexture produced a series of slippery surfaces. The antifouling and fouling-

release performance of these SLIPS surfaces was tested against the settlement of both *Ulva* zoospores and *Balanus amphitrite* cyprids and the removal of sporelings of *Ulva linza*, respectively. Furthermore, the performance of these SLIPS surfaces in the field was examined after immersion in the ocean for different lengths of time.

4.1 Influence of topographic gradients on *Ulva* settlement

Surface topography has been recognized as one of the key factors that influence cell-substrate interaction [104]. To study the antifouling impact of topography, gradient surfaces are particularly powerful tools [105, 106]. With position-bound and gradually changing topographies on the same surface, high-throughput and cost-effective analysis of the responses of fouling organisms can be realized in a single experiment on gradient samples. The derived information should inspire novel coatings design.

Since the first gradient surface was described in the 1960s [107], many new approaches have contributed to this field in order to produce gradients of different properties (wettability, chemistry, topography, etc.) [108-110]. However, besides the investigation of *Ulva* spores on wettability gradients [111] and hierarchically wrinkled coatings [112], there have been few applications in relation to marine antifouling.

In this Section, we aimed to develop an understanding about the response of spores of *U. linza*, one of the major soft-fouling species, to a range of continuously changing microtopographies using a morphological size gradient. Gradients of honeycomb pits were constructed on polymethylmethacrylate (PMMA) by hot embossing. The feature size of microstructures along the gradient covers the range between 1 and 10 µm which is especially interesting for zoospores of *Ulva linza*. The influence of topographic properties, i.e., Wenzel roughness and local binding geometry, on the settlement behavior of spores was closely examined. Additionally, the minimal pit size to accommodate spores was determined.

4.1.1 Characterization of ‘honeycomb’ size gradients

The ‘honeycomb’ gradient layout is depicted in Figure 4-1a. The hexagonal microstructures appeared as pits on PMMA slides with the feature size (the width of the hexagon in *x* direction in Figure 4-1a) changing continuously in micrometer step from 1 µm to 10 µm along the gradient, while the distances between the centers of adjacent hexagons remained the same (10.00 µm along the *x* axis and 11.58 µm along the *y* axis in Figure 4-1a). Six structured regions (Figure 4-1b) were patterned on each PMMA sample with smooth areas lying inside between, which served as the control for bioassays.

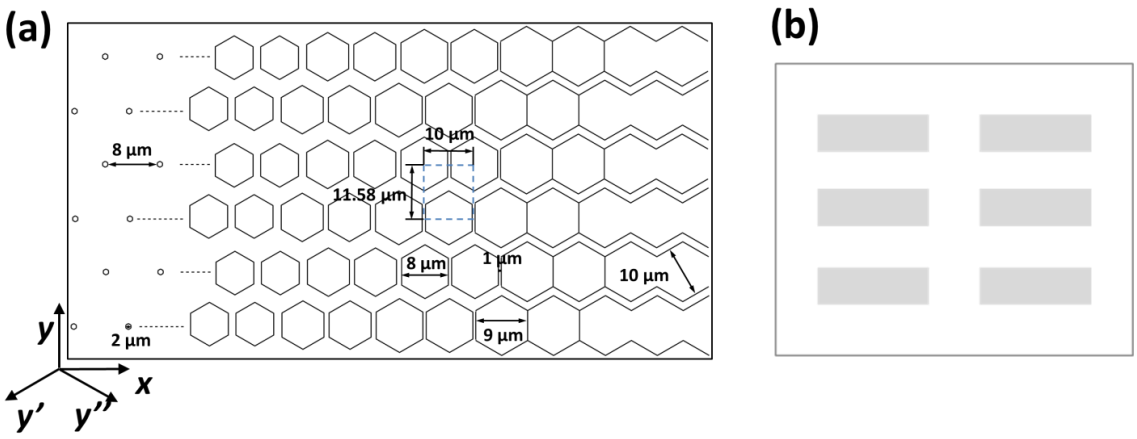

Figure 4-1 (a) Schematic illustration of the 'honeycomb' gradient microstructures. The gradient is based on the honeycomb motif and consists of hexagonal pits. To the left pits are getting smaller until they reach a minimal size of 1 µm. On the right hand side, as the size of the pits gets larger and finally exceeds a critical diameter, the structure converts into a zigzag pattern. The small circles on the left side of the gradient resemble the symmetry of the centers of the hexagonal pits and their corresponding characteristic distances. (b) Sketch of the hot-embossed PMMA 'honeycomb' gradient replicate (The gray structured areas are 1.512 cm×1 cm, and the full dimensions of the samples are 4.5 cm × 4.5 cm.).

PMMA gradient samples were prepared via hot embossing as described in Section 3.1.1 in collaboration with the group of Dr. Hendrik Hölscher at IMT, KIT. Microstructures were analyzed under phase contrast microscopy (Figure 4-2). The size of the hexagonal pits increased across the gradient. As the rims in *y*-direction (Figure 4-1a) were slightly thinner compared to the other two directions (*y'* and *y''*), they became smaller and eventually disappeared with the increasing diameter of the hexagons, and the surface pattern transformed into zigzag microstructures. The depth of the hexagonal pits measured by AFM was 1.57 ± 0.08 µm across the whole gradient. Static water contact angle (WCA) measurements showed that the smooth area between the microstructures had a contact angle of ca. 77°. Across the gradient the value changed from 77° to 109° with increasing size of the hexagons. This increase was expected, as larger structures normally had a higher roughness which caused larger WCAs.

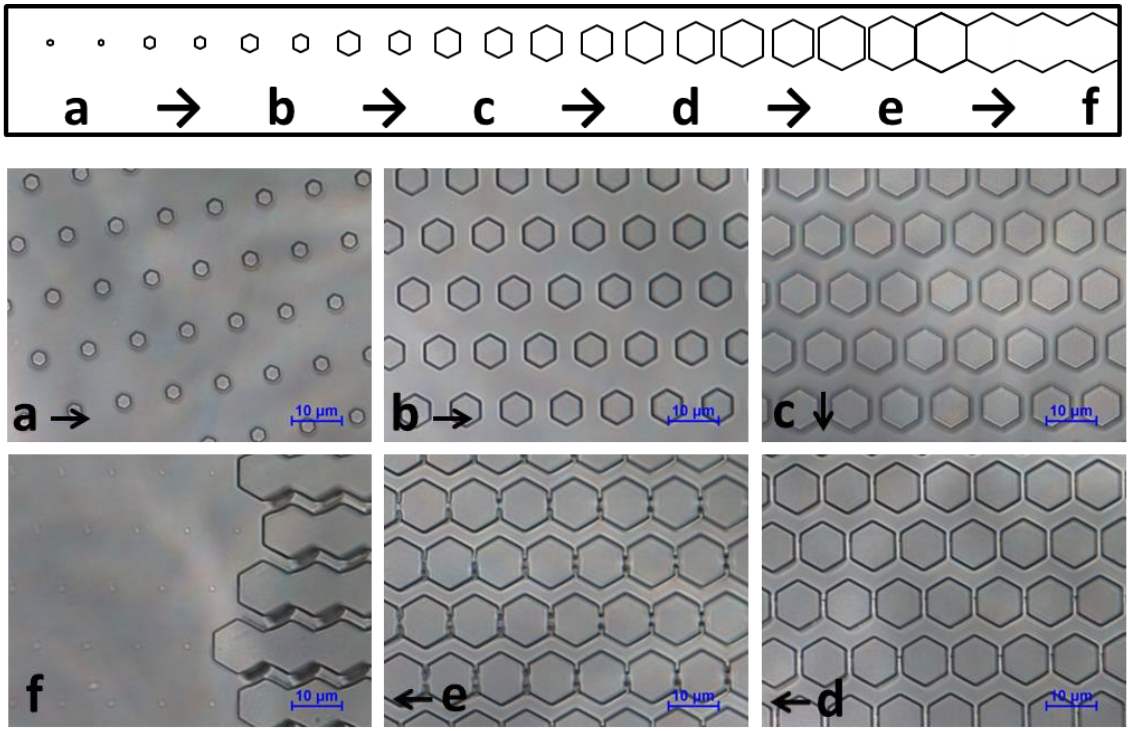

Figure 4-2 Top-down phase contrast microscopic images of the 'honeycomb' gradient topography on PMMA. The size of the hexagonal microstructures increases gradually (following the order of a→b→c→d→e→f).

4.1.2 Correlation between Wenzel roughness and spore settlement on morphological gradients

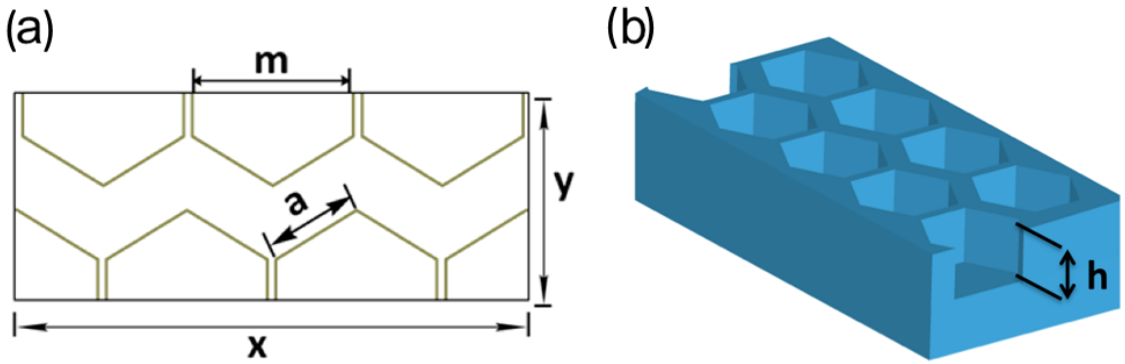

Figure 4-3 (a) Schematic representation of the repeating unit of hexagonal microstructures. The distances between neighboring hexagonal pits are fixed across the gradient with **x**/3=10 µm (in *x* direction) and **y**=11.58 µm (in *y* direction), while **m** (the width of the hexagon in *x* direction or the diameter of the inscribed circle of the hexagon) and **a** (the side length of the hexagon) change according to the size of the features and are related with $\mathbf{a}=\frac{\sqrt{3}}{3}\mathbf{m}$). (b) The roughness factor increases with the height of the structures **h** due to the increased wall area.

To examine the correlation between the surface topography and spore settlement, the Wenzel roughness along the gradient was calculated using the variables introduced in Figure 4-3, where **x** and **y** represented respectively the length and width of the extracted unit, **m** described the width of the hexagonal pit, while **a** was the side length of the hexagon. In Figure 4-3b, **h** stranded for the height of the microstructures. The Wenzel roughness was defined as the ratio between the actual surface area and the geometric surface area [92]. The actual surface area was the sum of projected surface area and wall area. As the microstructures changed from hexagons to zigzag, the number of walls belonging to each hexagon decreased from six to four. Therefore, two sets of formulae (equation 1 and equation 2) were applied to calculate the Wenzel roughness factor for these two distinctive regions, i.e., the hexagonal region and the zigzag region, respectively. For hexagonal microstructures (image a-e in Figure 4-2),

$$\mathbf{r}_{\mathrm{Wenzel}} = \frac{\mathrm{S_{actual}}}{\mathrm{S_{geometric}}} = \frac{\mathrm{S_{geometric}} + \mathrm{S_{wall}}}{\mathrm{S_{geometric}}} = \frac{\mathbf{xy}+18\mathbf{ah}}{\mathbf{xy}} = 1 + \frac{10\sqrt{3}}{579}\mathbf{mh} \qquad (1)$$

While for zigzag microstructures (image f in Figure 4-2),

$$\mathbf{r}_{\mathrm{Wenzel}} = \frac{\mathrm{S_{actual}}}{\mathrm{S_{geometric}}} = \frac{\mathrm{S_{geometric}} + \mathrm{S_{wall}}}{\mathrm{S_{geometric}}} = \frac{\mathbf{xy}+12\mathbf{ah}}{\mathbf{xy}} = 1 + \frac{20\sqrt{3}}{1737}\mathbf{mh} \qquad (2)$$

Following the preincubation of samples in ASW for 1 h, spores were settled on gradients for 45 min as described in Section 3.3.1. Due to the autofluorescent effect of the structured PMMA, spores were counted by eye under the light microscope. Three transects, corresponding to thirty-one fields of view, along each gradient were counted. Counts were recorded in an area of 0.038 mm^2 at 0.5 mm intervals along the *x* axis of the gradient (Figure 4-1a). The three cell counts (top, middle, and bottom) taken at each of the 31 points along the gradient were averaged to give a mean value (n=3) for each patch of gradient. For the background (smooth PMMA control), 31 counts were made along each of the three transects of 15 mm length on the smooth area of the wafer. The results are expressed in cells·mm^{-2} with respect to the size of micro-hexagonal pits. Reliability of the data was verified in repeating experiments with two additional batches of spores which yielded the same trends.

The density of settled spores on different sections of the morphological gradient was quantified (Figure 4-4), resulting in curves from five individual replicates patterned on the same PMMA wafer. As shown in Figure 4-4, spores attached at a higher density on

the structured area than the smooth background. The number of settled spores was found to be gradually reduced with decreasing size of the hexagonal pits. The reduction started to become apparent when the size of microstructures went below the size of motile spores (a diameter of approximately 4-5 µm at the widest part of the pyriform spore). In the other direction, as the size of the pits exceeded a diameter of 8.5 µm, the structures changed from hexagons to zigzag walls. Along with the structural change, a dramatic decrease in spore settlement was found. A closer inspection of the microscopic images revealed that the spores preferred to settle against edges in the structures rather than in the middle. The gray area in Figure 4-4 represented the change in Wenzel roughness factor across the gradient, which showed a close correlation with spore settlement up to the point where hexagons converted into zigzag structures.

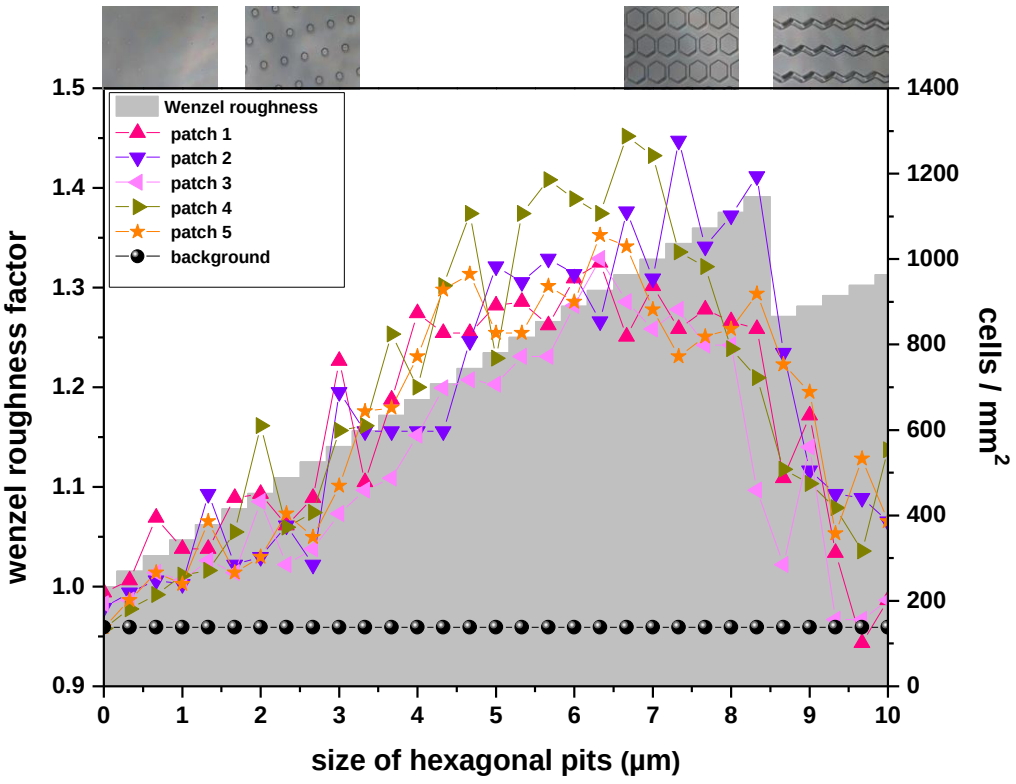

Figure 4-4 Settlement density of spores of *U. linza* graphed against the Wenzel roughness (gray columns) across the gradient. Mean cell counts for 5 individual patches on one wafer; each point is the mean of three transects (top, middle and bottom); counts are taken at 0.5 mm intervals along the gradient. The reported settlement density on the smooth control is the average of 93 counts.

Since the Wenzel roughness factor was introduced [92], it has been applied to a range of different studies. Developed by Brennan's research group [16, 74, 75], the dimensionless Engineered Roughness Index (ERI) was used to correlate surface topographic properties with biofouling. For the specific microstructure dimensions (feature spacing=2 μm and feature depth=3 μm), the spore settlement was inversely linear to the ERI. In both ERI equations (ERI_I and ERI_{II}, equation 3-4), Wenzel roughness (**r**) was proportional to ERI. Besides **r**, both ERI_I and ERI_{II} also took into account the depressed surface area fraction ($1-\boldsymbol{\varphi_s}$). The degree of freedom (d***f***) to move on the surface was considered in ERI_I, while d***f*** was replaced by the number of distinct features (**n**) in the ERI_{II} equation.

$$ERI_I = \frac{\mathbf{r}\cdot d\boldsymbol{f}}{1-\boldsymbol{\varphi_s}}, \qquad ERI_{II} = \frac{\mathbf{r}\cdot\mathbf{n}}{1-\boldsymbol{\varphi_s}} \tag{3, 4}$$

Interestingly, our results on the hexagonally structured morphology gradients revealed a trend of increasing settlement with increased Wenzel roughness (Figure 4-4). This was in contrast to the general ERI models which predicted lower settlement with increased Wenzel roughness, although only for microstructures of feature size/spacing of 2 μm [16]. In the present study even topographies based upon 2 μm stimulated settlement. On surfaces with a size gradient it was difficult to determine the number of 'unique features' at each point. Moreover, the Wenzel roughness factor and depressed surface area fraction changed simultaneously across the gradient. Hence it was not possible to describe the surface topographic features of the present study by the ERI models and the mechanistic basis of the difference in the response of spores to topographies in these different studies was not known. It was possible that the presence of the gradient modified responses of spores since the results of previous studies on gradients (albeit gradients of wettability rather than topography) generated some unexpected results [111]. Thus, the settlement of spores of *Ulva* on surfaces with homogeneous topography was substantially different to settlement on equivalent topography when presented as part of a gradient.

4.1.3 Influence of local binding geometry on spore settlement

A steep drop in spore settlement density was found when the structure changed from hexagon to zigzag (hexagonal size of ~8.5 μm, image e→image f in Figure 4-2). Scanning electron microscopic (SEM) images revealed that spores preferentially settled in

the ‘kink sites’ (Figure 4-5a). The number of ‘kink sites’ in the hexagonal area was 3 times larger compared with the zigzag area. Interestingly, the spore settlement density was also reduced to approximately one third in the zigzag area. As shown in Figure 4-4, the change in spore settlement density was larger than that expected from the change in Wenzel roughness. Thus, a further detailed investigation of SEM images was carried out in which the settled spores were classified according to their settlement positions. Figure 4-5c shows the change in the number of all attached spores, spores at ‘kink sites’ and ‘non-kink sites’ as the microstructures transform from hexagons to zigzag walls. The difference between a ‘kink site’ and a ‘non-kink site’ was that three instead of two side walls were available for binding (Figure 4-5a and Figure 4-5b). Figure 4-5c showed that during the transition from hexagon to zigzag, the decrease in the number of settled spores was mainly caused by the reduction of spores at ‘kink sites’, while the number of spores at ‘non-kink sites’ remained almost the same. Therefore, SEM provided a substantial proof of the ‘kink site’ effect. This gave rise to the interpretation that spores were able to detect sheltered pits and kinks on the surface and these sites facilitated settlement. A similar preference was also observed for barnacle larvae, which exhibited strongly enhanced settlement on microstructures larger than the size of the cyprids providing maximum anchoring sites [66].

Spores of *U. linza* are pear-shaped while swimming and will assume a spherical shape after they commit to settlement. ‘Kink sites’ provided more attachment points, which supported the firm adhesion of spores against external hydrodynamic forces (Figure 4-5b). This adhesion was facilitated by the endocytotic fusion and discharge of membrane-bound adhesive vesicles with the plasma membrane of the spore to contact the surface [113]. The area available to be spread by the adhesive determined the effective contact area, which obviously was maximized at a ‘kink’ position. This situation was qualitatively comparable with the ‘half-crystal position’ or ‘Terrase ledge kink’ site in crystal growth on solid interfaces [114].

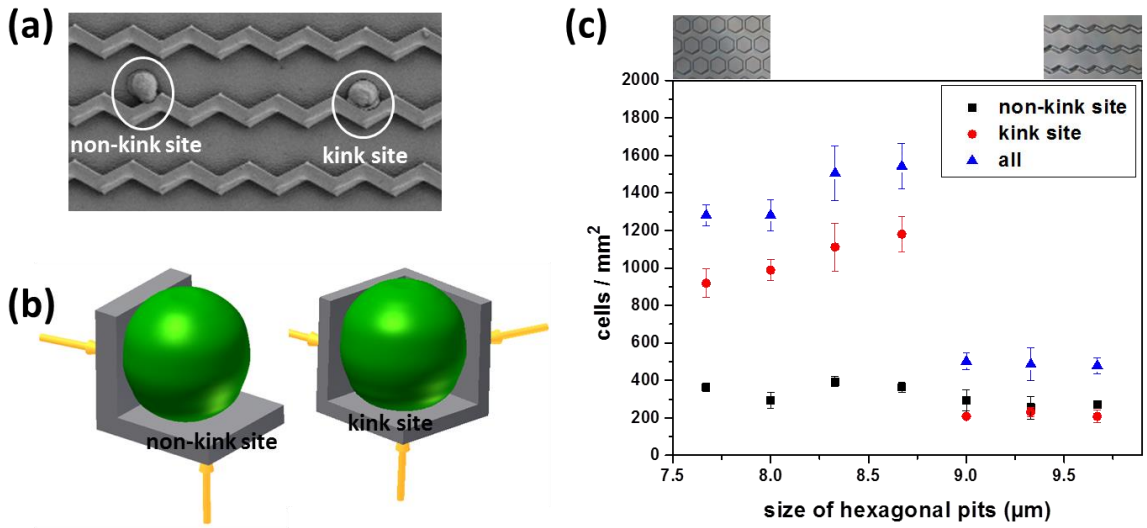

Figure 4-5 (a) A SEM image showing *Ulva* spores settled against a 'non-kink site' and a 'kink site' (b) Sketch of local binding geometry of settled spores at a 'non-kink site' and a 'kink site'. (c) Mean cell counts of spores at different binding geometries during the gradient transition from hexagon to zigzag; each point is the average of three counts taken at 0.5 mm intervals along the gradient with the error bars showing the standard errors.

By analyzing SEM images in greater detail, the smallest size of the pits that spores could enter and settle in, could be determined. Visual analysis of the images showed that if spores did not fit in the pits, they tended to settle asymmetrically and slightly displaced from the center of the pits. The same was observed if the pits were too large as spores tended to populate 'kink sites' in the pits. This observation was quantified from SEM images (Figure 4-6) by measuring the distance between the center of the settled spore and the center of the nearest pit. A gradual decrease in the displacement was found when the size of the pits increased up to approximately 2.0 µm. A steep drop in the displacement to nearly zero was found at a pit size of 2.6 µm, where spores were able to squeeze themselves into the pits. Spores remained in the center of the pits until the size of the pits increased to around 5 µm. Spores could be found sitting snugly when the size of the pits got closer to the dimension of the widest region of the swimming spores (ca. 4-5 µm). When the size of the hexagons increased further, spores tended to attach to the corners of the pits rather than adhere in the middle and the displacement again increased. Thus, the minimum size of the pits across the gradient which spores could fit in was about 2.6 µm, which was slightly smaller than the mean diameter of swimming spores (ca. 4-5 µm). Spores could fit into the 2.6 µm diameter pits because they were pear-shaped at the time

they committed to settlement. After attaching, the spores became round and more compact in the pits.

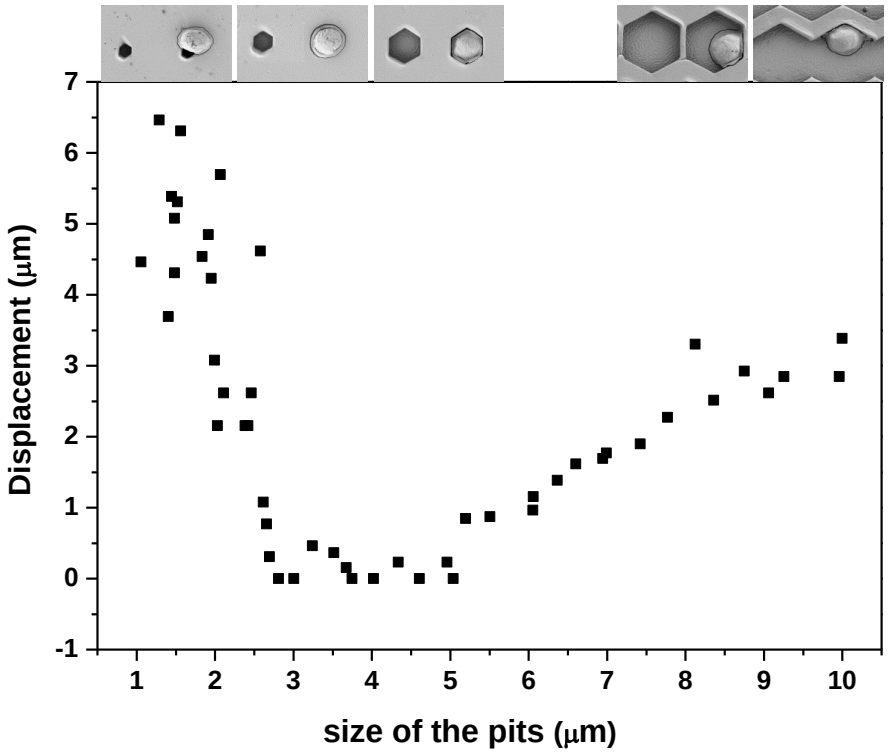

Figure 4-6 Distance between the center of the settled spore and the center of the nearest pit at different positions along the gradient.

4.1.4 Conclusions

Summarizing, morphological gradients allowed the influence of topographic cues on the settlement of spores to be studied systematically. A close correlation between spore settlement and Wenzel roughness **r** was observed. The specific role of the 'kink site' revealed the importance of the local binding geometry as spores selectively populated these sites. And in agreement with previous notion our gradient studies also showed that spores preferred topographies of a size similar to or slightly larger than their body size [14, 32]. Moreover, the smallest size of pits occupied by spores was determined to be 2.6 μm. This value was in line with previous studies showing that remarkably reduced settlement was found on smaller microstructures (e.g., 2 μm) [15].

4.2 Influence of feature size on settlement of fouling organisms

In our previous study using honeycomb gradients (Section 4.1), settlement of spores was guided by the Wenzel roughness factor and the local binding geometry. The gradient is a simple yet powerful tool to investigate biological reactions in relation to a series of surface properties. However, in some cases, e.g., the settlement of barnacles, interpretation of the data turned out to be difficult for two reasons. First, extended exploration was found throughout the gradient potentially guiding the cyprid behavior in a certain direction along the gradient. Secondly, it was difficult to place the droplet on the gradient in order to restrict the movement of the cyprid to a well-defined area and thus to avoid its settlement at edges or at the smooth interface. To be able to offer large areas of homogeneously structured material, to quantitatively interpret experimental observations with respect to local structural features, and to avoid the possible influence of responses to the gradient itself, a series of surfaces with ca. 2 cm × 2 cm of homogeneously structured areas were investigated. The series of microstructures with different feature sizes were designed and fabricated on PDMS substrates via soft lithography, each sample possessing a pattern of honeycomb pits of a specific size. The size of honeycomb pits on the ultimate PDMS, being the only variable in this study, ranged from ca. 2.5 µm to ca. 250 µm. Size preference of spores of *Ulva linza*, the diatom *Navicula incerta* and cyprids of *Balanus improvisus* was investigated.

Compared to the honeycomb gradient, there were several distinctive characteristics on this new topographic design. First, such discrete honeycomb topographies were constructed on polydimethylsiloxane (PDMS; E_{Young}=1.57 MPa) via soft lithography instead of on polymethylmethacrylate (PMMA; E_{Young}=2.43 GPa) via hot embossing (Table 6-1). Second, symmetrical hexagons of a specific size were patterned on each individual sample rather than in a gradient. Third, instead of two variables (feature size and feature spacing) on the gradient surface this set of discrete honeycombs had the feature size as the only variable. Besides these, the size range of the hexagon units was also increased to target more fouling species of interest.

4.2.1 Design and characterization of discrete honeycombs

The layout of the microstructure design is shown in Figure 4-7a. The full dimension of the mask was 5×5 inch^2 (127×127 mm^2). Sixteen structured regions were centered in the circular area (radius R=2 inch (50.8 mm)). The size of the larger squares (1-12) inside the circle was 20×20 mm^2. And the size for the smaller squares (a-d) was 10.5×10.5 mm^2. There were 2.8 mm wide gaps between adjacent squares. Siemens stars (resolution test) and group logos were present in the smaller squares. For the larger squares (1-12), each one was covered with a symmetrical hexagonal pattern (part of it shown in Figure 4-7b). To produce the whole series of microstructures, we changed the size of the hexagonal features (inner width of the hexagon e.g. for region 2: **W**=3 µm), while keeping the thickness of the bars constant (**d**=1 µm). Table 4-1 shows the parameters of microstructures in different regions of the mold (1-12). This design covered the interesting scales for a variety of fouling species (**W**=2-250 µm). Despite the change in the feature size, the feature spacing was kept constant, thus restricting the study to a single variable.

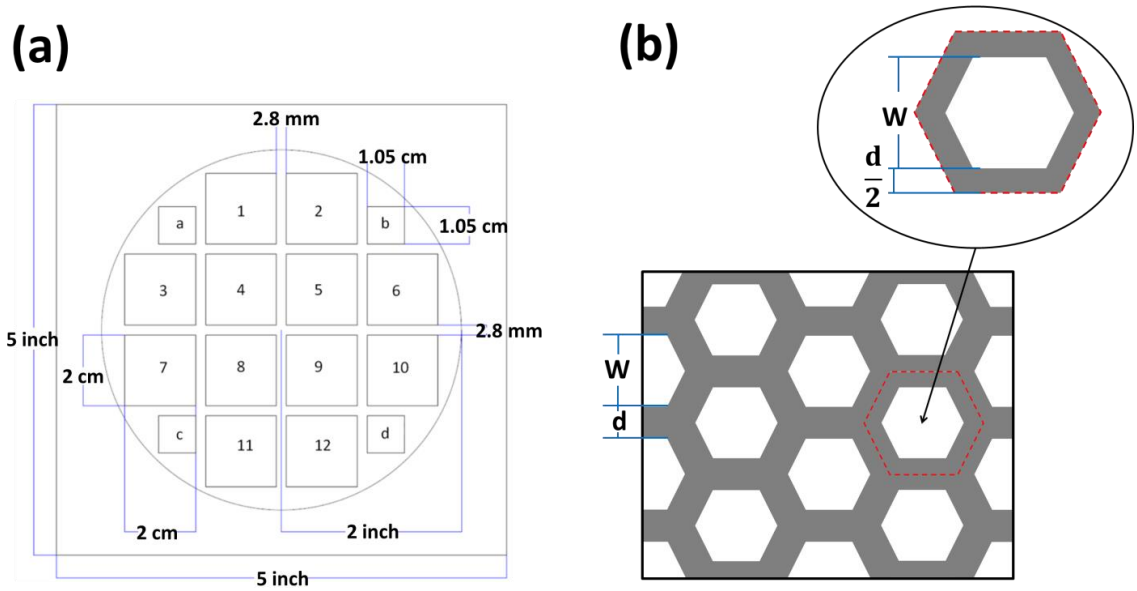

Figure 4-7 (a) Schematic representation of the mask; (b) sketch of the general structure motive. The depressed area on the final PDMS sample (pits) is in white and the gray area stands for the protruding part (walls). The size of honeycomb pits (W, the inner width of hexagons) differs from region to region with the spacing (d, the thickness of the walls) between every two microstructures remaining constant. The calculation of Wenzel roughness is based on the extracted unit (the hexagon highlighted with the red dash line).

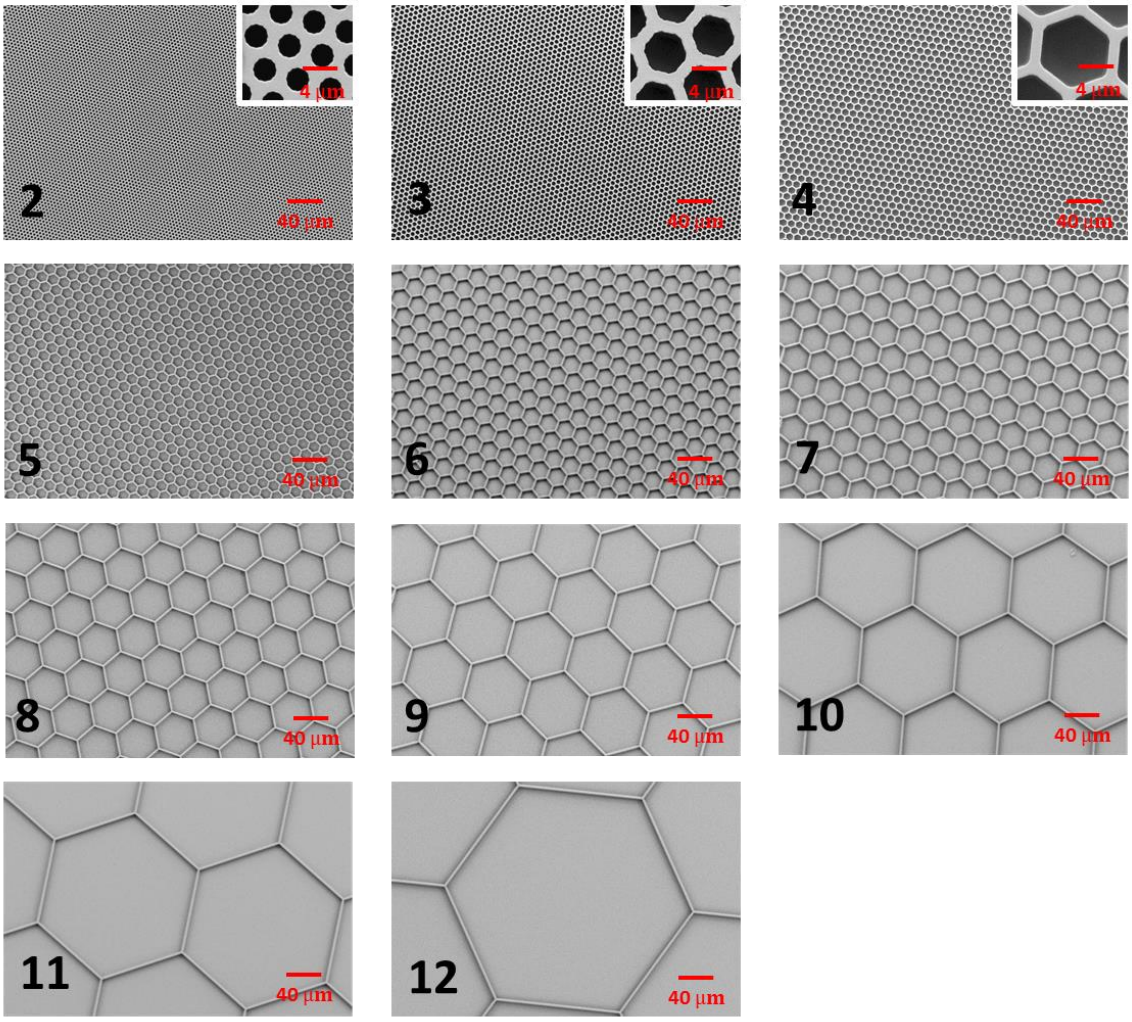

Figure 4-8 SEM images of discrete honeycombs on PDMS (images 2-12 correspond to the regions 2-12 illustrated in Table 1.).

On the basis of the surface design, the chromium mask was fabricated on quartz by Photronics MZD GmbH, Germany. Subsequent UV photolithography using the chromium mask as the mold produced SU8 negative photoresist patterns on a silicon wafer (IMT, KIT, Germany). As described in Section 3.1.2, the photoresist mold was fluorinated to minimize the adhesion of the casted PDMS. To facilitate the casting to protect the mold, the wafer was cut into individual square pieces corresponding to the regions specified in Figure 4-7a and Table 4-1. The microstructures on these smaller molds were then transferred onto PDMS substrates via soft casting (Section 3.1.2).

The topography of the successfully molded PDMS samples was analyzed under SEM (Figure 4-8). The microstructures appeared as pits of different diameters. Highly ordered circular pits were found on the smallest sized sample (region 2, **W**=3 µm). With

the increasing size of the microstructures (region 3-12), the edge of the hexagons became sharper. We observed hexagonal walls of the similar thickness on all surfaces. Set by the resolution limit of UV light during the fabrication of the photoresist mold, the size of the hexagonal pits on all the final samples was slightly smaller than that we expected from the design (ca. 0.5 µm smaller). The height of the features was determined to be ca. 1.3 µm on all samples.

Table 4-1 Feature size, feature spacing and Wenzel roughness of hexagonal microstructures on the final casted PDMS samples replicated from different regions of the mold.

Region	W / µm	d / µm	r_{Wenzel}
Smooth	-	-	1
2	3	1	1.98
3	5	1	1.72
4	8	1	1.51
5	12	1	1.37
6	20	1	1.24
7	30	1	1.16
8	45	1	1.11
9	70	1	1.07
10	110	1	1.05
11	170	1	1.03
12	250	1	1.02

It should be noted that this set of honeycomb microstructures resembled a series of varying Wenzel roughness (the ratio between the actual surface area and the geometric surface area) on the final casted samples. To calculate the Wenzel roughness factor (equation 5), we took the unit highlighted in Figure 4-7b.

$$\mathbf{r}_{\mathrm{Wenzel}} = \frac{S_{\mathrm{actual}}}{S_{\mathrm{geometric}}} = \frac{S_{\mathrm{geometric}} + S_{\mathrm{wall}}}{S_{\mathrm{geometric}}}$$

$$= \frac{\frac{\sqrt{3}}{2}(\mathbf{W}+\mathbf{d})^2 + 2\sqrt{3}\mathbf{Wh}}{\frac{\sqrt{3}}{2}(\mathbf{W}+\mathbf{d})^2} = \frac{(\mathbf{W}+\mathbf{d})^2 + 4\mathbf{Wh}}{(\mathbf{W}+\mathbf{d})^2} \qquad (5)$$

As shown in Table 4-1, the Wenzel roughness decreased with the increasing size of the hexagonal microstructures. This could be attributed to the reduction in the amount of wall area per unit projected area as the feature size increased and the feature spacing remained unchanged.

4.2.2 Size-dependent settlement of different fouling organisms

In the following discussion, the size of the microstructures refers to the designed size. The actual hexagonal pit size on the final PDMS samples was ca. 0.5 µm smaller than the designed size **W** illustrated in Table 4-1. Due to the high diversity in size preference of fouling organisms during their exploration and selection of habitats, topographies of different feature sizes were included for the settlement assays with different fouling species. Following a preincubation in artificial seawater (ASW, Tropic Marin®) for 1 h to ensure the full wetting of the microstructured surfaces, samples with hexagonal pits of 3 µm, 5 µm, 8 µm, 12 µm, 20 µm and the smooth PDMS were applied to examine the responses of zoospores of *Ulva linza* (Section 3.3.1) and cells of the diatom *Navicula incerta* (Section 3.3.2). To investigate the settlement behaviors of the cyprids of *Balanus improvisus*, hexagonal patterns of 3 µm, 5 µm, 8 µm, 20 µm, 30 µm, 45 µm, 110 µm, 170 µm, 250 µm and the smooth PDMS were prepared for the test via the droplet method (Section 3.3.3).

Attachment of cells of the diatom Navicular incerta

As shown in Figure 4-9, relatively smaller amount of attached diatoms were found on structured surfaces compared with the smooth PDMS. The dimension of cells of *Navicula incerta* is approx. 13 µm×4 µm. A diatom cell could not fit itself entirely inside an individual honeycomb pit on most of the patterned samples (images A-D in Figure 4-10) except the one with the largest honeycomb size of 20 µm (image F in Figure 4-10). When the microstructures (3 µm, 5 µm, 8 µm and 12 µm) were smaller than the diatom cells, the available attachment points decreased with the increasing hexagonal size, and therefore, the attachment density went down. Although diatoms could possible fit completely inside the hexagonal pits of ca. 20 µm and attain multiple attachment points, the lowest attachment was found on the largest dilatometer hexagons (20 µm). The settlement results suggested that a big proportion of diatoms were 'hanging' across hexagonal microstructures (image E in Figure 4-10). The attachment data of diatoms were well in line with the 'attachment point theory' [19, 73].

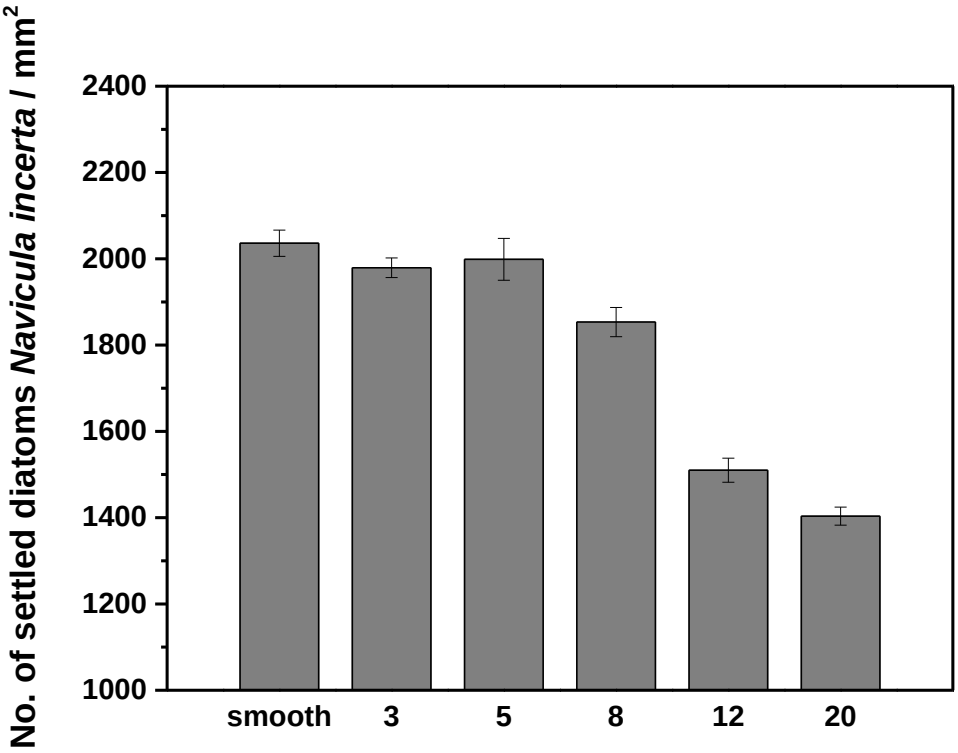

Figure 4-9 The density of attached *N. incerta* cells on different honeycomb patterns after washing, i.e., initial attachment density. Each value is the mean from 90 counts on 3 replicate slides. Bars show standard errors.

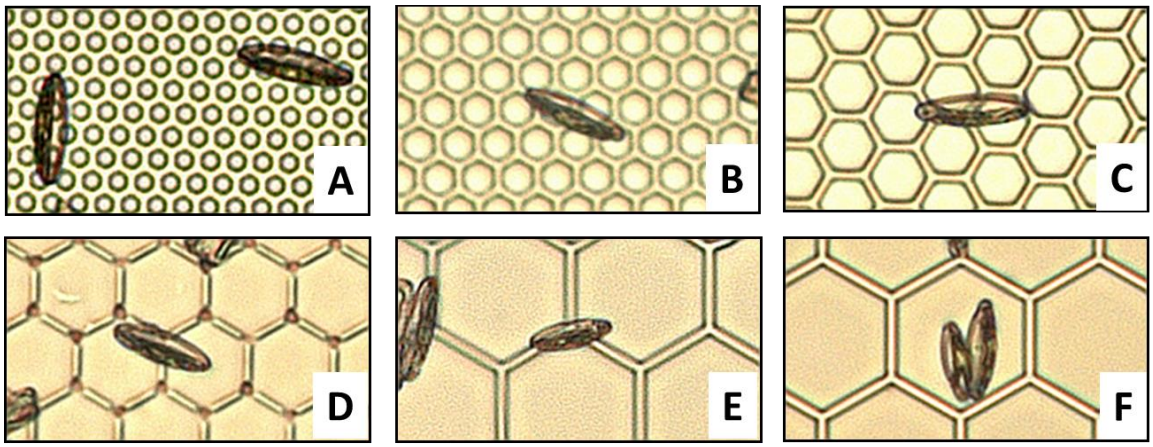

Figure 4-10 Microscopic images of diatoms attached on discrete honeycombs after washing (images A-D correspond to honeycombs of 3 µm, 5 µm, 8 µm and 12 µm, and images E and F are the honeycombs of 20 µm.).

Settlement of spores of Ulva linza

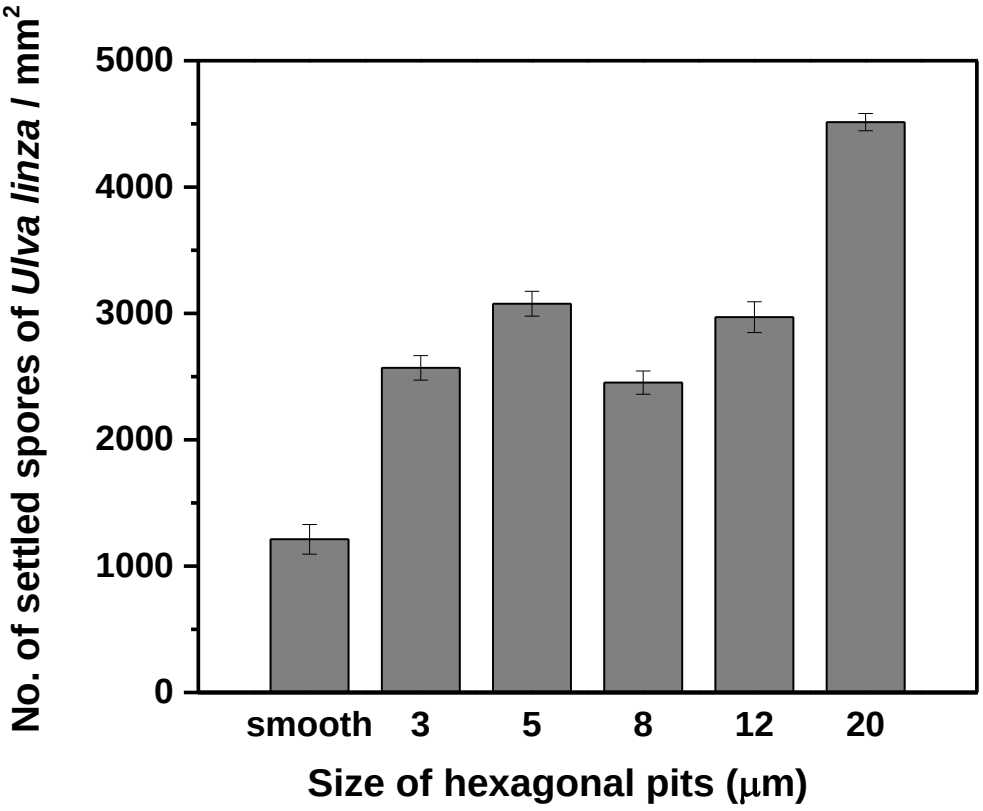

Figure 4-11 The density of attached spores of *Ulva linza* on the honeycomb patterns after 30 min settlement. Each point is the mean of 90 counts from 3 replicate slides with the bars showing standard errors.

As spores and diatoms differed highly in their physical morphology and attachment mechanisms, the settlement patterns of these two species were expected to be different from each other. A 45 min assay indicated very dense settlement of spores on all surfaces including the smooth control. Hence, the present data (Figure 4-11) were collected after 30 min incubation in spore suspension (Section 3.3.1). The amount of settled spores was substantially higher on all structured surfaces than the smooth control, which was in line with the observation of spore settlement on the honeycomb gradients (Section 4.1.2) but contrary to the diatom attachment in this study. The highest settlement was found on the microstructures with the largest feature size (20 μm). There was little difference in settlement density between the 3 μm, 5 μm, 8 μm and 12 μm diameter hexagons. This contrasted with previous findings on the gradient surface (Section 4.1.2), as over the range from 1 μm to 10 μm of the gradient, we found a visible increase in settlement density as hexagon size increased. The reasons for this difference probably lay

in the pattern layouts which were different in these two studies. Across the honeycomb gradient the feature spacing changed simultaneously with the feature size and the distance between the centers of adjacent honeycombs remained constant, while on these discrete honeycombs the feature spacing stayed the same (ca. 1 µm) and only the feature size differed from each other. As a consequence, contrary to the positive correlation found on the honeycomb gradient, the Wenzel roughness factors of these discrete honeycombs were inversely related to the hexagonal size. The influence on spore behaviors would therefore be different.

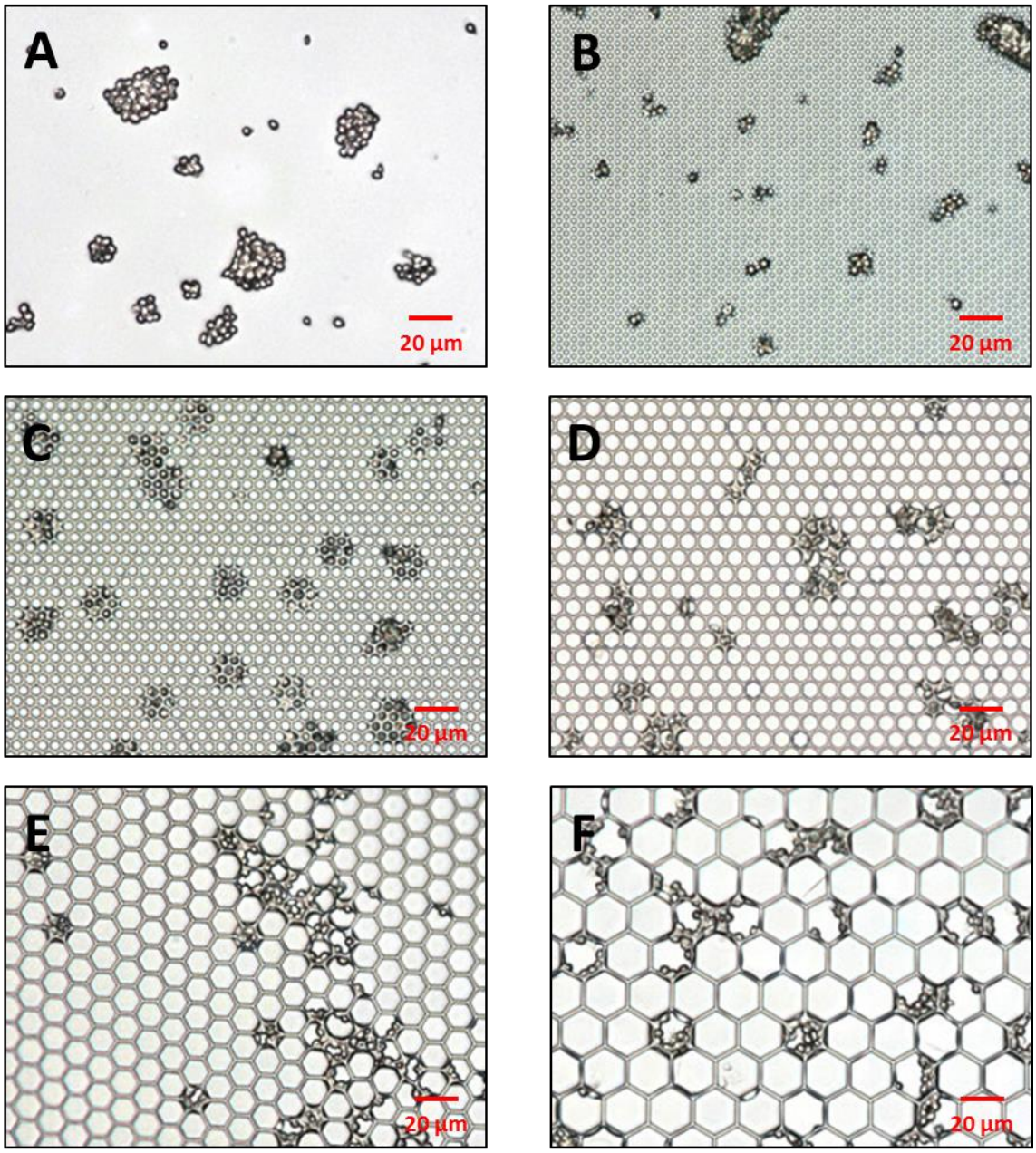

Figure 4-12 Microscopic images of spores settled on discrete honeycombs (image A is the smooth PDMS and images B-F correspond to honeycombs of 3 µm, 5 µm, 8 µm, 12 µm and 20 µm.).

Additionally, microscopic images of spore settlement (Figure 4-12) showed that although the honeycomb patterns did not affect the settlement density over the range of 3-12 µm, they did influence spore distribution. Spores settled in groups on the smooth PDMS, a distribution typically seen on PDMS-based coatings [32]. On the smallest sized pattern (designed size: 3 µm; real size: ca. 2.5 µm), spores were unable to fit inside the hexagons and sat on top of the features, which was expected as the smallest size for spores to squeeze in was around 2.6 µm (Section 4.1). Consequently, although the 3 µm microstructures had the highest Wenzel roughness, the settlement was unfavorable as the pits were too small for spores to get in and attach properly. On the 5 µm pattern, single spores were able to fit neatly inside the hexagonal features and many small aggregations of spores separated by thin walls could be found. These were often composed of 7 spores and formed a nearly hexagonally close packed pattern. On the 8 µm pattern, each hexagonal unit housed up to 3 spores and adjacent hexagons were often entirely filled, forming areas of dense clumping on the surface. While up to 7 spores were able to fit into the 12 µm hexagons, which again formed larger clumps of full or half full units. Spores tended to settle in groups on 8 µm and 12 µm discrete honeycombs on PDMS in this study. On the contrary, clumps of settled spores were rarely found in hexagonal pits of similar sizes (8 µm-10 µm) on the PMMA honeycomb gradient in our previous study.

On the one hand, the physicochemical nature of the PDMS substrate contributed to the formation of spore clumps during settlement [95] which was validated by the observation on the smooth PDMS in this study. On the other hand, considering the size of motile spores (4-5 µm at the widest part of the body), the elastic nature of PDMS material enhanced the possibility to host a larger number of spores inside a single pit. This explained the similar level of settlement density on 8 µm and 12 µm discrete honeycombs to the 5 µm samples, although they had relatively smaller Wenzel roughness. On the largest pattern (20 µm), clumps of spores were again present, but the hexagons were rarely full. Among all the structured surfaces we tested with spores, the 20 µm sample had the smallest area occupied by the wall and the lowest Wenzel roughness. From that point of view, it was most similar to the smooth control. However, we actually got the highest density of settled spores on this surface. Spores could be seen settled at the ‘kinks’ in the hexagonal pits which were normally preferred by spores. The settlement of a spore could induce the attachment of other spores as a consequence of both topographic signals [32] and chemical signals produced by settled spores, i.e., settled spore released

compounds that attracted swimming spores. Moreover, 20 µm pits provided enough depressed area to host relatively bigger clumps of settled spores. Therefore, microstructures of 20 µm achieved the maximum settlement in this topographic group.

Settlement of cyprids of Balanus improvisus

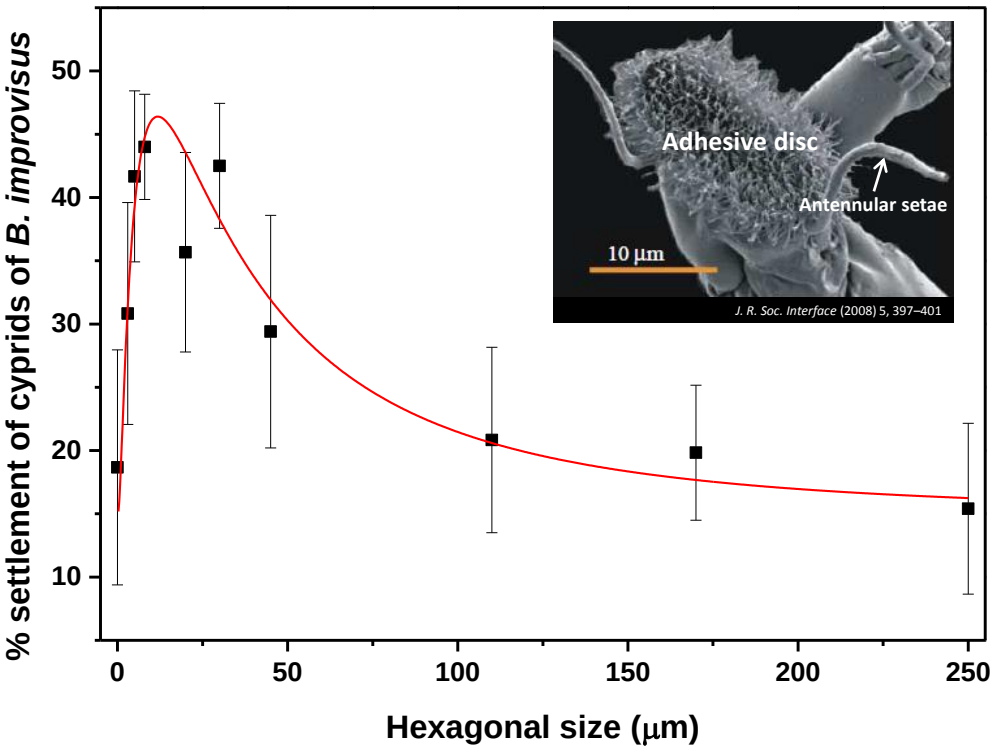

Figure 4-13 Percentage settlement of cyprids of *Balanus improvisus* on different surfaces after 48 h. Reported values are the means of the data collected from 6 replicates with error bars showing the standard errors. The line is intended to guide the eye. The attached SEM image was taken from Phang et al. 2008 [115].

A clear trend in the settlement of *Balanus improvisus* cyprids was observed in relation to the size of honeycomb pits (Figure 4-13). Within the smaller size range from the smooth to 5 µm, the settlement went up with the size of the hexagonal microstructures. The highest percentage of settlement was found on the microstructures with the pit sizes of 5-30 µm. Besides the highest Wenzel roughness obtained in this size region, these microtextures were below or similar to the scale of the adhesive discs of cyprids (ca. 25 µm in diameter) and they would probably not physically interfere with adhesion. Moreover, regarding the fact that on the adhesive disc there were a large number of antennular setae (ca. 0.5-2 µm in diameter and ca. 10-30 µm in length) which actively functioned as hydrodynamic and chemo-receptors [116], not to mention there were some

even smaller sensory structures, it was possible that these sensory organs might perceive information on surface texture below the scale of the antennular disc and probably improved adhesion. The further increasing of the feature size (> 30 μm) and decreasing of Wenzel roughness (< 1.16) decreased the settlement of cyprids. This could be interpreted by the interaction between the microstructures and the adhesive structures of the cyprids — the antennular discs. As indicated in the work of Berntsson et al. [17], microtextures above the dimension of the adhesive disc could interfere with the exploration behaviors of cyprids and thus prevent stable temporary attachment. That study also showed that the recruitment of *B. improvisus* on the field-exposed panels was almost absent when the surface topography had a roughness width within 150-200 μm. In the present work, as the size of the honeycomb pits increased further up to 250 μm, the amount of settled cyprids was reduced to a level comparable to the smooth PDMS control. Cyprids are ca. 530-580 μm in length and ca. 250-270 μm in width [42]. They did not prefer microstructures of the feature sizes that fell into the range of ca. 100-300 μm, because they could not fit their bodies in the microstructures entirely. Additionally, these microstructures were also too large to confer any adhesive advantage during temporary attachment as the features above 100 μm were essentially flat for the adhesive disc, which could also be predicted by comparing the Wenzel roughness values (e.g., smooth vs. 250 μm: 1 vs. 1.02). To some extent the general settlement trend on the structured surfaces was consistent with the literature. However, in contrast to the literature [17], settlement was relatively higher on patterned surfaces than the smooth, which could possibly be attributed to the low feature heights (ca. 1.3 μm compared with 20-100 μm in the literature) used in this study.

4.2.3 Conclusions

A series of discrete honeycomb samples, varied in the feature size, were prepared via PDMS casting. On each sample contiguous hexagonal pits of a specific size were separated by a thin PDMS wall with the fixed thickness for the whole series.

The attachment density of diatoms decreased with the increasing microstructure size, as there were fewer attachment points available for each diatom when the feature dimension increased. This was consistent with the ‘attachment point theory’. When the microstructure grew large enough to fit in the whole diatom, the attachment density was also correlated with the positioning of the attached diatoms.

Spore settlement assays showed that all honeycomb patterns stimulated spore settlement. The highest settlement density was on the largest sized features (20 µm). Different from previous gradient study, no obvious differences had been found in the amount of settled spores between microstructures of 3 µm, 5 µm, 8 µm and 12 µm. This was primarily related to the different pattern layouts applied in these two studies, resulting in inverse correlations between the microstructure size and the Wenzel roughness. Additional explanation was provided by the different physicochemical and mechanical properties of the base materials (PDMS in discrete honeycomb study vs. PMMA in honeycomb gradient study). As PDMS substrates induced the aggregation of spores and facilitated the formation of clumps, which therefore led to the deviation from the guideline of Wenzel roughness.

Settlement of cyprids went up with the size of honeycomb microstructures (0-5 µm), reached a maximum on the features below or similar to the scale of the adhesive disc (ca. 25 µm), and eventually decreased to a level similar to the smooth control with the further increasing of the microstructure size. Compared with diatoms and spores, the sensory system of cyprids composed of a series of multilevel receptors, which were highly diverse in size and function [116]. Responses of cyprids on these discrete honeycombs could be associated with both the Wenzel roughness and the scale and function of the adhesive disc and the antennular setae.

To conclude, topographies of varying feature sizes affected the attachment of different fouling species in different manners. Generally, the attachment of the diatom *Navicula incerta* was dominated by the density of available attachment points, while the settlement of both *Ulva* spores and *Balanus improvisus* cyprids could be correlated with the Wenzel roughness factor of the structured surfaces. In addition, the gregarious settlement on PDMS substrates played an important role in the spore attachment density, and the settlement of cyprids was also influenced by the interaction of sensory and adhesive structures with topographic features of comparable sizes.

4.3 Tapered microstructures for the minimization of attachment area

As described in Section 4.2, we observed different responses of fouling organisms(spores of *Ulva linza*, the diatom *Navicula incerta* and cyprids of *Balanus improvisus*) to the same set of topographies. The question, whether the species-specific preference correlates with different topographic cues which dominate the attachment of different fouling organisms, remains to be further confirmed. To commence an additional comparasion of the topographic cues which guide the settlement of different fouling species, a series of tapered microstructures were fabricated and investigated towards their influence on the attachment of *Ulva* spores and the diatom *Navicula*.

Sufficient contact at the cell-substrate interface could be commonly found on surface patterns favored by fouling organisms, as it is critical and essential for marine colonizers to attain solid adhesion against external hydrodynamic forces. As indicated in reported studies [70], sites between the floor and the vertical wall were preferentially occupied by *Ulva* spores in settlement assays. Here cone-like tapered microstructures were designed to first avoid these unfavorable corners and meanwhile possess limited available contact area on the outmost surface. In our previous discrete honeycomb study (Section 4.2), spores and diatoms were examined towards their responses on topographies with a broad size range which covered their body sizes. Different from that, tapered microstructures were designed to have depressed regions smaller than the dimensions of both spores and diatoms, as it was implied in the literature [16, 19, 32] that it was more likely to reduce the attachment of fouling organisms on narrow topographies.

To construct such tapered microstructures of different feature periods and feature heights, hot embossing and hot pulling techniques were employed. Settlement of the diatom *Navicula incerta* and zoospores of *Ulva linza* were then performed on these microstructures to explore the topographic cues which guided the attachment of these two species.

4.3.1 Design and characterization of tapered microstructures

Tapered microstures of different feature periods (3 µm, 2 µm, 230 nm) and feature heights were prepared via hot embossing and hot pulling (Setion 3.1.1). Subsequent

characterization with SEM and AFM provided the topographic information of samples in detail and water contact angle analysis compared the wetability between surfaces of different topographies.

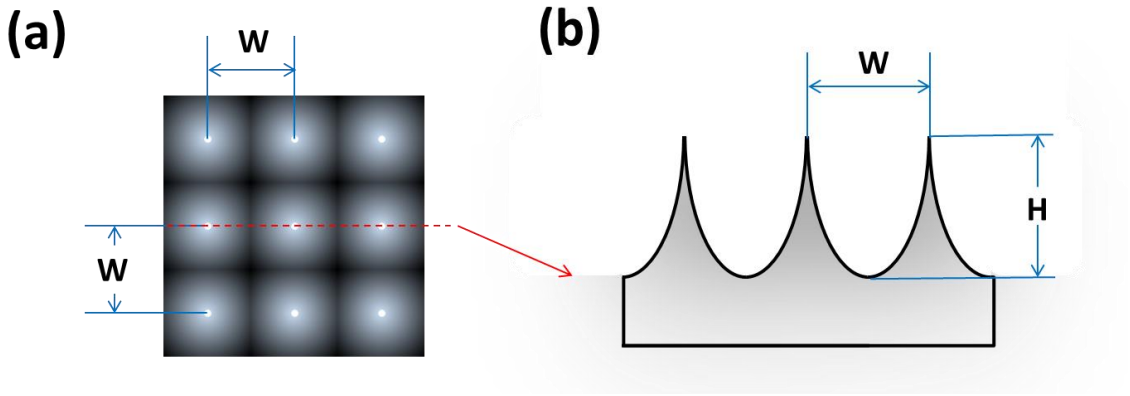

Figure 4-14 Schematic diagrams of tapered microstructures: (a) top view; (b) cross-sectional view.

The total dimensions of the sample were 2×2 cm^2. Tapered microstructures were patterned in a square array (Figure 4-14a). In the cross-sectional view (Figure 4-14b) taken along the side of the square array (indicated with the red dash line in Figure 4-14a), the feature period (**W**) and the feature height (**H**) were defined as the distance between the tips of two adjacent microstructures and the fall between the tips and the valleys, respectively.

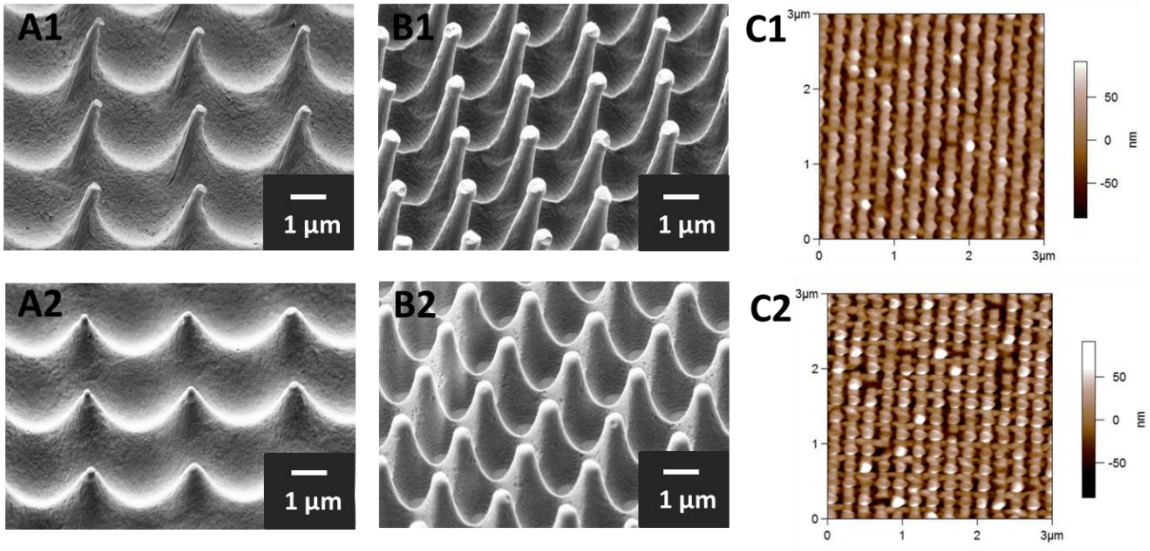

Figure 4-15 SEM and AFM images of tapered microstructures of different feature periods (**W**) and feature heights (**H**). 45 degree SEM images (A1, A2: **W**=3 µm; B1, B2: **W**=2 µm); AFM images (C1, C2: **W**=230 nm).

Uniform tapered microstructures (Figure 4-15) were molded in an isotropic area on polycarbonate (PC) sheets as described in Section 3.1.1. In brief, hot-embossed microstructures (e.g., 3µm-L) were produced by softening the PC foil above its glass transition temperature, pressing the mold into the molten polymer with controlled embossing temperature and pressure, and demolding after cooling the whole setup down to ca. 50 °C. To fabricate the hot-pulled samples (e.g., 3µm-H) for this study, a two-step hot pulling technique was employed. First, the PC foil was firmly adhered on the rough demolding plate via embossing with a smooth mold. Compared with the standard hot embossing procedure, the second step of hot pulling was featured by increasing only the temperature of the molding plate to soften the polymer before embossing, and an additional pulling action before cooling down and demolding. With the cone-like embossed microstructures, the available area on the horizontal plane decreased with the increasing feature height, which eventually ended up with sharp tips. Such topographic architectures strongly reduced the terminating surface area available for attachment of fouling organisms. As any corners were avoided by the smooth, curved pits, the adhesion of fouling organisms on such topographies was expected to be unfavorable. The corresponding properties of displayed topographies (Figure 4-15) are listed in Table 4-2.

Table 4-2 Surfaces properties of tapered microstructures (feature period, feature height, Wenzel roughness factor, and static water contact angle).

Name	**3µm-H**	**3µm-L**	**2µm-H**	**2µm-L**	**230nm-H**	**230nm-H**	**Smooth PC**
Corresponding image (Figure 4-15)	A1	A2	B1	B2	C1	C2	—
Feature period	*3 µm*	*3 µm*	*2 µm*	*2 µm*	*230 nm*	*230 nm*	—
Feature height	*2.57 µm*	*1.66 µm*	*2.78 µm*	*2.05 µm*	*170 nm*	*100 nm*	—
Wenzel roughness	*1.77*	*1.39*	*2.53*	*2.01*	*1.62*	*1.26*	*1*
Water contact angle / °	*119 ± 7*	*126 ± 5*	*118 ± 6*	*124 ± 5*	*121 ± 9*	*124 ± 8*	*98 ± 1*

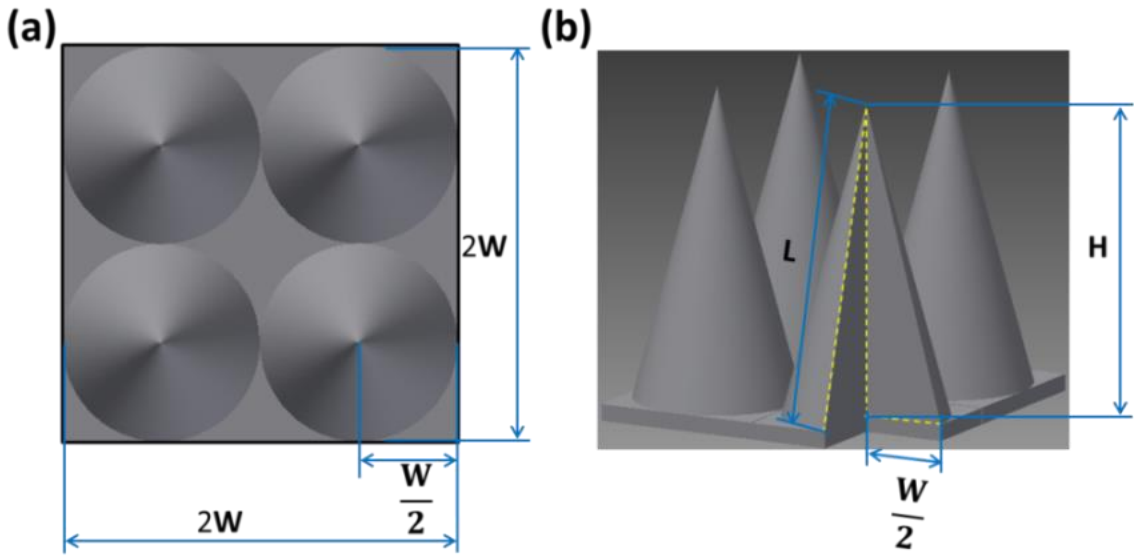

Figure 4-16 (a) Schematic representation of the repeating unit of tapered microstructures. The side of the square unit is 2**W** and the radius of the projected circle is **W**/2. (b) **L** stands for the slant height of the cone. The Wenzel roughness factor increases with the height of the structures **H** due to the increased side walls.

To calculate the Wenzel roughness of the surfaces, the structure was approximated using the shape of a cone. The height of tapered microstructures **H** was determined from SEM and AFM images. As illustrated in the extracted repeating unit for quantification (Figure 4-16a), 2**W** (2 times the feature period) was the side length of the square unit and $\frac{\mathbf{W}}{2}$ (half of the feature period) was the radius of the projected circle. In Figure 4-16b, **H** (the feature height) represented the height of the cone and **L** stood for the slant height of the cone. The Wenzel roughness factor was calculated from the ratio between the actual surface area and the geometric surface area (the projected surface area). By deducting the base surface area from the lateral surface area of the cone, we got to know the amount of increased surface area per cone due to the structuring. Therefore, for the extracted unit the actual surface area equaled the sum of the square area and the difference between the lateral area and the base area of the four cones. The projected surface area was the total area of the square. Hence, for tapered microstructures,

$$\mathbf{r}_{Wenzel} = \frac{\mathbf{S}_{actual}}{\mathbf{S}_{geometric}} = \frac{\mathbf{S}_{square}+4(\mathbf{S}_{lateral}-\mathbf{S}_{basal})}{\mathbf{S}_{square}} = \frac{2\mathbf{W}\times 2\mathbf{W}+4(\pi\times\frac{\mathbf{W}}{2}\times\mathbf{L}-\pi\times(\frac{\mathbf{W}}{2})^2)}{2\mathbf{W}\times 2\mathbf{W}}$$

$$= \frac{2\mathbf{W}\times 2\mathbf{W}+4(\pi\times\frac{\mathbf{W}}{2}\times\sqrt{(\frac{\mathbf{W}}{2})^2+\mathbf{H}^2}-\pi\times(\frac{\mathbf{W}}{2})^2)}{2\mathbf{W}\times 2\mathbf{W}} = 1-\frac{\pi}{4}+\frac{\pi}{4}\sqrt{1+4(\frac{\mathbf{H}}{\mathbf{W}})^2} \qquad (6)$$

As indicated in equation 6, Wenzel roughness factor of tapered microstructures is determined by both the feature period (**W**) and the feature height (**H**). $\mathbf{r}_{Wenzel}$ is positively correlated with **H** but negatively related to **W**. The $\mathbf{r}_{Wenzel}$ values of all selected topographies are reported in Table 4-2.

The static water contact angle of pristine PC was ca. 98°. We observed an increased hydrophobicity on all patterned surfaces. This general trend could be well explained by the Wenzel theory of wetting. However, no significant difference in wettability was found between surfaces with different microstructures.

4.3.2 Attachment of the diatom *Navicula incerta* and *Ulva linza* zoospores on tapered microstructures

Besides tapered microstructure series (3µm-H, 3µm-L, 2µm-H, 2µm-L, 230nm-H, 230nm-L, and smooth PC), cell culture plates (polystyrene, PS) and Nexterion glasses were also included as standards in spore and diatom settlement assays (Section 3.3.1 and Section 3.3.2). All samples were preincubated in filtered ASW (Tropic Marin®) with shaking for 1 h prior to the assays in order to remove any air that might be trapped between microstructures. 2 h settlement of diatoms *Navicula incerta* and 45 min settlement of spores of *Ulva linza* were carried out to investigate the effect of topographic cues on the settlement of these two species.

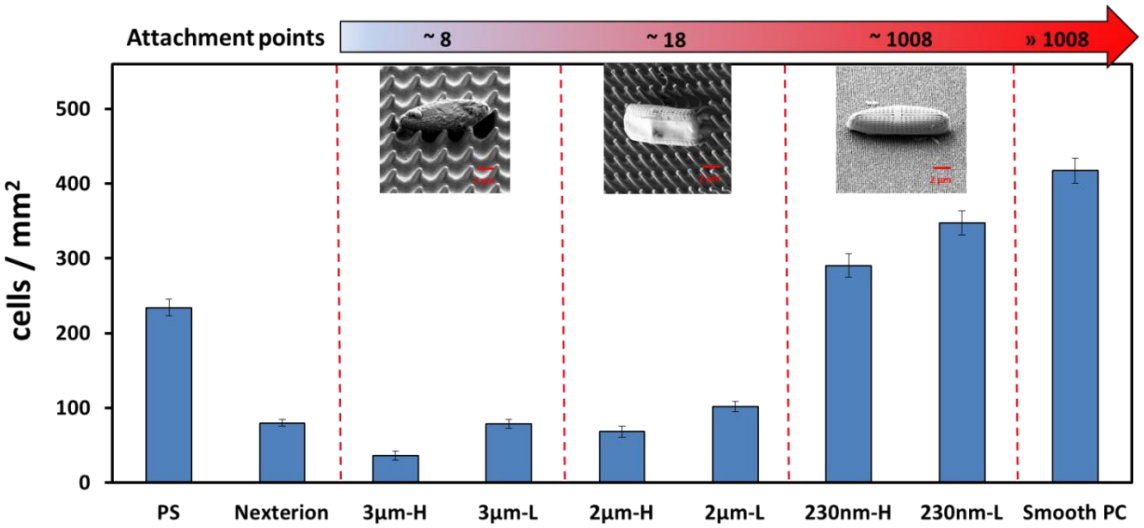

Figure 4-17 The density of settled diatoms *Navicula incerta* on different surfaces in a 2 h settlement assay. Reported data are the means of 80 counts with 20 counts collected from each of 4 replicates. Error bars represent standard errors. Reproducibility of the results has been confirmed in a repeating assay with another batch of diatoms.

Unlike *Ulva* spores, diatoms *Navicula* lack flagella and hence could not actively explore the surfaces before the initial contact with the surfaces. After being passively brought onto the surface by flow or gravity force, diatoms could either adhere to the surface or relocate themselves by 'gliding'. The amount of settled diatoms had no obvious correlation with Wenzel roughness. Previous researches [19, 73] suggested that the available attachment area was a key factor that should be taken into account for the settlement of diatoms. The numbers of attachment points illustrated in Figure 4-17 were estimated from the dimension of the diatom *Navicula incerta* (around 13 µm in length and 4 µm in width) and the size of the microstructures. The attachment of diatoms was reduced on structured surfaces compared with the smooth PC. Interestingly, the settlement data was highly in line with the number of attachment points (smooth PC > 230 nm > 2 µm > 3 µm). As the feature period increased, the number of attachment points for diatom adhesion decreased, or in other words, the available adhesion area was reduced, which consequentially led to poor adhesion and hence easier removal by disturbance (washing) . For instance, only ca. 10 attachment points were available for diatoms on topographies of 3 µm period, and therefore, the settlement was significantly lower compared with that on the smooth control (ANOVA, Tukey test, $p < 0.05$), which allowed for multiple attachment sites. Comparing the settlement of the diatom on topographies of the same feature period but different feature heights (3µm-H vs. 3µm-L; 2µm-H vs. 2µm-L; 230nm-H vs. 230nm-L), we noticed that slight decrease of settlement occurred with the increasing feature height. A higher degree of stretching/pulling resulted in higher microstructures with relatively sharper tips, in which case the available contact area was further reduced and so was the settlement.

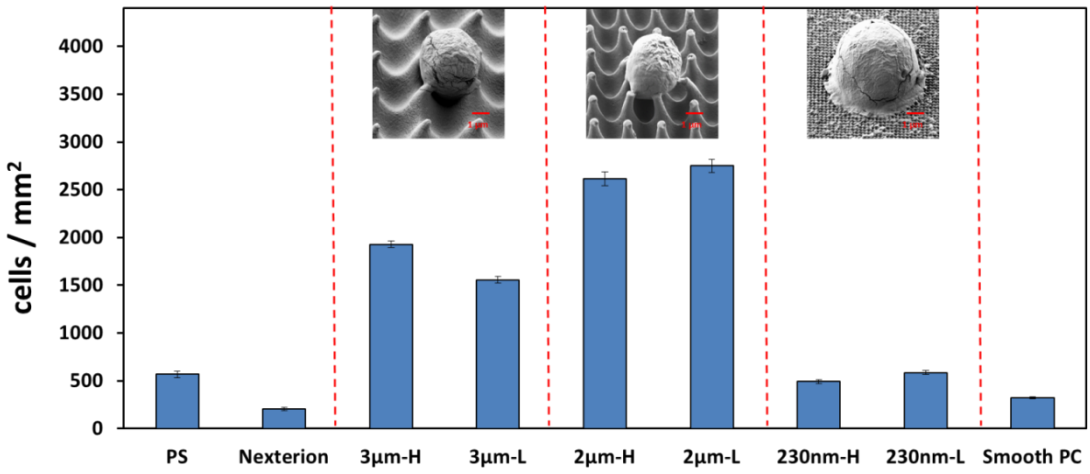

Figure 4-18 The density of zoospores of *Ulva linza* settled on different surfaces in a 45 min settlement assay. Reported data are the means of 90 counts with 30 counts collected from each of 3 replicates. Error bars represent standard errors. Reproducibility of the results has been validated in a repeating assay with a second batch of spores.

The settlement of *Ulva* spores takes place following an active exploration phase [33, 34]. After 45 min incubation in spore solution in darkness, more spores settled on PS than on Nexterion glass (Figure 4-18). This was consistent with the settlement preference of zoospores to hydrophobic surfaces as previously reported [54]. Contrary to diatom preference, spores settled at a higher density on structured surfaces than on the smooth polycarbonate. Although the differences in settlement between microstructures of the same feature period but different feature heights were not generally significant (ANOVA, Tukey test, $p > 0.05$), notably different settlement could be found on topographies of different feature periods (2 µm > 3 µm > 230 nm > smooth PC) (ANOVA, Tukey test, $p < 0.05$). In contrast to the attachment of diatoms, the settlement of spores correlated well with Wenzel roughness. The highest population of spores was measured on microstructures of 2 µm period, so was the largest Wenzel roughness factor. As previously discussed, Wenzel roughness ($\mathbf{r}_{Wenzel}$) of tapered microstructures increased with the feature height (**H**) but decreased with the feature period (**W**). The highest Wenzel roughness of 2 µm samples was the result of the common-effect of **H** and **W**. Although spores appeared to sit half inside the features, they achieved biological success to adhere on these surfaces with the highest Wenzel roughness. On the other side, despite the similarity in Wenzel roughness, the settlement on 3 µm structures was remarkably higher than on 230 nm structures (ANOVA, Tukey test, $p < 0.05$). The SEM image (Figure 4-18) showed that on tapered microstructures of 3 µm period the spore could fit

snugly into the pit generated by four adjacent ‘cones’. Under such a circumstance, spores attained highly enhanced contact area and assured solid adhesion against potential external hydrodynamic forces. Moreover, the response of spores might not be as sensitive as expected on features of submicron scales, which could be emphasized by the fact that the settlement on tapered microstructures of 230 nm was only slightly higher than the smooth PC considering their relatively big difference in Wenzel roughness. Therefore, besides the predominant influence of Wenzel roughness on spore settlement, the local binding geometry also played an important role.

4.3.3 Conclusions

Our study demonstrated different responses of *Ulva* spores and diatoms *Navicula* to the same set of tapered microstructures, which was consistent with the previous observation on discrete honeycombs (Section 4.2). This species-specific settlement preference could be attributed to different topographic cues that actually guided the attachment of these two organisms. The attachment of diatoms was mainly regulated by the ‘attachment point theory’, while the settlement of zoospores was co-dominated by the Wenzel roughness factor and the local binding geometry (available adhesion area), The possible correlation between the topographic cues to guide the settlement and the biological nature of fouling organisms needs to be further analyzed with additional topographies and more fouling species.

4.4 Microtexture-based SLIPS as antifouling coatings

Previous studies (sections 4.1-4.3) focused on the direct influence of surface topographies on the settlement of marine fouling organisms. It turned out that fouling responses were complicated on sole topographies, e.g., there was no a common driving factor for the attachment of different fouling species. As it is most likely that successful novel non-biocidal coatings need to be multifunctional (i.e., incorporate a range of attributes such as topography, surface energy, modulus and lubricity) [24, 117], in this study the concept of slippery liquid-infused porous surfaces (SLIPS), which were constructed by combining the surface lubricity on the basis of microporous topographies, was tested towards its potential in marine antifouling applications.

Liquid-repellency of surfaces has been shown to contribute to antifouling properties of natural or manufactured surfaces, e.g., 'Lotus-Effect' [13]. However, liquid-repellent antifouling surfaces relying solely on complex micro- and nanoscopic architectures were limited for practice because of both the intricate and expensive fabrication and the indifferent performance in harsh and diverse environment. A novel route to liquid-repellency was inspired by the 'aquaplaning' of prey on the peristome of pitcher leaves, which could be realized by using porous microtextures as the intermediate layer to lock in a lubricating film, thus generating fluidity and slipperiness on solid substrates [118, 119]. To obtain SLIPS [120], a microporous substrate was required and the surface energies of the solid and the lubricant needed to be well-matched. It was reported [121] that the anti-biofilm performance of SLIPS was comparable to that of PEGylated surfaces.

In this section, porous poly(butyl methacrylate-co-ethylene dimethacrylate) (BMA-EDMA or BE) microstructures prepared via UV-initiated polymerization [94] was covalently bonded on glass substrates. Subsequent infusion of fluorocarbon lubricants into the polymer microtexture produced a series of slippery surfaces. The antifouling performance of these SLIPS was tested against the settlement of both *Ulva* zoospores and *Balanus amphitrite* cyprids, which respectively represent the typical colonization of soft-fouling and hard-fouling species. The investigation of the fouling-release capability of SLIPS was completed with the removal of sporelings of *Ulva linza*. Additionally, SLIPS surfaces were immersed in the ocean to check their antifouling performance in the field.

4.4.1 Surface characterization

As described in Section 3.1.3, in collaboration with the group of Dr. Pavel Levkin at ITG, KIT, thin porous poly(butyl methacrylate-*co*-ethylene dimethacrylate) (BE) films were synthesized on glasses via UV-initiated radical polymerization and used as the substrates to prepare the slippery surfaces. By infusing three different fluorocarbon lubricants (Krytox® GPL 103, Krytox® GPL 100 and Fluorinert® FC-70) into the microtextured polymer substrates, the water-repellent slippery surfaces were produced. In the previous work by Aizenberg et al. [120], the SLIPS surfaces were prepared by infusing a lubricant liquid into a porous perfluorinated membrane (Teflon) or into a surface with epoxide resin based nanoarray produced by moulding and subsequently functionalized with heptadecafluoro-1,1,2,2-tetrahydrodecyltrichlorosilane. In comparison, our SLIPS surfaces were based on the non-fluorinated polymethacrylate with the microporous structure. The polymer substrate was produced in-situ by UV-initiated polymerization. Compared with normal moulding this method could be applied to coat relatively larger area. And by controlling the composition of the polymerization mixture, it was possible to control the pore size, the thickness of the polymer layer as well as the surface functionality making this substrate a convenient material for systematic investigation of SLIPS properties.

In the following, BE represents the pristine porous BMA-EDMA, and BE103, BE100 and BE70 are porous BMA-EDMA surfaces infused with fluorocarbon liquids Krytox103, Krytox100 and Fluorinert FC-70, respectively. Nexterion® Glass B microscope slides (Schott, Germany), Teflon sheets (polytetrafluoroethene, PTFE; 125 µm; American Durafilm Co, USA), PEG2000 self-assembly monolayers on gold, and PDMS-coated glass slides (SILASTIC® T-2) were included as standard surfaces for biological tests.

The morphology of the porous BE polymer coating without any fluorocarbon liquid represented a homogeneous and interconnected network of polymer globules (Figure 4-19a and Figure 4-19b) with the average globule size determined from SEM images being 1.14±0.17 µm [122]. The thickness of the porous BE polymer was ~45 µm measured from the cross-sectional SEM image (Figure 4-19b) and the size of the pores and polymer globules across the polymer thickness was similar. The porosity based on the amount of porogens present in the polymerization mixture was ~50%. Such microtextured

hydrophobic substrates with large surface area could effectively assist the infusion and stabilization of the hydrophobic lubricants applied in the study. As verified by X-Ray tomography in the reported article [123], the Krytox lubricant liquids could be easily infused into the pores of BE surfaces completely and formed a stable thin lubricant liquid layer on top of the surface.

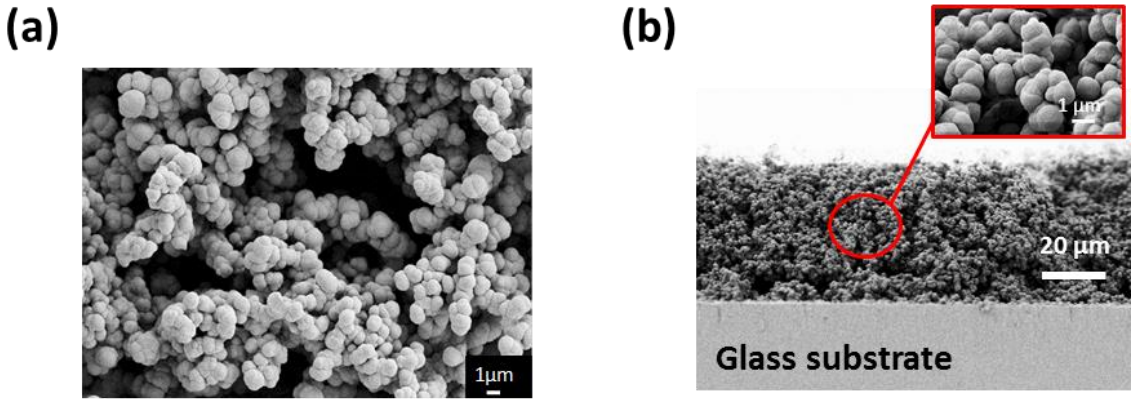

Figure 4-19 SEM images of the microporous BMA-EDMA polymer. (a) Top view; (b) cross-sectional view.

The stability of antifouling coatings in seawater is essential to the surface design if intended for long timescale practical applications. In Figure 4-20, to determine the stability of slippery surfaces in the laboratory settlement and growing assays, the evolution of surface wettability of BE103, BE100, BE70 and BE with respect to the length of incubation time in moving filtered artificial seawater and filtered seawater was tracked with water contact angle (WCA) measurements (Section 3.4.2). The WCA obtained on pristine BE decreased gradually with time, indicating degradation of the surface caused either by adsorption of components from the solution or by the slow hydrolysis of the ester bonds on the surface, leading to increased hydrophilicity. On the other hand, the WCAs measured on the BE103 and BE100 slippery surfaces (Krytox103 and Krytox100 infused BE, respectively) remained nearly constant at least up to 7 days of incubation in both artificial seawater and seawater. The pristine BE70 surface had a WCA of ~114° and very low water contact angle hysteresis (~6°). According to Figure 4-20, after 2 days of incubation, the static WCA of the BE70 surface increased slightly while the WCA hysteresis increased significantly. Considering the slight increase in static WCA of BE70 within 2 days of immersion, the possible explanation for this change was that the lubricant layer had been partially removed from the surface making the surface more rough and, therefore, leading to the increase of the static WCA and larger WCA hysteresis, which was similar to the properties of the BE surface. The further decrease of

the static and advancing WCAs could be explained by the change of the surface chemistry of the BMA-EDMA porous surface caused by hydrolysis of the ester bonds in slightly alkaline environment (pH ~8.2). This behavior was obvious from the decrease of WCA on the non-infused BE polymer surface exposed to the solution.

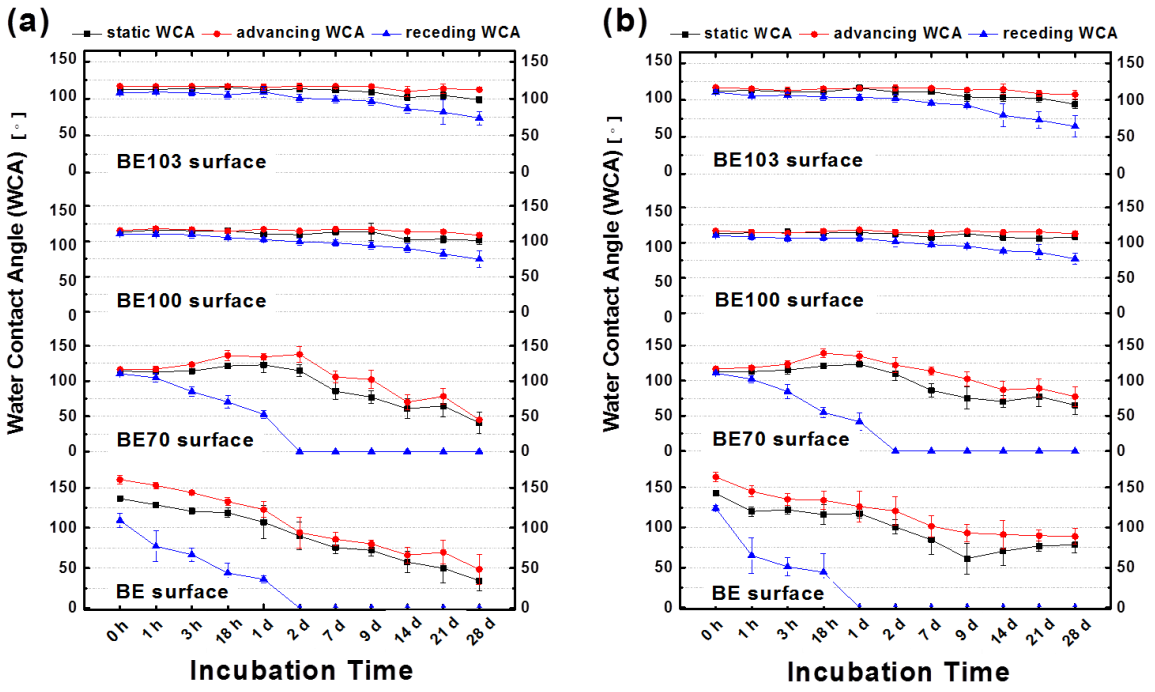

Figure 4-20 Water contact angles of BE, BE70, BE100 and BE103 surfaces as a function of the incubation time in both filtered (a) artificial seawater and (b) seawater. The reported values are the means of 9 measurements collected from 3 replicates with the error bars representing the standard deviations.

4.4.2 Toxicity test

As described in Section 3.4.3, to test whether toxic compounds were leached from the coatings which might affect the settlement, viability and growth of zoospores, leachates of the BE-based SLIPS were collected after 48 h immersion in ASW. The biomass of sporelings that developed in the leachates was quantified. The RFU values in Figure 4-21 for the various leachates, including from the standard surfaces, were statistically indistinguishable (ANOVA, Tukey test, $p > 0.05$). The similarity in the relative number of live sporelings found in all media including the ASW control demonstrated that the germination and growth of spores was not affected by fluorocarbons in the leachates of the BE based SLIPS. Similar results were obtained from two separate tests with different batches of spores.

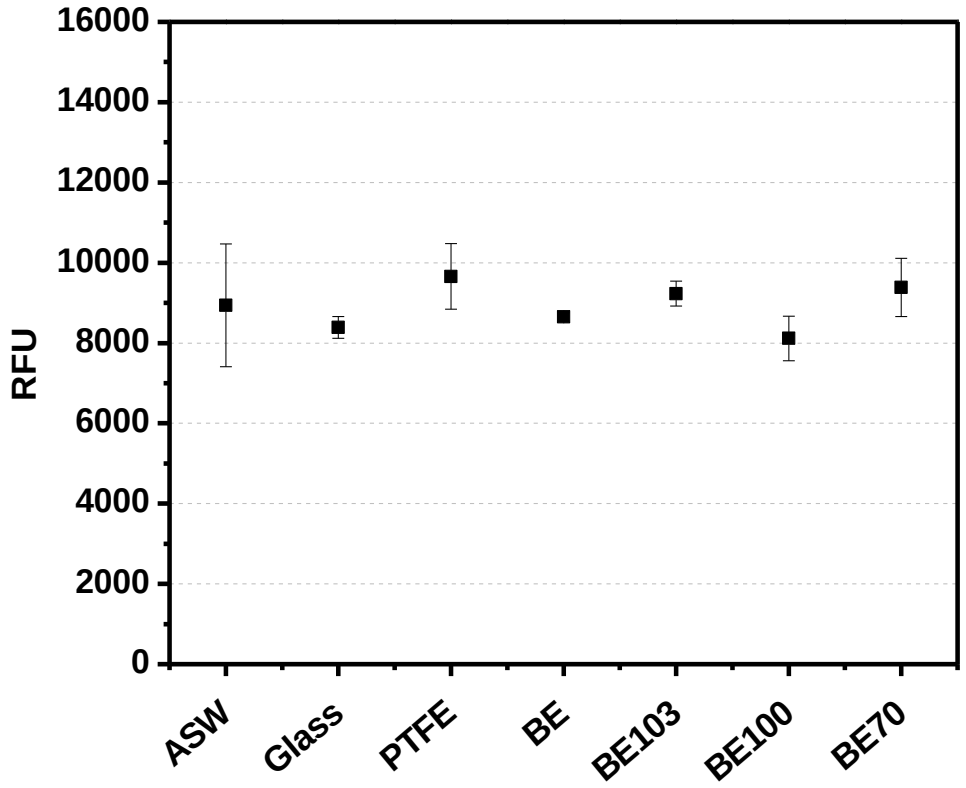

Figure 4-21 The relative fluorescence intensity (RFU, relative fluorescence units) of sporelings cultured in leachates collected from different samples after 48 h of incubation in ASW. Values are the means of 12 readings, 4 from each of 3 replicates with the error bars showing the standard errors.

4.4.3 Laboratory settlement and removal tests

To study the response of spores to the different surfaces, after 2-day preincubation of all samples except PEG2000 self-assembly monolayers (SAMs) in ASW, settlement assays were carried out in the laboratory for 45 min and 2 h (Section 3.3.1). Two time points were used for settlement, as a preliminary experiment indicated that few spores settled on some of the test surfaces when the standard assay (45 min) was used. As shown in Figure 4-22, after 45 min settlement, the highest density of settled spores was on the Teflon sheets. Compared to Nexterion glass (538±80 spores/mm^2), a significantly lower density of spores was found on the uncoated BE surfaces (148±29 spores/mm^2) (ANOVA, Tukey test, $p < 0.05$). Furthermore, on BE103 and BE100, the settlement density was further reduced to a level comparable to the PEG2000 SAMs. However, the settlement density on SLIPS BE70 was significantly higher (245±17 spores/mm^2) than on BE103 and BE100 surfaces (ANOVA, Tukey test, $p < 0.05$). After 2 h incubation, a slight increase in spore numbers was observed for most of the surfaces, while the trend between

different samples remained the same. It has been reported that hydrophobic surfaces were more favorable for spore attachment [27, 54], which was consistent with the high settlement on Teflon sheets in our study. Saturating the microtexture and covering the surfaces with the lubricating fluorocarbons made BE103 and BE100 water-repellent with low water contact angle hysteresis (<10°), reflecting its slippery property. This predominant feature in effect rendered the SLIPS unfavorable for spore settlement. Settlement of only ca. 12 spores/mm^2 was found after 45 min incubation for both surfaces, and no notable increase of settled spores was observed after 2 h incubation. Statistically higher settlement on BE70 (245±17 spores/mm^2 at 45 min and 471±22 spores/mm^2 at 2 h) compared with BE103 and BE100 (ANOVA, Tukey test, $p < 0.05$) could at least be explained in part by disintegration of the former surface in seawater after 2 days of preincubation, as indicated by the increase of the water contact angle hysteresis from 6^o to 138^o. Similar results were obtained from a repeating experiment with a different batch of spores.

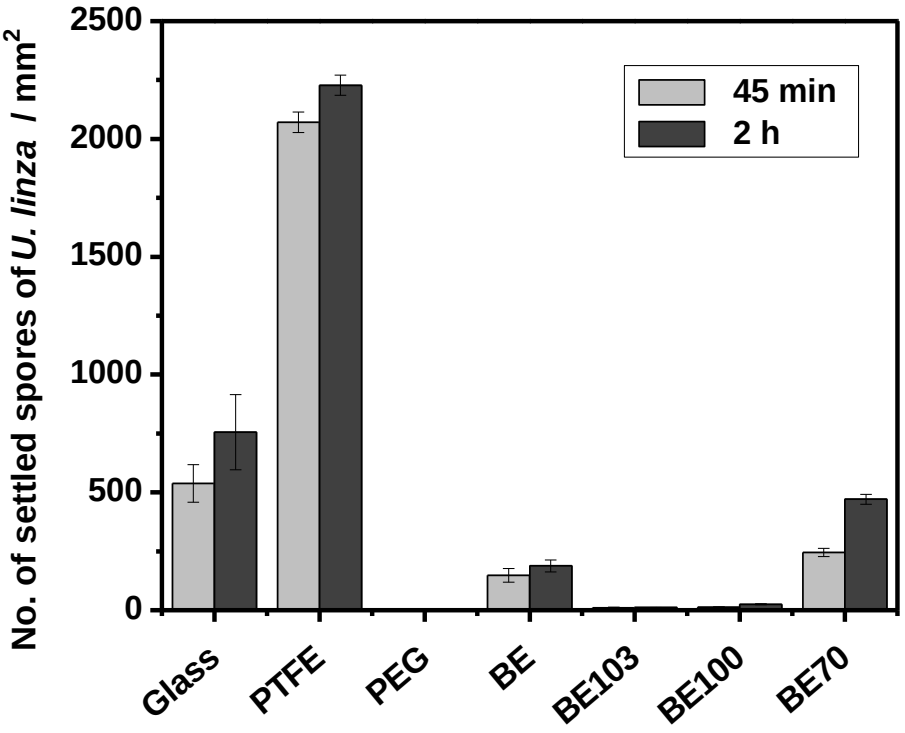

Figure 4-22 The density of spores of *Ulva linza* settled after 45 min and 2 h on different surfaces. Values are the means of 90 counts; 30 counts collected from each of 3 replicates. Error bars represent standard errors.

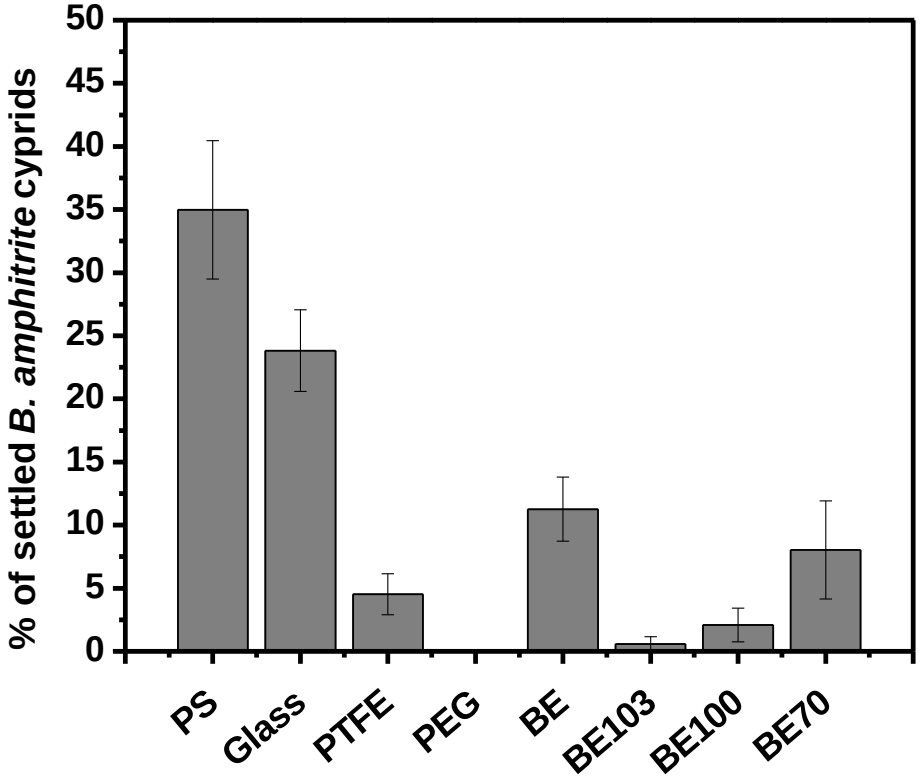

Figure 4-23 Percentage settlement of *Balanus amphitrite* cyprids on different surfaces after 48 h. Reported values are the average of the data collected from 6 replicates with error bars showing the standard errors.

The percentage settlement of cyprids (percentage settlement = settled cyprids / live cyprids × 100%) was calculated after 48 h incubation (Section 3.3.3). A representative set of data of 3 separate settlement assays is shown in Figure 4-23. Cyprid settlement on polystyrene, at 35% (PS in Figure 4-23), was consistent with the expected settlement for this standard surface. Higher settlement was found on Nexterion glass than on PTFE. Compared with Nexterion glass, the settlement was significantly lower on PEG2000 SAMs and BE103 (Kruskal Wallis, Dunn's test, $p < 0.05$). Around 10% cyprids settled on BE and BE70, and the settlement on BE100 was only 2% (±1% SE). Excellent resistance to cyprid settlement on PEG2000 SAMs was consistent with the ability of PEG to inhibit settlement of different marine fouling species [52, 124]. The comparably water-repellent and relatively smooth BE103 and BE100 showed a strong inhibition of settlement of cyprids (compared to glass and PS), which was not significantly different from PEG (Kruskal Wallis, Dunn's test, $p > 0.05$). The reduced settlement on these two surfaces might reflect poor adhesion during presettlement ('searching') behavior (the low settlement prevented measures of adhesion of settled cyprids). Because of the instability

of Fluorinert FC-70 layer after long contact with seawater, the porous substrate could be partially exposed to organisms. This could explain why similar percentages of cyprids settled on BE and BE70.

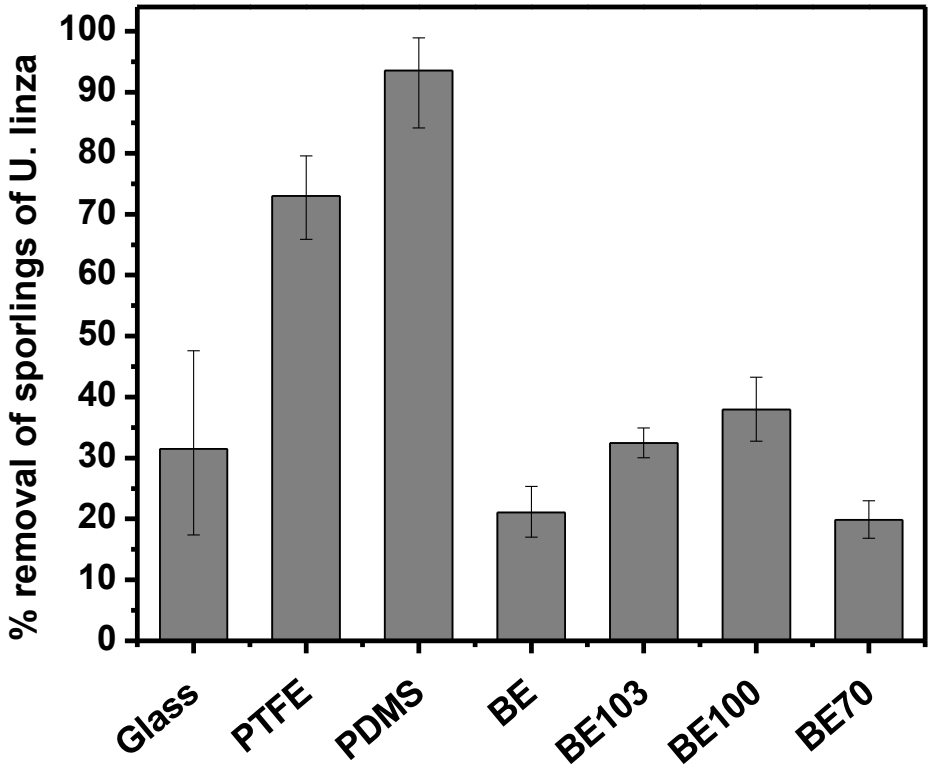

Figure 4-24 Percentage removal of *Ulva* sporelings from different surfaces after exposure to a shear stress of 50 Pa in a water channel for 5 min. Reported values represent the average removal of biomass on 6 replicates. Error bars represent 95% confidence limits of intervals (CI) and are calculated from arcsine-transformed data.

The fouling-release properties of surfaces were assessed by determining the adhesion strength of 7-day old sporelings of *Ulva*, estimated as the proportion removed from surfaces under a defined shear stress in a water channel (Section 3.3.4). The removal of sporelings after culture under static conditions was performed by application of a high shear stress in order to test how easy sporelings could be removed from the surfaces. In Figure 4-24, sporelings growing on PDMS were almost completely removed by 50 Pa wall shear stress and the removal was significantly higher than that from all the other surfaces (ANOVA, Tukey test, $p < 0.05$). This result was consistent with the known fouling-release properties of siloxane-based coatings [98]. The percentage removal from Nexterion glass and PTFE was 31%±15% and 73%±7%, respectively, which was

consistent with previous data showing relatively strong attachment on hydrophilic surfaces such as glass and weak attachment on hydrophobic surfaces such as PTFE [98]. Around 20% of the sporelings that attached on BE and BE70 were removed, while on BE103 and BE100 the removal increased up to ca. 35%. However, we observed some of the rhizoids of sporelings grew into the underlying porous microstructures after 7 days of culture. BE103 and BE100 SLIPS surfaces exhibited excellent performance in resisting settlement (adhesion) of spores. However, once spores developed into sporelings they were able to overcome the oily barrier and attach to the substrate, thus lowering removal efficiency. As shown in the stability test, both the morphology and chemistry of the BE70 surface changed after 7 days incubation in seawater. Therefore, we concluded that the change in both morphology and chemistry of the surfaces was the cause of the poor fouling release performance of the BE70 surfaces.

As shown above, excellent anti-fouling properties of BE103 and BE100 surfaces were found. An important mechanistic question is whether the 'fluid' property alone or its combination with the chemical nature of the material is responsible for its anti-fouling behavior. In the case of the settlement of spores of *Ulva linza* (Figure 4-22), the fluidity of the coating was clearly an important factor required for reducing the number of adhered spores (cf. PTFE *vs*. BE103 in Figure 4-22). A similar trend was observed for the settlement of cyprids on PTFE *vs*. BE103 (Figure 4-23). However, our study also indicated that the chemical nature of the coating influenced the attachment of both spores and cyprids. The stability and anti-fouling properties of BE100 and BE70 differed significantly (see Figure 4-20, Figure 4-22 and Figure 4-23). However, they had similar kinematic viscosity (FC-70: 0.12 cm^2/s at 25 °C; Krytox100: 0.12 cm^2/s at 20 °C) [120] and, hence, similar thickness of the fluid layer on the porous substrate could be expected. Therefore, the different anti-fouling performance observed for BE70 and BE100 could be attributed to their different chemical nature (perfluoroalkylated tertiary amine – FC 70 *vs.* perfluorinated polyether – Krytox100 and Krytox103) as well as the difference in the molecular weight (Table 6-2 in the supporting information in appendix, Section 6.1). Interestingly, the antifouling performance of BE100 was similar to that of BE103, despite the higher viscosity of BE103 (Krytox 103: 0.82 cm^2/s at 20 °C) [120], indicating that the possible reduction of the thickness of the fluid layer in BE100 did not affect the antifouling properties.

4.4.4 Field test

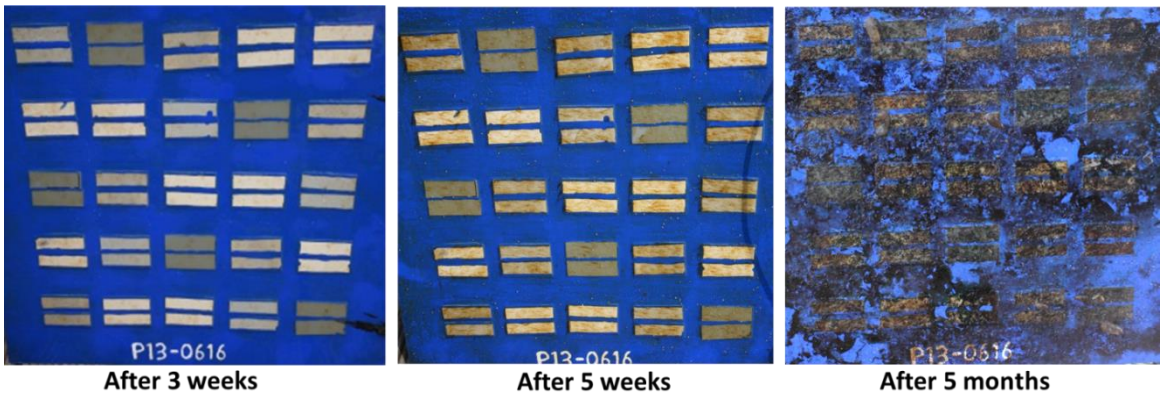

Figure 4-25 Photos of the testing board after immersion for 3 weeks, 5 weeks and 5 months.

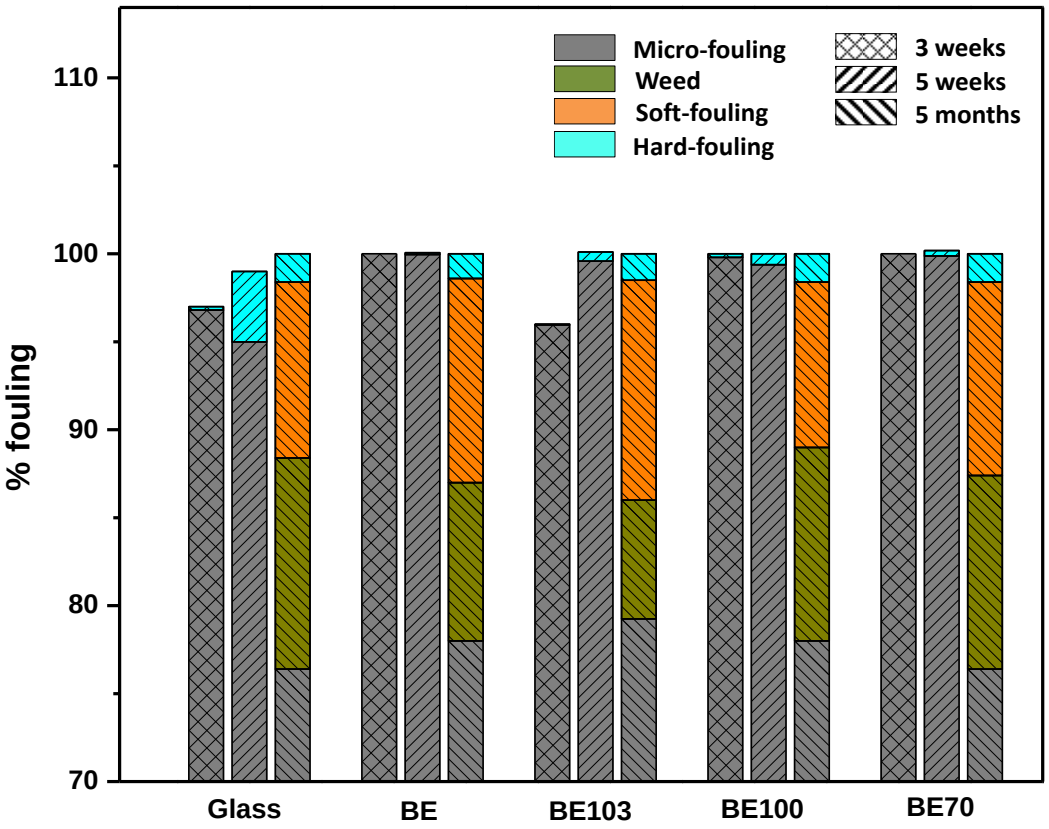

Figure 4-26 Percentages of micro-fouling, Weed, soft-fouling and hard-fouling on different surfaces after immersion for 3 weeks, 5 weeks and 5 months, respectively. Reported values are the means of 5 readings from 10 replicates of each sample type.

As shown in Figure 4-25 and Figure 4-26, after 3 weeks of immersion BE, BE100 and BE70 were covered by mainly microfouling. In comparison, BE103 and Nexterion glasses had slightly lower degree of fouling (ca. 5%). All surfaces were fully occupied by marine colonizers after 5 weeks of immersion with relatively lower amount of hard-

foulers on BE series than Nexterion glasses. When the testing board was immersed for longer time for 5 months, there was no difference between the tested coatings performance in terms of percentage fouling. However, the types of fouling developed with the immersion time. Compared with immersion results after 3 weeks and 5 weeks, weed and soft-fouling composed an important part of the fouling community after immersion for 5 months.

4.4.5 Conclusions

Water-repellent slippery surfaces were prepared by infusing perfluorinated liquids (Krytox103, Krytox100 and Fluorinert FC-70) into the porous hydrophobic poly(butyl methacrylate-*co*-ethylene dimethacrylate) (BMA-EDMA or BE) substrates. Krytox103 and Krytox100 infused BE surfaces maintained the water-repellent slippery property after one month incubation under shaking in artificial seawater and seawater, and revealed a significant inertness in inhibiting attachment of both zoospores and cyprids. The capability of these two surfaces to reduce the adhesion of sporelings of *U. linza* was enhanced compared with pristine porous BE substrates. The marginal performance of Fluorinert FC-70 infused BE could be attributed to the limited stability of the Fluorinert FC-70 layer on the microtexture substrates in seawater. The laboratory study indicated the feasibility of enhancing antifouling performance by the application of the hydrophobic liquid-infused water-repellent concept. However, the poor performance of SLIPS in the field testing suggested that to apply the concept in practice, significant improvements are required to adapt antifouling coatings to the complex ocean environment.

5 Summary and Outlook

Surface microtopographies are of fundamental importance to the settlement of cells and larvae of marine fouling organisms. In this thesis, responses of different fouling organisms, including spores of *Ulva linza*, cells of the diatom *Navicula incerta* and barnacle cyprids of *B. improvisus* and *B. amphitrite*, to various topographic features have been studied.

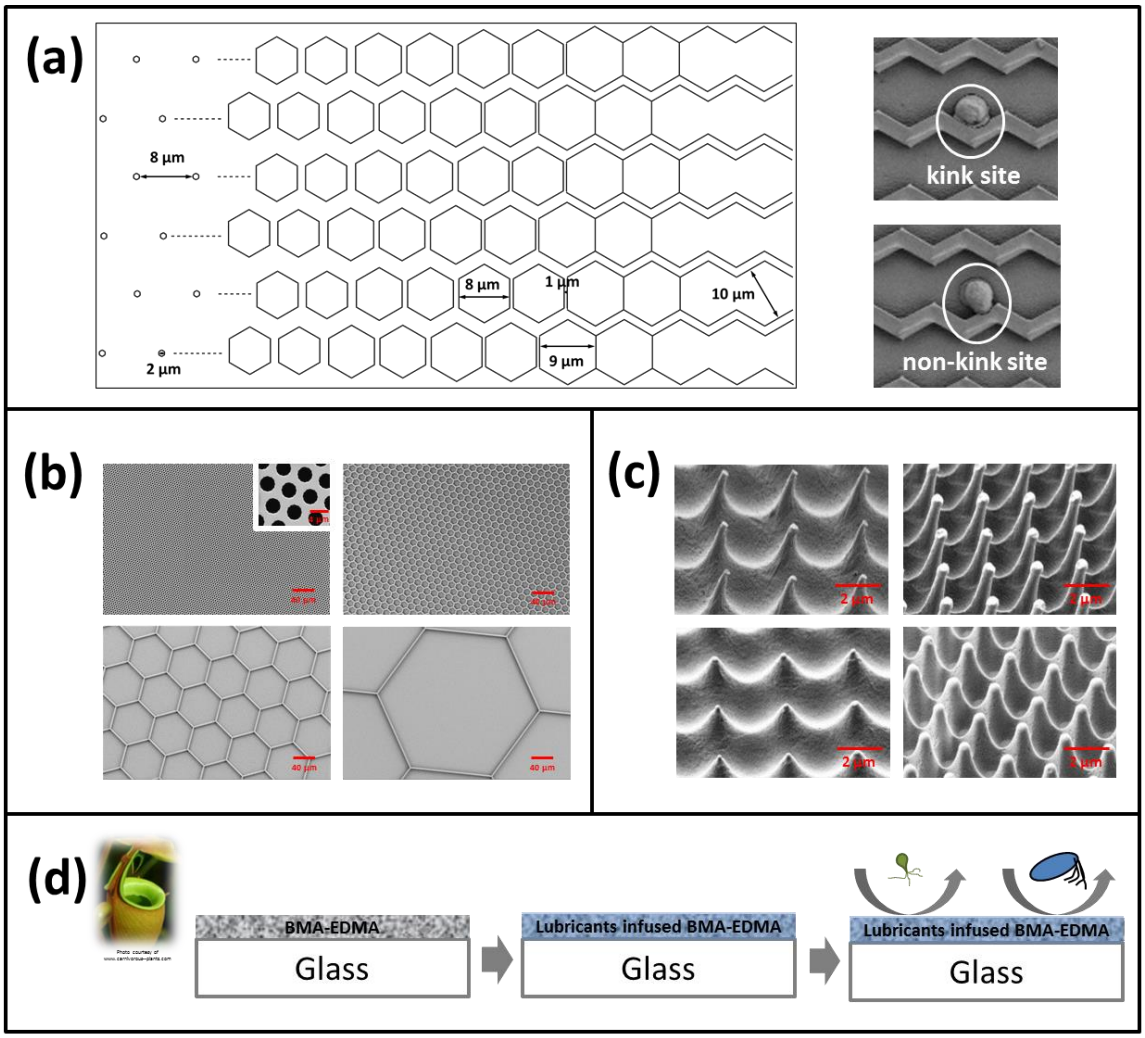

Figure 5-1 Overview of the different patterns and approaches used in this thesis. (a) Honeycomb gradients in Section 4.1; (b) discrete honeycombs in Section 4.2; (c) tapered microstructures in Section 4.3; (d) microtexture-based slippery liquid-infused porous surfaces in Section 4.4.

Gradients of honeycomb pits (Section 4.1, Figure 5-1a) were hot embossed and studied to correlate topographic features with the settlement behavior of spores of *Ulva linza*. Following the gradient study, a series of discrete honeycombs of different sizes (Section 4.2, Figure 5-1b) was soft-casted from the photo-resist mold for the investigation of the size preference of *Ulva* spores, *Navicula* cells and *B. improvisus* cyprids. Moreover, the topographic cues guiding the settlement of spores and diatoms

were further tested on tapered microstructures (Section 4.3, Figure 5-1c) prepared via hot embossing and hot pulling to achieve minimized outmost surface contact area. By combining the surface lubricity on the basis of porous microtopographies, we produced slippery liquid-infused porous surface (SLIPS) (Section 4.4, Figure 5-1d). The SLIPS concept was examined for its antifouling performance in both the lab and the field.

Cells of the microalgae diatom *Navicula incerta* differ from *Ulva* zoospores in both their physical morphology and attachment mechanisms. Unlike spores, diatoms lack flagella. Accordingly they reach the surface by passive sinking through the water column and relocate themselves by 'gliding' on the surfaces [37]. Besides, diatoms are enclosed in a rigid cell wall (frustules), and consequently the cells could straddle the microtopographies when they attach. The initial attachment of diatoms was studied on both discrete honeycombs (Section 4.2, Figure 5-1b) and tapered microstructures (Section 4.3, Figure 5-1c). Generally, the attachment of cells of the diatom *Navicula incerta* was mainly regulated by the 'attachment point theory' [19]. It means the density of attached diatoms increased with available attachment points for each diatom. On topographies with depressed regions smaller than the dimension of diatoms, diatoms tended to hang over the protruding parts of the microstructures. Different numbers of attachment points were available for the attachment of diatoms depending on the microstructure features. With feature spacing remaining constant, the attachment points decreased with the increasing feature size, hence the amount of attached diatoms decreased. On topographies larger than the size of diatoms, e.g., 20 µm discrete honeycombs, the study suggested a possible correlation between the attachment density and the positioning of the attached diatoms (positioned across microstructures vs. positioned inside the depressed region).

Spores of *Ulva linza* are responsible for the colonization of substrates to initiate the life story of this green macroalgae [125]. When surfaces are exposed to the spore solution, Spores commit settlement on selected sites following an active exploration phase [34]. Instead of a cell wall motile spores have a flexible plasma-membrane and therefore can squeeze themselves into narrow space or up against other spores when they settle. The settlement of spores was investigated on topographies of honeycomb gradients (Section 4.1, Figure 5-1a), discrete honeycombs (Section 4.2, Figure 5-1b) and tapered microstructures (Section 4.3, Figure 5-1c) to explore the correlation with topographic cues. In general, the settlement of *Ulva* spores was primarily guided by the Wenzel

roughness factor. As found in the honeycomb gradient study and the tapered microstructure study, the amount of attached spores increased with increasing Wenzel roughness. It is worth mentioning that the local binding geometry, i.e., available contact area, also influenced the settlement, which was more obvious in some special cases, e.g., transition from hexagon to zigzag on honeycomb gradient, 3 µm vs. 230 nm of tapered microstructures. Substantial proof has been gathered to support the fact that spores preferred settlement sites which provided sufficient contact to facilitate the solid adhesion against potential external hydrodynamic forces supposing the choice lay between topographies with similar Wenzel roughness. However, on some of the discrete honeycomb surfaces (Section 4.2, Figure 5-1) the settlement of spores exhibited a deviation from the guideline of Wenzel roughness. This could be attributed to the substrate material used to construct the microstructures in this study, i.e., PDMS, which was highly attractive to spores. As the tendency of spores to settle in groups increased with the settlement density [126], gregarious settlement was observed on all PDMS samples, which impaired the absolute positive correlation between spore settlement and Wenzel roughness.

The sessile life of barnacles starts following the settlement of cyprid larvae [41]. Compared to spores and diatoms, the multicellular cyprid larvae are much more complicated as they possess a large number of sensory and adhesive structures, which are highly diverse in size and function (e.g., adhesive disc, attenular setae) [116]. The settlement of cyprids of *B. improvisus* was examined on discrete honeycombs (Section 4.2, Figure 5-1b) with the feature size between ca. 2.5-250 µm. The percentage of settlement was positively correlated with Wenzel roughness on most of the microstructures. In line with the literature [17], the settlement choice of cyprids could also be explained by the interaction of sensory and adhesive organs with microstructures of comparable sizes.

Going beyond biofouling studies on sole topographies, on the basis of hydrophobic microporous topographies we combined the surface lubricity by introducing a layer of fluorocarbon lubricant liquid, thus producing water-repellent slippery liquid-infused porous surfaces (SLIPS) (Section 4.4, Figure 5-1d). In this case, instead of being exposed directly to fouling organisms, topographies served as the intermediate layer to maintain the lubricity of SLIPS surfaces. Settlement of both *Ulva* spores and *B. amphitrite* cyprids was highly reduced on the SLIPS surfaces, i.e., BE103 and BE100,

which were proven to remain stable over the length of laboratory experiments. This indicated the potential of the SLIPS concept to be applied in fouling-resistant marine coatings. However, the marginal fouling-release and poor field performance suggested that great efforts are still required to improve the resistance to the penetration induced by the growth of fouling organisms and both the antifouling ability and the durability when the coatings are applied in the complicated and harsh real environment.

Hierarchical surface topographies have been mentioned and proposed in the literature [112, 127] as an ideal model to target multiple fouling species. The topographic studies in this thesis showed that the fouling behaviors of different species were actually dominated by different surface topographic cues, e.g., spores — Wenzel roughness vs. diatoms — 'attachment point theory'. This implied that the basis to construct a hierarchical topography for antifouling applications should be set on the combined consideration of different topographic cues instead of the mere mixing of microstructure of different sizes. Furthermore, the combination of other surface properties with topographies or based on topographies could possibly generate more possibilities to realize antifouling and meanwhile reduce the cost.

6 Appendix

6.1 Supplementary materials

Table 6-1 Main chemical components, Young's modulus and water contact angles of polymer materials used in this thesis.

Commercial Name	**Main chemical components**	**Young's modulus (MPa) [128]**	**Water contact angle / ° (mean±SD)**
PLEXIGLAS® Folie Farblos 99530 (Röhm GmbH Chemische Fabrik, Germany)	Polymethylmethacrylate (PMMA)	2430	77.3±1.1
Makrolon® LED2045 (Bayer MaterialScience AG, USA)	Polycarbonate (PC)	2350	97.5±0.3
Sylgard® *184* Silicone Elastomer (Dow Corning Corporation, USA)	Polydimethylsiloxane (PDMS)	1.57	110.2±5.1

Table 6-2 Properties of the lubricant liquids used to construct slippery surfaces (Section 4.4).

Commercial Name	**Chemical Name**	**Kinematic Viscosity (cm^2/s)** [120]
Fluorinert® FC-70	perfluorotri-n-pentylamine	0.12 (at 25°C)
Krytox® GPL 100	perfluoropolyether	0.12 (at 20°C)
Krytox® GPL 103	perfluoropolyether	0.82 (at 20°C)

Table 6-3 Statistical analysis of the diatom *Navicula incerta* on discrete honeycombs (Section 4.2).

smooth	**3 µm**	**5 µm**	**8 µm**	**12 µm**	**20 µm**
a	*ab*	*a*	*b*	*c*	*c*

Values are significantly different to each other on surfaces which don't share the same letter (ANOVA, Tukey test, $p < 0.05$).

Table 6-4 Statistical analysis of *Ulva linza* spores on discrete honeycombs (Section 4.2).

smooth	3 µm	5 µm	8 µm	12 µm	20 µm
a	*bc*	*d*	*b*	*cd*	*e*

Values are significantly different to each other on surfaces which don't share the same letter (ANOVA, Tukey test, $p < 0.05$).

Table 6-5 Statistical analysis of the diatom *Navicula incerta* on tapered microstructures (Section 4.3).

3µm-H	3µm-L	2µm-H	2µm-L	230nm-H	230nm-L	smooth
a	*ab*	*ab*	*b*	*c*	*d*	*e*

Values are significantly different to each other on surfaces which don't share the same letter (ANOVA, Tukey test, $p < 0.05$).

Table 6-6 Statistical analysis of *Ulva linza* spores on tapered microstructures (Section 4.3).

3µm-H	3µm-L	2µm-H	2µm-L	230nm-H	230nm-L	smooth
a	*b*	*c*	*c*	*de*	*d*	*e*

Values are significantly different to each other on surfaces which don't share the same letter (ANOVA, Tukey test, $p < 0.05$).

Table 6-7 Statistical analysis of toxicity data on slippery surfaces (Section 4.4).

ASW	Glass	PTFE	BE	BE103	BE100	BE70
a	*a*	*a*	*a*	*a*	*a*	*a*

Values are significantly different to each other on surfaces which don't share the same letter (ANOVA, Tukey test, $p < 0.05$).

Table 6-8 Statistical analysis of settlement of spores of *Ulva linza* on slippery surfaces (Section 4.4).

	Glass	PTFE	PEG	BE	BE103	BE100	BE70
45min	*a*	*b*	*c*	*cd*	*c*	*c*	*d*
2h	*a*	*b*	*c*	*c*	*c*	*c*	*d*

Values are significantly different to each other on surfaces which do not share the same letter (ANOVA, Tukey test, $p < 0.05$).

Table 6-9 Statistical analysis of settlement of cyprids of *Balanus amphitrite* on slippery surfaces (Section 4.4).

PS	Glass	PTFE	PEG	BE	BE103	BE100	BE70
a	*ab*	*ac*	*c*	*ac*	*c*	*bc*	*ac*

Values are significantly different to each other on surfaces which do not share the same letter (Kruskal Wallis, Dunn's test, $p < 0.05$).

Table 6-10 Statistical analysis of removal of sporelings of *Ulva linza* on slippery surfaces (Section 4.4).

Glass	PTFE	PDMS	BE	BE103	BE100	BE70
ad	*b*	*c*	*d*	*de*	*ae*	*d*

Values are significantly different to each other on surfaces which do not share the same letter (ANOVA, Tukey test, $p < 0.05$).

6.2 Name abbreviations

AC	Adhesive complex
AF	Antifouling
AFM	Atomic force microscopy
AIS	Aquatic invasive species
BE	Poly(butyl methacrylate-co-ethylene dimethacrylate), BMA-EDMA
BE100	Krytox® GPL 100 infused porous poly(butyl methacrylate-co-ethylene dimethacrylate)
BE103	Krytox® GPL 103 infused porous poly(butyl methacrylate-co-ethylene dimethacrylate)
BE70	Fluorinert® FC-70 infused porous poly(butyl methacrylate-co-ethylene dimethacrylate)
CDPs	Controlled depletion systems
CVD	Chemical vapor deposition
DMSO	Dimethyl sulfoxide
EPS	Extracellular polymeric substances
FR	Fouling-release
PC	Polycarbonate
PEG2000 SAMs	PEG2000 self-assembly monolayers
PDMS	Polydimethylsiloxane
PMMA	Polymethylmethacrylate
PS	Polystyrene
PTFE	Polytetrafluoroethene, Teflon
SEM	Scanning electron microscopy
TBT	Tributyltin
TBT-SPCs	Tributyltin self-polishing copolymers
TFS	Tridecafluorooctyltriethoxysilane
Tin-free SPCs	Tin-free self-polishing copolymers
WCA	Water contact angle

6.3 Acknowledgement

First I would like to express my deepest gratitude to both Prof. Michael Grunze and Prof. Axel Rosenhahn, who have provided an excellent platform for my PhD study and offered numerous constructive suggestions and comments on my thesis work. I am grateful for the new knowledge and skills I acquired and all the stimulating discussions I had during my study. Moreover, I highly appreciate the chance to experience the enthusiasm of research and open working atmosphere.

I would like to take the chance to thank all my current and former group members —Stojan Maleschlijski, Stella Bauer, Dr. Isabel Thome, Svenja Vater, Dr. Gonzalo Hernán Sendra, Dr. Maria Pilar Arpa Sancet, Max Hanke, Dr. Thomas Gorniak, Tobias Senkbeil, Andreas Buck, Maria Alles, Dr. Christof Christophis, and Dr. Christina Leinweber for all the help they offered during my study. It is the power that warms you up and keeps you moving on.

I would like to give my sincere thanks to Dr. Maureen E. Callow, Prof. James A. Callow, Dr. John Finlay, Dr. Sophie Mieszkin and Dr. Stephanie E. M. Thompson for their great support for the bioassays with *Ulva* spores and *Navicula* diatoms and all the intensive discussions.

Without the assistance and tutoring of the Hex hot embossing machine, my work could not be completed smoothly. Therefore, I would like to thank Dr. Michael Röhrig, Dr. Marc Schneider. Dr. Matthias Worgull, Dr. Hendrik Hölscher, and Prof. Volker Saile for their great help and discussions.

Heike Fornasier and Dr. Uwe Köhler are greatly thanked for their countless trying to get the suitable photoresist mold for casting. Alessio Di Fino, Dr. Nick Aldred and Prof. Anthony S. Clare are thanked for the support and assistance with the cyprid experiments. Jusheng Li and Dr. Pavel Levkin are thanked for providing the substrates of slippery surfaces.

Besides, I would like to express my sincere thanks to Mr. Benjamin Scherke, Mrs. Swetlana Duchnay and Mrs. Karin Jordan for their great help with the administration work during my PhD work.

The last but not the least, I would like to thank my family and my boyfriend for the great support with my PhD study. I love you all!

6.4 Financial support

The work present in this thesis is supported by:

- European Community's Seventh Framework Programme FP7/2007-2013 under Grant Agreement number 237997 (SEACOAT)

- ONR grants N00014-08-1-1116 and N00014-12-1-0498

- Biointerfaces programme of the Helmholtz Society

6.5 List of publications

Published articles:

- **L. Xiao**, S. E. M. Thompson, M. Röhrig, M. E. Callow, J. A. Callow, M. Grunze and A. Rosenhahn. Hot embossed microtopographic gradients reveal morphological cues that guide the settlement of zoospores. *Langmuir*, **2013**, 29(4): 1093-1099.

- **L. Xiao**, J. Li, S. Mieszkin, A. Di Fino, A. S. Clare, M. E. Callow, J. A. Callow, M. Grunze, A. Rosenhahn and P. A. Levkin. Slippery liquid-infused porous surfaces showing marine antibiofouling properties. *ACS applied materials & interfaces*, **2013**, 5(20): 10074–10080.

Articles in preparation:

- **L. Xiao**, M. Röhrig, J. A. Finlay, S. Mieszkin, M. E. Callow, J. A. Callow, M. Grunze and A. Rosenhahn. Species-specific topographic cues guiding the settlement of *Ulva* spores and diatoms *Navicula*.

- **L. Xiao**, J. A. Finlay, N. Aldred, A. S. Clare, M. E. Callow, J. A. Callow, M. Grunze and A. Rosenhahn. Biofouling studies on honeycomb microstructures: the influence of feature size.

Oral presentations:

- **L. Xiao**, M. Röhrig, S. E. Thompson, M. E. Callow, J. A. Callow, A. Rosenhahn, and M. Grunze. "Surface topographic features to control biofouling". the AVS 58th International Symposium and Exhibition. November 2011

Posters:

- **L. Xiao**, S. E. Thompson, M. Röhrig, M. E. Callow, J. A. Callow, A. Rosenhahn, and M. Grunze. "Settlement on surface topographic gradients". International Workshop of the US Office of Naval Research (ONR) and SEACOAT. December 2011

- **L. Xiao**, S. E. Thompson, M. Röhrig, M. E. Callow, J. A. Callow, M. Grunze, and A. Rosenhahn. "Influence of surface topography on *Ulva* settlement". Bunsentagung 2012. May 2012.

- **L. Xiao**, S. E. Thompson, M. Röhrig, M. E. Callow, J. A. Callow, M. Grunze, and A. Rosenhahn. "Influence of surface topographic gradient on *Ulva* settlement". ICMCF 2012. June 2012.

- **L. Xiao**, S. E. Thompson, M. Röhrig, M. E. Callow, J. A. Callow, M. Grunze, and A. Rosenhahn. "Application of bioinspired topographic gradients in marine antifouling research" International Conference on Bioinspired and Biobased Chemistry & Materials. October 2012.

6.6 References

[1] Wahl, M. (1989) "Marine epibiosis. I. Fouling and antifouling: some basic aspects." *Marine ecology progress series.* **58**(1):175-189.

[2] Callow, M. E. and Callow, J. A. (2002) "Marine biofouling: a sticky problem." *Biologist.* **49**(1):1-5.

[3] Edyvean, R. (2010) "Consequences of fouling on shipping." *Biofouling.* Dürr, S. and Thomason, J. C. (eds). Wiley-Blackwell. Oxford, UK. Vol 10, pp 217-225.

[4] Yvyagintsev, A. and Ivin, V. V. (1995) "Study of biofouling of the submerged structural surfaces of offshore oil and gas production platforms." *Marine Technology Society Journal.* **29**(2):59-62.

[5] Adams, C. M., Shumway, S. E., Whitlatch, R. B., and Getchis, T. (2011) "Biofouling in marine molluscan shellfish aquaculture: a survey assessing the business and economic implications of mitigation." *Journal of the World Aquaculture Society.* **42**(2):242-252.

[6] Schultz, M., Bendick, J., Holm, E., and Hertel, W. (2011) "Economic impact of biofouling on a naval surface ship." *Biofouling.* **27**(1):87-98.

[7] Poloczanska, E. S. and Butler, A. J. (2010) "Biofouling and climate change." *Biofouling.* Dürr, S. and Thomason, J. C. (eds). Wiley-Blackwell. Oxford, UK. pp 333-347.

[8] Ghiya, S. (1987) "Self-polishing antifoulings." *Paintindia.* **37**(10):19-31.

[9] Yebra, D. M., Kiil, S., and Dam-Johansen, K. (2004) "Antifouling technology—past, present and future steps towards efficient and environmentally friendly antifouling coatings." *Progress in Organic Coatings.* **50**(2):75-104.

[10] Milne, A. and Hails, G. (1977) "Marine paint." (The International Paint Company Limited).

[11] Champ, M. A. (2003) "Economic and environmental impacts on ports and harbors from the convention to ban harmful marine anti-fouling systems." *Marine pollution bulletin.* **46**(8):935-940.

[12] Harrison, R. G. (1914) "The reaction of embryonic cells to solid structures." *Journal of Experimental Zoology.* **17**(4):521-544.

[13] Barthlott, W. and Neinhuis, C. (1997) "Purity of the sacred lotus, or escape from contamination in biological surfaces." *Planta.* **202**(1):1-8.

[14] Carman, M. L., Estes, T. G., Feinberg, A. W., Schumacher, J. F., Wilkerson, W., Wilson, L. H., et al. (2006) "Engineered antifouling microtopographies–correlating wettability with cell attachment." *Biofouling.* **22**(1):11-21.

[15] Cao, X., Pettitt, M. E., Wode, F., Arpa Sancet, M. P., Fu, J., Ji, J., et al. (2010) "Interaction of zoospores of the green alga *Ulva* with bioinspired micro- and nanostructured surfaces prepared by polyelectrolyte layer-by-layer self-assembly." *Advanced Functional Materials.* **20**(12):1984-1993.

[16] Schumacher, J. F., Carman, M. L., Estes, T. G., Feinberg, A. W., Wilson, L. H., Callow, M. E., et al. (2007) "Engineered antifouling microtopographies–effect of feature size, geometry, and roughness on settlement of zoospores of the green alga *Ulva*." *Biofouling.* **23**(1):55-62.

[17] Berntsson, K. M., Jonsson, P. R., Lejhall, M., and Gatenholm, P. (2000) "Analysis of behavioural rejection of micro-textured surfaces and implications for recruitment by the barnacle *Balanus improvisus*." *Journal of Experimental Marine Biology and Ecology.* **251**(1):59-83.

[18] Berke, A. P., Turner, L., Berg, H. C., and Lauga, E. (2008) "Hydrodynamic attraction of swimming microorganisms by surfaces." *Physical review letters.* **101**(3):038102.

[19] Scardino, A., Harvey, E., and De Nys, R. (2006) "Testing attachment point theory: diatom attachment on microtextured polyimide biomimics." *Biofouling.* **22**(1):55-60.

[20] FathomShipping (2013) "Hull fouling control: the era of innovation." http://gcaptain.com/hull-fouling-control-innovation/

[21] Gollasch, S. (2002) "The importance of ship hull fouling as a vector of species introductions into the North Sea." *Biofouling.* **18**(2):105-121.

[22] Godwin, L. S. (2003) "Hull fouling of maritime vessels as a pathway for marine species invasions to the Hawaiian Islands." *Biofouling.* **19**(S1):123-131.

[23] Almeida, E., Diamantino, T. C., and de Sousa, O. (2007) "Marine paints: the particular case of antifouling paints." *Progress in Organic Coatings.* **59**(1):2-20.

[24] Callow, J. A. and Callow, M. E. (2011) "Trends in the development of environmentally friendly fouling-resistant marine coatings." *Nature Communications.* **2**:244.

[25] Chambers, L. D., Stokes, K. R., Walsh, F. C., and Wood, R. J. (2006) "Modern approaches to marine antifouling coatings." *Surface and Coatings Technology.* **201**(6):3642-3652.

[26] Jain, A. and Bhosle, N. B. (2009) "Biochemical composition of the marine conditioning film: implications for bacterial adhesion." *Biofouling.* **25**(1):13-19.

[27] Thome, I., Pettitt, M. E., Callow, M. E., Callow, J. A., Grunze, M., and Rosenhahn, A. (2012) "Conditioning of surfaces by macromolecules and its implication for the settlement of zoospores of the green alga *Ulva linza*." *Biofouling.* **28**(5):501-510.

[28] Rittschof, D. (2010) "Research on practical environmentally benign antifouling coatings." *Biofouling.* Dürr, S. and Thomason, J. C. (eds). Wiley-Blackwell. Oxford, UK. pp 396-409.

[29] Maggs, C. A. and Callow, M. E. (2003) "Algal spores." *eLS.*

[30] Callow, M. E., Callow, J. A., Pickett‐Heaps, J. D., and Wetherbee, R. (1997) "Primary adhesion of *Enteromorpha* (*Chlorophyta*, *Ulvales*) propagules: quantitative settlement studies and video microscopy." *Journal of Phycology.* **33**(6):938-947.

[31] Callow, J. A. and Callow, M. E. (2006) "The *Ulva* spore adhesive system." *Biological adhesives.* Smith, A. M. and Callow, J. A. (eds). Springer Berlin Heidelberg. pp 63-78.

[32] Callow, M. E., Jennings, A. R., Brennan, A., Seegert, C., Gibson, A., Wilson, L., et al. (2002) "Microtopographic cues for settlement of zoospores of the green fouling alga *Enteromorpha*." *Biofouling.* **18**(3):229-236.

[33] Heydt, M., Rosenhahn, A., Grunze, M., Pettitt, M., Callow, M., and Callow, J. (2007) "Digital in-line holography as a three-dimensional tool to study motile marine organisms during their exploration of surfaces." *The Journal of Adhesion.* **83**(5):417-430.

[34] Heydt, M., Pettitt, M., Cao, X., Callow, M., Callow, J., Grunze, M., et al. (2012) "Settlement behavior of zoospores of *Ulva linza* during surface selection studied by digital holographic microscopy." *Biointerphases.* **7**(33):1-7.

[35] Umemura, K., Noguchi, Y., Ichinose, T., Hirose, Y., Kuroda, R., and Mayama, S. (2008) "Diatom cells grown and baked on a functionalized mica surface." *Journal of biological physics.* **34**(1-2):189-196.

[36] Wetherbee, R., Lind, J. L., Burke, J., and Quatrano, R. S. (1998) "Minireview—the first kiss: establishment and control of initial adhesion by raphid diatoms." *Journal of Phycology.* **34**(1):9-15.

[37] Lebret, K., Thabard, M., and Hellio, C. (2009) "Algae as marine fouling organisms: adhesion damage and prevention." *Advances in marine antifouling coatings and technologies.* Hellio, C. and Diego, Y. (eds). Woodhead Publishing. Cambridge, UK. pp 80-112.

[38] Gordon, R. (1987) "A retaliatory role for algal projectiles, with implications for the mechanochemistry of diatom gliding motility." *Journal of theoretical biology.* **126**(4):419-436.

[39] Chiovitti, A., Dugdale, T. M., and Wetherbee, R. (2006) "Diatom adhesives: molecular and mechanical properties." *Biological adhesives.* Smith, A. M. and Callow, J. A. (eds). Springer Berlin Heidelberg. pp 79-103.

[40] Roughgarden, J., Gaines, S., and Possingham, H. (1988) "Recruitment dynamics in complex life cycles." *Science.* **241**(4872):1460-1466.

[41] Aldred, N. and Clare, A. S. (2008) "The adhesive strategies of cyprids and development of barnacle-resistant marine coatings." *Biofouling.* **24**(5):351-363.

[42] Doochin, H. D. (1951) "The morphology of *Balanus improvisus* Darwin and *Balanus amphitrite niveus* Darwin during initial attachment and metamorphosis." *Bulletin of Marine Science.* **1**(1):15-39.

[43] Kamino, K. (2006) "Barnacle underwater attachment." *Biological adhesives.* Smith, A. M. and Callow, J. A. (eds). Springer Berlin Heidelberg. pp 145-166.

[44] Walker, G. (1981) "The adhesion of barnacles." *The Journal of Adhesion.* **12**(1):51-58.

[45] Walker, G. (1973) "The early development of the cement apparatus in the barnacle, *Balanus balanoides* (L.) (Crustacea: Cirripedia)." *Journal of Experimental Marine Biology and Ecology*. **12**(3):305-314.

[46] Yule, A. and Walker, G. (1984) "The adhesion of the barnacle, *Balanus balanoides*, to slate surfaces." *Journal of the Marine Biological Association of the UK* **64**:147-156.

[47] Walker, G. (1971) "A study of the cement apparatus of the cypris larva of the barnacle *Balanus balanoides*." *Marine Biology*. **9**(3):205-212.

[48] Okano, K., Shimizu, K., Satuito, C., and Fusetani, N. (1996) "Visualization of cement exocytosis in the cypris cement gland of the barnacle *Megabalanus rosa*." *The Journal of Experimental Biology*. **199**(10):2131-2137.

[49] Kiil, S., Weinell, C. E., Pedersen, M. S., and Dam-Johansen, K. (2001) "Analysis of self-polishing antifouling paints using rotary experiments and mathematical modeling." *Industrial & engineering chemistry research*. **40**(18):3906-3920.

[50] Schilp, S., Rosenhahn, A., Pettitt, M. E., Bowen, J., Callow, M. E., Callow, J. A., et al. (2009) "Physicochemical properties of (ethylene glycol)-containing self-assembled monolayers relevant for protein and algal cell resistance." *Langmuir*. **25**(17):10077-10082.

[51] Christophis, C., Grunze, M., and Rosenhahn, A. (2010) "Quantification of the adhesion strength of fibroblast cells on ethylene glycol terminated self-assembled monolayers by a microfluidic shear force assay." *Physical Chemistry Chemical Physics*. **12**(17):4498-4504.

[52] Ekblad, T., Bergström, G., Ederth, T., Conlan, S. L., Mutton, R., Clare, A. S., et al. (2008) "Poly (ethylene glycol)-containing hydrogel surfaces for antifouling applications in marine and freshwater environments." *Biomacromolecules*. **9**(10):2775-2783.

[53] Ista, L. K. and López, G. P. (2012) "Interfacial tension analysis of oligo (ethylene glycol)-terminated self-assembled monolayers and their resistance to bacterial attachment." *Langmuir*. **28**(35):12844-12850.

[54] Schilp, S., Kueller, A., Rosenhahn, A., Grunze, M., Pettitt, M. E., Callow, M. E., et al. (2007) "Settlement and adhesion of algal cells to hexa (ethylene glycol)-containing self-assembled monolayers with systematically changed wetting properties." *Biointerphases*. **2**(4):143-150.

[55] Chaudhury, M. K., Finlay, J. A., Chung, J. Y., Callow, M. E., and Callow, J. A. (2005) "The influence of elastic modulus and thickness on the release of the soft-fouling green alga *Ulva linza* (syn. *Enteromorpha linza*) from poly (dimethylsiloxane)(PDMS) model networks." *Biofouling.* **21**(1):41-48.

[56] Zhang, J. W., Lin, C. G., Wang, L., Zheng, J. Y., Peng, Y. L., and Duan, D. X. (2011) "The influence of elastic modulus on the adhesion of fouling organism to poly (dimethylsiloxane)(PDMS)." *Advanced Materials Research.* **152**:1466-1470.

[57] Gray, N. L., Banta, W. C., and Loeb, G. I. (2002) "Aquatic biofouling larvae respond to differences in the mechanical properties of the surface on which they settle." *Biofouling.* **18**(4):268-273.

[58] Ahmed, N., Murosaki, T., Kakugo, A., Kurokawa, T., Gong, J. P., and Nogata, Y. (2011) "Long-term in situ observation of barnacle growth on soft substrates with different elasticity and wettability." *Soft Matter.* **7**(16):7281-7290.

[59] Brady Jr, R. F. (1999) "Properties which influence marine fouling resistance in polymers containing silicon and fluorine." *Progress in Organic Coatings.* **35**(1):31-35.

[60] Brady Jr, R. F. and Singer, I. L. (2000) "Mechanical factors favoring release from fouling release coatings." *Biofouling.* **15**(1-3):73-81.

[61] Chen, H., Song, W., Zhou, F., Wu, Z., Huang, H., Zhang, J., et al. (2009) "The effect of surface microtopography of poly (dimethylsiloxane) on protein adsorption, platelet and cell adhesion." *Colloids and Surfaces B: Biointerfaces.* **71**(2):275-281.

[62] Hayes, J., Khan, I., Archer, C., and Richards, R. (2010) "The role of surface microtopography in the modulation of osteoblast differentiation." *European Cells and Materials.* **20**:98-108.

[63] Edwards, K. J. and Rutenberg, A. D. (2001) "Microbial response to surface microtopography: the role of metabolism in localized mineral dissolution." *Chemical Geology.* **180**(1):19-32.

[64] Tanaka, M., Takayama, A., Ito, E., Sunami, H., Yamamoto, S., and Shimomura, M. (2007) "Effect of pore size of self-organized honeycomb-patterned polymer films on spreading, focal adhesion, proliferation, and function of endothelial cells." *Journal of nanoscience and nanotechnology.* **7**(3):763-772.

[65] Maréchal, J.-P. and Hellio, C. (2009) "Challenges for the development of new non-toxic antifouling solutions." *International journal of molecular sciences.* **10**(11):4623-4637.

[66] Aldred, N., Scardino, A., Cavaco, A., de Nys, R., and Clare, A. S. (2010) "Attachment strength is a key factor in the selection of surfaces by barnacle cyprids (*Balanus amphitrite*) during settlement." *Biofouling.* **26**(3):287-299.

[67] Scardino, A. J. and de Nys, R. (2011) "Mini review: Biomimetic models and bioinspired surfaces for fouling control." *Biofouling.* **27**(1):73-86.

[68] Verran, J. and Boyd, R. D. (2001) "The relationship between substratum surface roughness and microbiological and organic soiling: a review." *Biofouling.* **17**(1):59-71.

[69] Korber, D., Choi, A., Wolfaardt, G., Ingham, S., and Caldwell, D. (1997) "Substratum topography influences susceptibility of *Salmonella enteritidis* biofilms to trisodium phosphate." *Applied and environmental microbiology.* **63**(9):3352-3358.

[70] Schumacher, J. F., Aldred, N., Callow, M. E., Finlay, J. A., Callow, J. A., Clare, A. S., et al. (2007) "Species-specific engineered antifouling topographies: correlations between the settlement of algal zoospores and barnacle cyprids." *Biofouling.* **23**(5):307-317.

[71] Decker, J., Kirschner, C., Long, C., Finlay, J. A., Callow, M. E., Callow, J. A., et al. (2013) "Engineered antifouling microtopographies: an energetic model that predicts cell attachment." *Langmuir.* **29**(42):13023-13030.

[72] Schumacher, J. F., Long, C. J., Callow, M. E., Finlay, J. A., Callow, J. A., and Brennan, A. B. (2008) "Engineered nanoforce gradients for inhibition of settlement (attachment) of swimming algal spores." *Langmuir.* **24**(9):4931-4937.

[73] Scardino, A., Guenther, J., and De Nys, R. (2008) "Attachment point theory revisited: the fouling response to a microtextured matrix." *Biofouling.* **24**(1):45-53.

[74] Long, C. J., Schumacher, J. F., Robinson, P. A., Finlay, J. A., Callow, M. E., Callow, J. A., et al. (2010) "A model that predicts the attachment behavior of *Ulva linza* zoospores on surface topography." *Biofouling.* **26**(4):411-419.

[75] Magin, C. M., Long, C. J., Cooper, S. P., Ista, L. K., López, G. P., and Brennan, A. B. (2010) "Engineered antifouling microtopographies: the role of Reynolds number in a model that predicts attachment of zoospores of *Ulva* and cells of *Cobetia marina*." *Biofouling.* **26**(6):719-727.

[76] Worgull, M., Heckele, M., Mappes, T., Matthis, B., Tosello, G., Metz, T., et al. (2008) "Sub-µ structured lotus surfaces manufacturing." *Microsystem Technologies.* **15**(8):1327-1333.

[77] Worgull, M. (eds) (2009) *Hot embossing: theory and technology of microreplication.* Elsevier Inc. Oxford, UK.

[78] Kumar, G., Tang, H. X., and Schroers, J. (2009) "Nanomoulding with amorphous metals." *Nature.* **457**(7231):868-872.

[79] Kolew, A., Münch, D., Sikora, K., and Worgull, M. (2011) "Hot embossing of micro and sub-micro structured inserts for polymer replication." *Microsystem technologies.* **17**(4):609-618.

[80] Heckele, M. and Schomburg, W. (2004) "Review on micro molding of thermoplastic polymers." *Journal of Micromechanics and Microengineering.* **14**(3):R1.

[81] Chou, S. Y., Keimel, C., and Gu, J. (2002) "Ultrafast and direct imprint of nanostructures in silicon." *Nature.* **417**(6891):835-837.

[82] Worgull, M., Kolew, A., Heilig, M., Schneider, M., Dinglreiter, H., and Rapp, B. (2011) "Hot embossing of high performance polymers." *Microsystem technologies.* **17**(4):585-592.

[83] Pan, C., Wu, T., Chen, M., Chang, Y., Lee, C., and Huang, J. (2008) "Hot embossing of micro-lens array on bulk metallic glass." *Sensors and Actuators A: Physical.* **141**(2):422-431.

[84] Röhrig, M., Schneider, M., Etienne, G., Oulhadj, F., Pfannes, F., Kolew, A., et al. (2013) "Hot pulling and embossing of hierarchical nano-and micro-structures." *Journal of Micromechanics and Microengineering.* **23**(10):105014.

[85] Goodhew, P. J., Humphreys, F. J., and Beanland, R. (eds) (2001) *Electron microscopy and analysis.* Taylor & Francis Inc. London, UK.

[86] Egerton, R. F. (eds) (2005) *Physical principles of electron microscopy: an introduction to TEM, SEM, and AEM.* Springer Science+Business Media, Inc. New York, USA.

[87] Binnig, G., Quate, C. F., and Gerber, C. (1986) "Atomic force microscope." *Physical review letters.* **56**(9):930.

[88] Vickerman, J. C. and Gilmore, I. S. (eds) (2009) *Surface analysis: the principal techniques.* John Wiley & Sons, Ltd. Chichester, UK.

[89] Braet, F., De Zanger, R., Kämmer, S., and Wisse, E. (1997) "Noncontact versus contact imaging: An atomic force microscopic study on hepatic endothelial cells in vitro." *International journal of imaging systems and technology.* **8**(2):162-167.

[90] Zhong, Q., Inniss, D., Kjoller, K., and Elings, V. (1993) "Fractured polymer/silica fiber surface studied by tapping mode atomic force microscopy." *Surface Science Letters.* **290**(1):L688-L692.

[91] Young, T. (1805) "An essay on the cohesion of fluids." *Philosophical Transactions of the Royal Society of London.* **95**:65-87.

[92] Wenzel, R. N. (1936) "Resistance of solid surfaces to wetting by water." *Industrial & Engineering Chemistry.* **28**(8):988-994.

[93] Cassie, A. and Baxter, S. (1944) "Wettability of porous surfaces." *Transactions of the Faraday Society.* **40**:546-551.

[94] Levkin, P. A., Svec, F., and Fréchet, J. M. (2009) "Porous polymer coatings: a versatile approach to superhydrophobic surfaces." *Advanced Functional Materials.* **19**(12):1993-1998.

[95] Callow, M. E., Callow, J., Ista, L. K., Coleman, S. E., Nolasco, A. C., and López, G. P. (2000) "Use of self-assembled monolayers of different wettabilities to study surface selection and primary adhesion processes of green algal (*Enteromorpha*) zoospores." *Applied and environmental microbiology.* **66**(8):3249-3254.

[96] Petrone, L., Di Fino, A., Aldred, N., Sukkaew, P., Ederth, T., Clare, A. S., et al. (2011) "Effects of surface charge and Gibbs surface energy on the settlement behaviour of barnacle cyprids (*Balanus amphitrite*)." *Biofouling.* **27**(9):1043-1055.

[97] Starr, R. C. and Zeikus, J. A. (1993) "UTEX: The culture collection of algae at the University of Texas at Austin 1993 list of cultures." *Journal of Phycology.* **29**(s2):1-106.

[98] Mieszkin, S., Martin-Tanchereau, P., Callow, M. E., and Callow, J. A. (2012) "Effect of bacterial biofilms formed on fouling-release coatings from natural seawater and *Cobetia marina*, on the adhesion of two marine algae." *Biofouling.* **28**(9):953-968.

[99] Schultz, M. P., Finlay, J. A., Callow, M. E., and Callow, J. A. (2000) "A turbulent channel flow apparatus for the determination of the adhesion strength of microfouling organisms." *Biofouling.* **15**(4):243-251.

[100] Tokumitsu, S., Liebich, A., Herrwerth, S., Eck, W., Himmelhaus, M., and Grunze, M. (2002) "Grafting of alkanethiol-terminated poly (ethylene glycol) on gold." *Langmuir.* **18**(23):8862-8870.

[101] Fick, J., Steitz, R., Leiner, V., Tokumitsu, S., Himmelhaus, M., and Grunze, M. (2004) "Swelling behavior of self-assembled monolayers of alkanethiol-terminated poly (ethylene glycol): a neutron reflectometry study." *Langmuir.* **20**(10):3848-3853.

[102] Elliott, A. C. and Hynan, L. S. (2011) "A SAS macro implementation of a multiple comparison post hoc test for a Kruskal–Wallis analysis." *Computer methods and programs in biomedicine.* **102**(1):75-80.

[103] Wright, S., Caldwell, G. S., and Clare, A. S. (2012) "Sperm activation in acorn barnacles by elevation of seawater pH." *Invertebrate Reproduction & Development.* **56**(1):79-85.

[104] Wong, J. Y., Leach, J. B., and Brown, X. Q. (2004) "Balance of chemistry, topography, and mechanics at the cell–biomaterial interface: issues and challenges for assessing the role of substrate mechanics on cell response." *Surface Science.* **570**(1):119-133.

[105] Ekblad, T., Andersson, O., Tai, F.-i., Ederth, T., and Liedberg, B. (2009) "Lateral control of protein adsorption on charged polymer gradients." *Langmuir.* **25**(6):3755-3762.

[106] Genzer, J. and Bhat, R. R. (2008) "Surface-bound soft matter gradients." *Langmuir.* **24**(6):2294-2317.

[107] Carter, S. B. (1965) "Principles of cell motility: the direction of cell movement and cancer invasion." *Nature.* **208**(5016):1183.

[108] Genzer, J. (2005) "Templating surfaces with gradient assemblies." *The Journal of Adhesion.* **81**(3-4):417-435.

[109] Morgenthaler, S., Zink, C., and Spencer, N. D. (2008) "Surface-chemical and-morphological gradients." *Soft Matter.* **4**(3):419-434.

[110] Blondiaux, N., Morgenthaler, S., Pugin, R., Spencer, N. D., and Liley, M. (2008) "Gradients of topographical structure in thin polymer films." *Applied Surface Science.* **254**(21):6820-6825.

[111] Chaudhury, M., Daniel, S., Callow, M., Callow, J., and Finlay, J. (2006) "Settlement behavior of swimming algal spores on gradient surfaces." *Biointerphases.* **1**(1):18-21.

[112] Efimenko, K., Finlay, J., Callow, M. E., Callow, J. A., and Genzer, J. (2009) "Development and testing of hierarchically wrinkled coatings for marine antifouling." *ACS applied materials & interfaces.* **1**(5):1031-1040.

[113] Thompson, S., Callow, J., Callow, M., Wheeler, G., Taylor, A., and Brownlee, C. (2007) "Membrane recycling and calcium dynamics during settlement and adhesion of zoospores of the green alga *Ulva linza*." *Plant, cell & environment.* **30**(6):733-744.

[114] Stranski, I. (1928) "Zur theorie des kristallwachstums." *Z. phys. Chem.* **136**(259):259-278.

[115] Phang, I. Y., Aldred, N., Clare, A. S., and Vancso, G. J. (2008) "Towards a nanomechanical basis for temporary adhesion in barnacle cyprids (*Semibalanus balanoides*)." *Journal of The Royal Society Interface.* **5**(21):397-402.

[116] Bielecki, J., Chan, B. K., Hoeg, J. T., and Sari, A. (2009) "Antennular sensory organs in cyprids of balanomorphan cirripedes: standardizing terminology using *Megabalanus rosa*." *Biofouling.* **25**(3):203-214.

[117] Rosenhahn, A., Ederth, T., and Pettitt, M. E. (2008) "Advanced nanostructures for the control of biofouling: The FP6 EU Integrated Project AMBIO." *Biointerphases.* **3**(1):IR1-IR5.

[118] Gaume, L., Gorb, S., and Rowe, N. (2002) "Function of epidermal surfaces in the trapping efficiency of *Nepenthes alata* pitchers." *New Phytologist.* **156**(3):479-489.

[119] Bohn, H. F. and Federle, W. (2004) "Insect aquaplaning: *Nepenthes* pitcher plants capture prey with the peristome, a fully wettable water-lubricated anisotropic surface." *Proceedings of the National Academy of Sciences.* **101**(39):14138-14143.

[120] Wong, T.-S., Kang, S. H., Tang, S. K., Smythe, E. J., Hatton, B. D., Grinthal, A., et al. (2011) "Bioinspired self-repairing slippery surfaces with pressure-stable omniphobicity." *Nature.* **477**(7365):443-447.

[121] Epstein, A. K., Wong, T.-S., Belisle, R. A., Boggs, E. M., and Aizenberg, J. (2012) "Liquid-infused structured surfaces with exceptional anti-biofouling performance." *Proceedings of the National Academy of Sciences.* **109**(33):13182-13187.

[122] Li, J. S., Ueda, E., Nallapaneni, A., Li, L. X., and Levkin, P. A. (2012) "Printable superhydrophilic–superhydrophobic micropatterns based on supported lipid layers." *Langmuir.* **28**(22):8286-8291.

[123] Li, J., Kleintschek, T., Rieder, A., Cheng, Y., Baumbach, T., Obst, U., et al. (2013) "Hydrophobic liquid-infused porous polymer surfaces for antibacterial applications." *ACS applied materials & interfaces.* **5**(14):6704–6711.

[124] Andersson, O., Ekblad, T., Aldred, N., Clare, A. S., and Liedberg, B. (2009) "Novel application of imaging surface plasmon resonance for in situ studies of the surface exploration of marine organisms." *Biointerphases.* **4**(4):65-68.

[125] Fletcher, R. L. and Callow, M. E. (1992) "The settlement, attachment and establishment of marine algal spores." *British Phycological Journal.* **27**(3):303-329.

[126] Callow, M. E. and Callow, J. (2000) "Substratum location and zoospore behaviour in the fouling alga *Enteromorpha*." *Biofouling.* **15**(1-3):49-56.

[127] Genzer, J. and Efimenko, K. (2006) "Recent developments in superhydrophobic surfaces and their relevance to marine fouling: a review." *Biofouling.* **22**(5):339-360.

[128] Bayer MaterialScience. "Datasheet of Makrolon LED2045." http://www.plastics.bayer.com/en/Products/Makrolon/ProductList/201305212210/Makrolon-LED2045.aspx